AD-A218 680

DTIC FILE COPY

WRDC-TR-89-3099

NONDESTRUCTIVE MEASUREMENT OF RESIDUAL STRESSES IN AIRCRAFT TRANSPARENCIES

B. Basava Raju
Blaine S. West

University of Dayton Research Institute
300 College Park Avenue
Dayton, Ohio 45469-0001

November 1989

DTIC
ELECTE
MAR 0 1 1990
S B D

FINAL REPORT FOR PERIOD DECEMBER 1984-JUNE 1988

Approved for public release, distribution is unlimited

FLIGHT DYNAMICS LABORATORY
WRIGHT RESEARCH AND DEVELOPMENT CENTER
AIR FORCE SYSTEMS COMMAND
WRIGHT-PATTERSON AIR FORCE BASE, OHIO 45433-6553

90 02 28 016

NOTICE

When government drawings, specifications, or other data are used for any purpose other than in connection with a definitely government-related procurement, the United States Government incurs no responsibility or any obligation whatsoever. The fact that the government may have formulated or in any way supplied the said drawings, specifications, or other data, is not to be regarded by implication, or otherwise in any manner construed, as licensing the holder, or any other person or corporation; or as conveying any rights or permission to manufacture, use, or sell any patented invention that may in any way be related thereto.

This technical report has been reviewed and is approved for publication.

Russell E. Urzi

RUSSELL E. URZI
Project Engineer
Windshield Program Office

Ralph J. Speelman

RALPH J. SPEELMAN
Chief, Aircraft Windshield Program Office

FOR THE COMMANDER

Richard E. Colclough, Jr.

RICHARD E. COLCLOUGH, Jr.
Chief, Vehicle Subsystems Div.

If your address has changed, if you wish to be removed from our mailing list, or if the addressee is no longer employed by your organization please notify WRDC/FIVR, Wright-Patterson AFB, OH 45433-6553 to help maintain a current mailing list.

Copies of this report should not be returned unless return is required by security considerations, contractual obligations, or notice on a specific document.

REPORT DOCUMENTATION PAGE

Form Approved OMB No. 0704-0188

1a REPORT SECURITY CLASSIFICATION: UNCLASSIFIED	1b RESTRICTIVE MARKINGS:
2a SECURITY CLASSIFICATION AUTHORITY:	3 DISTRIBUTION/AVAILABILITY OF REPORT: Approved for public release, distribution is unlimited
2b DECLASSIFICATION/DOWNGRADING SCHEDULE:	
4 PERFORMING ORGANIZATION REPORT NUMBER(S): UDR-TR-88-65	5 MONITORING ORGANIZATION REPORT NUMBER(S): WRDC-TR-89-3099
6a NAME OF PERFORMING ORGANIZATION: University of Dayton Research Institute; 6b OFFICE SYMBOL (If applicable):	7a NAME OF MONITORING ORGANIZATION: Flight Dynamics Laboratory (WRDC/FIVR) Wright Research and Development Center
6c ADDRESS (City, State, and ZIP Code): 300 College Park Avenue Dayton, Ohio 45469-0001	7b ADDRESS (City, State, and ZIP Code): Wright-Patterson AFB, OH 45433-6553
8a NAME OF FUNDING/SPONSORING ORGANIZATION; 8b OFFICE SYMBOL (If applicable):	9 PROCUREMENT INSTRUMENT IDENTIFICATION NUMBER: F33615-84-C-3404
8c ADDRESS (City, State, and ZIP Code):	10 SOURCE OF FUNDING NUMBERS: PROGRAM ELEMENT NO. 64212F; PROJECT NO. 1926; TASK NO 01; WORK UNIT ACCESSION NO. 10

11 TITLE (Include Security Classification)
NONDESTRUCTIVE MEASUREMENT OF RESIDUAL STRESSES IN AIRCRAFT TRANSPARENCIES

12 PERSONAL AUTHOR(S)
B. Basava Raju and Blaine S. West

13a TYPE OF REPORT	13b TIME COVERED	14 DATE OF REPORT (Year, Month, Day)	15 PAGE COUNT
Interim	FROM DEC 84 TO FEB 87	1989 November	108

16 SUPPLEMENTARY NOTATION

17 COSATI CODES			18 SUBJECT TERMS (Continue on reverse if necessary and identify by block number)
FIELD	GROUP	SUB-GROUP	Residual Stress, Scattered-Light Photoelasticity, Aircraft Transparency, Surface Wave, Ultrasonic

19 ABSTRACT (Continue on reverse if necessary and identify by block number)

This report documents a program which was conducted to:

- o Design, fabricate, and set up a photoelastic test apparatus capable of measuring residual stresses in aircraft transparencies.
- o Evaluate the accuracy of the scattered-light photoelastic technique by conducting scattered-light photoelastic experiments on four-point bending polycarbonate specimens having known analytical solutions and other experimental solutions.
- o Establish a scattered-light photoelastic experimental procedure for monolithic polycarbonate F-16 transparencies by measuring residual stresses at a typical station on the transparency.
- o Evaluate the scattered-light photoelastic properties of acrylic plastic material.
- o Determine the feasibility of using acoustic wave ultrasonic techniques to determine residual stresses in transparencies.

20 DISTRIBUTION/AVAILABILITY OF ABSTRACT	21 ABSTRACT SECURITY CLASSIFICATION
☒ UNCLASSIFIED/UNLIMITED ☐ SAME AS RPT ☒ DTIC USERS	UNCLASSIFIED

22a NAME OF RESPONSIBLE INDIVIDUAL	22b TELEPHONE (Include Area Code)	22c OFFICE SYMBOL
Lt. Paul Kolodziejski	(513) 255-6524	WRDC/FIVR

DD Form 1473, JUN 86 *Previous editions are obsolete.*

FOREWORD

The effort reported herein was conducted by the University of Dayton Research Institute (UDRI) for the Air Force Wright Aeronautical Laboratories, Flight Dynamics Laboratory, Wright-Patterson Air Force Base, Ohio, under contract F33615-84-C-3404, Project 1926. Air Force administrative direction and technical support was provided by Lts. D J. Altobelli and P. J. Kolodziejski, AFWAL/FIER. The work described herein was conducted during the period December 1984 to February 1987. Project supervision was provided by Mr. Dale H. Whitford, Supervisor, Aerospace Mechanics Division, and technical direction was provided by Mr. Blaine S. West, Head, Structures Group. Major technical effort was accomplished by Dr. B. Basava Raju, Principal Investigator. Mr. Phil A. Graf of the Vibrations Analysis and Control Group was very helpful in resolving many instrumentation problems. Mr. Robert J. Andrews of the Structural Integrity Division and Mr. James M. Aulds of the Electrical and Computer Engineering Division were very helpful in evaluating the performance of the surface wave transducer. The assembly of the photoelastic test set-up was completed by Mr. Phil A. Graf and Mr. John Blust. Experimental support was provided by Mr. John Blust, Ms. Terri Dietz and Mr. Kurt Ostdiek.

Accession For
NTIS GRA&I ☑
DTIC TAB ☐
Unannounced ☐
Justification
By
Distribution/
Availability Codes
Dist | Avail and/or Special
A-1

TABLE OF CONTENTS

TABLE OF CONTENTS (continued)

TABLE OF CONTENTS (continued)

LIST OF ILLUSTRATIONS

LIST OF ILLUSTRATIONS (continued)

LIST OF ILLUSTRATIONS (continued)

LIST OF TABLES

LIST OF SYMBOLS

$\bar{A}$	Polarized light vector (Figure 8)
A	Magnitude of polarized light vector
$\bar{A}_1, \bar{A}_2$	Light vectors along p and q directions (Figure 8)
$\bar{A}_3, \bar{A}_4$	Light vectors along OX direction (Figure 8)
A*	Slide (Figure 5)
B	Point where light enters the photoelastic model (Figures 1 and 2)
B*	Slide (Figure 5)
$\bar{C}$	Stress-optical constant, psi/fringe/inch
D	Diameter of calibration circular disc (Figure 11), inches
h	Thickness of calibration circular disc (Figure 11), inches
I	Intensity of scattered light
L_1, L_2	Lens system in slide A* to choose between pencil or ribbon light operation (Figure 5)
L_4, L_5	Lens system which expands the light beam to 0.6 inch (Figure 5)
L_6/L_7	Lens system which expands the light beam to 1.5 inches (Figure 5)
$\ell_1=\cos\theta$	Direction cosine of X′ axis relative to X axis (Figure 10)
M, M_1, M_2	Points of observation inside the photoelastic model (Figures 2 and 6)
$m_1=0$	Direction cosine of X′ axis relative to Y axis (Figure 10)
$\bar{M}$	Uniform bending moment applied to the four-point bending specimen, inch-lbs
N=N(Z)	Scattered-light photoelastic fringe order (number) along Z axis
$\bar{N}=\bar{N}(Z')$	Scattered-light photoelastic fringe order along Z′ axis

$n_1=-\sin\theta$	Direction cosine of X′ axis with respect to Z axis (Figure 10)
O	Station chosen in four-point bending specimens or F-16 canopy where secondary principal stresses were determined (Figures 9, 10, 28)
$\bar{O}$	Observer's eye position in scattered-light polariscope (Figure 2)
P	Light conditioner/polarizer (Figures 1 and 2)
$\bar{P}$	Applied load in four-point bending specimen, lbs
p	Maximum secondary principal stress along x axis determined by scattered-light photoelasticity, psi (Figure 10)
P_b	Maximum secondary principal stress determined by beam theory, psi
P_s	Maximum secondary principal stress determined by strain gages, psi
P*	Maximum secondary principal stress along X′ axis, psi (Figure 10)
q	Minimum secondary principal stress along y axis, psi (Figure 10)
Q	Diametrical compression load applied to the calibration circular disc, lbs (Figure 11)
Q_1, Q_2	Quarter wave plates (Figure 5)
S	Light source (Figure 2)
$T=\Delta Z$	Thickness or length of light path inside the photoelastic model between points of measurement M_1M_2, inch (Figures 2 and 8)
t	Time, seconds
β	Angle of polarizer relative to X axis, radians (Figure 8)

δ	Relative linear retardation between light vectors oriented along the two secondary prinipal stress directions after light travels through the thickness T($-\Delta Z$) (Figure 8), inches
ϕ	Phase angle (shift) of retardation = $2\pi\delta/\lambda$, radians
λ	Wavelength of light, nm Green = 546.1 nm Red = 632.8 nm
ω	Angular velocity of polarized light, rad/sec
σ_1, σ_2	Principal stresses at the center of calibration circular disc along X and Y axes (Figure 11)
$\begin{matrix}\sigma_x & \tau_{xy} & \tau_{xz} \\ \tau_{yx} & \sigma_y & \tau_{yz} \\ \tau_{zx} & \tau_{zy} & \sigma_z\end{matrix}$	Stress tensor at any general point in a stressed model, psi
$\theta, \theta+90$	Direction of maximum secondary principal stress p and minimum secondary principal stress q relative to X-axis, radians (Figure 8)
θ_x	Rotation about x axis produced by rotation mechanism, degrees (Figure 3)
θ_y	Rotation about y axis produced by rotation mechanism, degrees (Figure 3)
$\bar{\theta}$	Angle the direction of light makes with the vertical direction

SECTION 1
INTRODUCTION

1.1 BACKGROUND INFORMATION

A detailed literature search and review on scattered-light photoelasticity was reported in Reference 1. Some of the earlier work on scattered-light photoelasticity was performed by Weller [2,3] in the United States and Jessop [4] in the United Kingdom, but a systematic study of the analysis and experiments was initiated by Frocht and Srinath [5-8]. Cheng [9-12] has described a technique for determining the directions of the secondary principal stresses and their difference without using a compensator but still capable of obtaining the same degree of accuracy. Cheng [12] has reported experiments conducted on an aircraft windshield sample having a three layer (glass-vinyl-glass) sandwich structure. Swinson et al. [13-18] have applied scattered-light methods to transient thermal stress problems in a solid propellant rocket motor and to three-dimensional dynamic stress analysis problems; they have outlined methods to determine the state of stress on a free surface and the direction of the maximum secondary principal stress axis in a scattered-light photoelastic analysis.

The application of surface waves to internal stress determinations has been reported for metallic materials (Reference 1). Wave velocity is only slightly influenced by stress level and so very high accuracy in measurements is required. Furthermore, there are structural factors which influence the velocity and may mask velocity variations due to the presence of a stress.

The application to polymeric materials has the additional problem in that methods for launching and receiving surface waves

in these materials are not well established. Dean (References 25 and 26) has applied acoustic surface waves to measure the residual stresses in acrylic plastics. By using a special surface wave transducer the influences of internal stress, molecular orientation, physical aging, and water content on the acoustic surface wave velocity were studied.

In Reference 27 an acoustical-ultrasonic technique was used to demonstrate that relationships exist between changes in attenuation of stress waves and tensile stress for an 8-ply 0° graphite-epoxy fiber reinforced composite. Changes in attenuation were measured as a function of tensile stress in the frequency domain and in the time domain.

1.2 PROGRAM OBJECTIVE

Experience has shown that surface crazing of monolithic plastic transparencies, and surface crazing and delamination of laminated plastic transparencies, are related to the surface stress levels in the transparency. It has been theorized that control of this stress level to a critical threshold value (during the manufacturing and installation process) may increase the transparency's service life by delaying the need to remove them due to either of these stress induced failure modes. Therefore, the capability to measure the level of residual stresses in aircraft transparencies is important. Methods for determining these stresses need to be nondestructive, thus permitting measurements on installed aircraft transparencies. At present, nondestructive methods to quantify the residual stresses in aircraft transparencies are unknown.

The primary objective of this investigation was the laboratory evaluation of scattered-light photoelasticity and surface wave ultrasonics as nondestructive techniques to measure stresses in monolithic and laminated transparencies constructed

with polycarbonate and/or acrylic materials. A secondary objective was to evaluate the potential for adapting these techniques to measuring stress levels in fleet aircraft at operational bases. Five tasks defined to meet these objectives are as follows:

- Task 1: Design, fabricate, and set up a scattered-light photoelastic test facility capable of measuring residual stresses in aircraft transparencies.

- Task 2: Evaluate the accuracy of the technique by conducting experiments on four-point bending polycarbonate specimens having known analytical and experimental solutions.

- Task 3: Establish a scattered-light photoelastic experimental procedure for monolithic polycarbonate F-16 transparency by measuring residual stresses at a typical station.

- Task 4: Evaluate the scattered-light photoelastic properties of acrylic plastic material.

- Task 5: Measure the residual stresses in the outer ply of the F-16 laminated canopy using the acoustic surface wave ultrasonic technique.

SECTION 2
SCATTERED-LIGHT PHOTOELASTICITY

2.1 PRINCIPLES OF SCATTERED-LIGHT PHOTOELASTICITY

When a light ray propagates through a transparent body, a small portion of light scatters (Figure 1). A particle M, excited by an electromagnetic vibration, behaves as a secondary light source that will emit or scatter electromagnetic vibrations in all possible directions [19,20]. The scattered-light ray M-$\bar{O}$ in the direction perpendicular to the original wave S-M is polarized; that is, all electromagnetic vibrations are contained in a single plane. This polarizing effect enables the use of scattered light in photoelasticity. By placing a polarizer (light conditioner) P between the light source S and the model, the photoelastic effect accumulated between points B and M can be measured.

The scattered-light photoelastic effect can be measured by placing the transparent model or part in a tank filled with a liquid of the same index of refraction as the transparent body (Figure 2). The model is then subjected to the specified loads and forces. The light emerging from the source S is polarized by means of the light conditioner P, and conditioned to form a thin pencil- or ribbon-like beam propagating along SZ. The observer $\bar{O}$ sees light scattered in a direction perpendicular to the direction of propagation. Since every particle M scatters light and also acts as an analyzer, the observer looking at different points (M_1, M_2,...) along SZ will see the following:

- The scattered light coming from point M_1 which contains the photoelastic effect integrated from B to M_1.
- The scattered light from point M_2 which contains the photoelastic effect integrated from B to M_2.

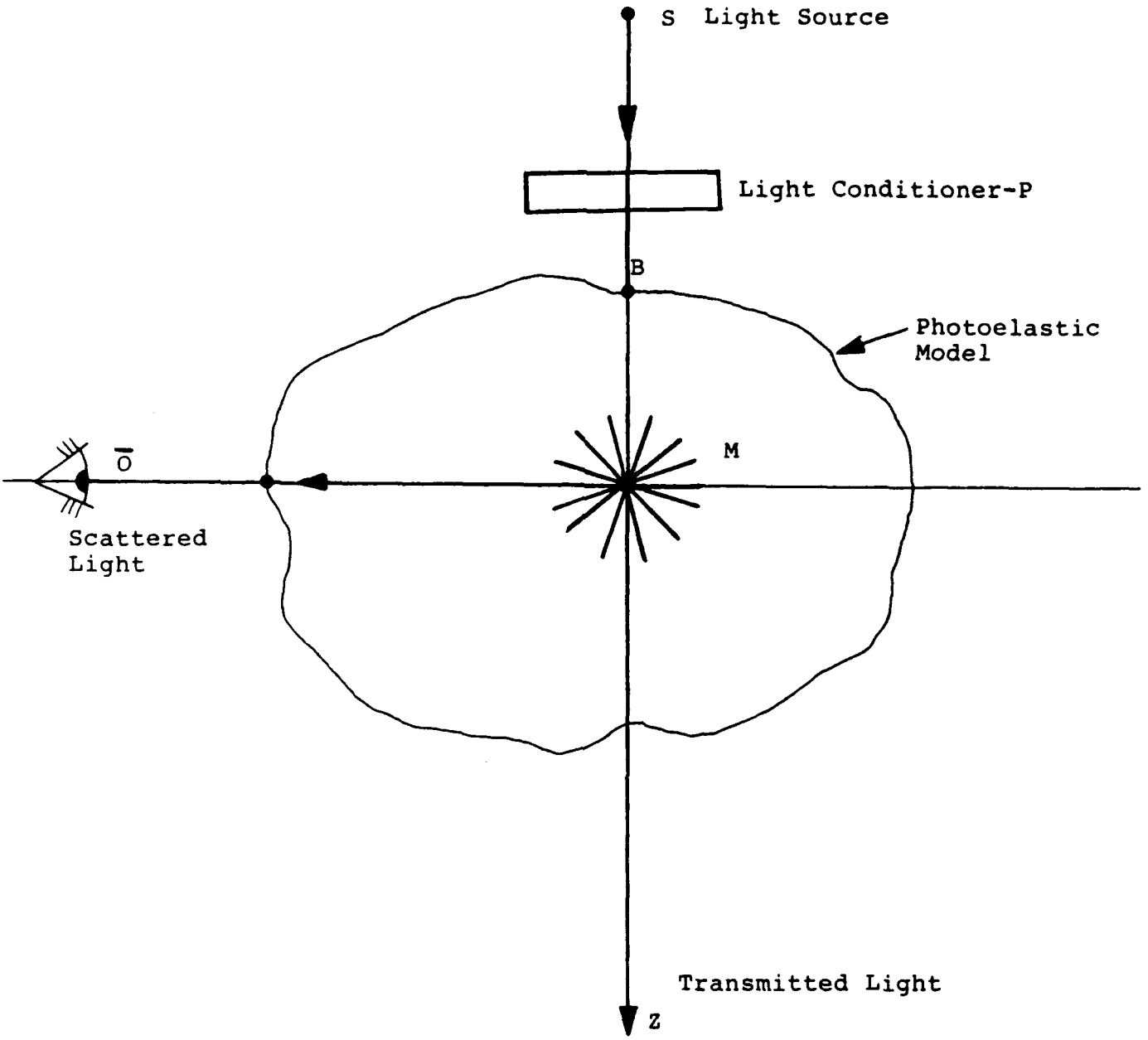

Figure 1. Scattering of Light by a Transparent Body.

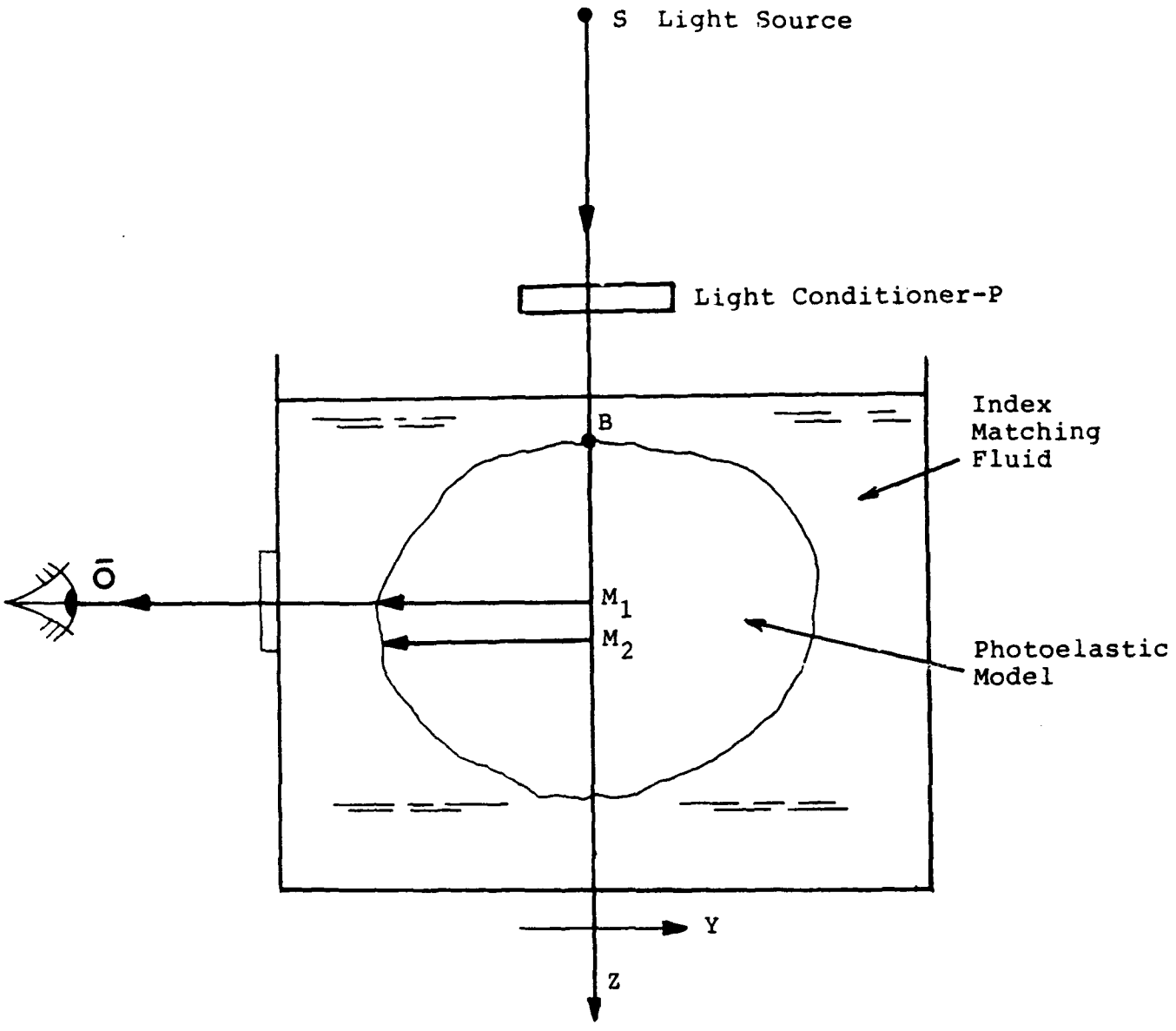

Figure 2. Schematic View of Scattered-Light Polariscope

The difference between the measured values at M_1 and M_2 is due to stresses in the M_1M_2 layer, and therefore is a measure of stresses in the M_1M_2 layer. The photoelastic effect (or relative retardation) that accumulates during the light passage is of the same nature as in conventional photoelasticity. A polarized light wave propagating through a layer of thickness M_1M_2 (ΔZ) splits into two waves, propagating at different speeds and polarizing in the direction of the secondary principal stresses p and q. (The secondary principal stresses p and q are the maximum and minimum normal stresses in the plane perpendicular to the ray SZ.)

The relative retardation between these waves is

$$\Delta\delta = \Delta N\lambda \tag{1}$$

where λ is the wavelength of light and N is the fringe order. This produces interferences that are analyzed by the observer, namely

$$dN = \frac{\Delta\delta}{\lambda} = (p-q)\ \frac{\Delta Z}{\bar{C}} \tag{2}$$

where $\bar{C}$ is the stress-optical constant of the material and ΔZ is the thickness of the layer crossed.

2.2 SCATTERED-LIGHT PHOTOELASTIC TEST FACILITY

The scattered-light photoelastic test facility used to conduct the experimental investigation is located at UDRI and consists of the following elements:

- support fixture
- light source and light conditioning system

- data acquisition system
- specimen

2.2.1 Support Fixture

The support fixture consists of:

- adjustable gantry which supports the rest of the test fixture (Figure 3).

- X-, Y-, and Z-translation mechanisms which permit the motions of the light conditioning system and the data acquisition system in these directions. These motions can be controlled and measured to an accuracy of 0.01 inch. The X-Y translation is used to locate X-Y coordinate lines within the model to be analyzed (Figures 3 and 4) if the shear difference method is used to separate the secondary principal stresses.

- θ_x and θ_y rotation mechanisms, which permit rotary motions of the light conditioning and data acquisition systems in these directions. Motions can be controlled and measured to an accuracy of one degree. These rotation motions were used in the separation of secondary principal stresses.

2.2.2 Light Source and Light Conditioning System

The light source and light conditioning system were manufactured by the Photoelastic Division of Measurements Group Inc. The functions of the various components of the system are described below.

- The light is supplied by a helium/neon laser, providing collimated light of 632.8 nm wavelength (Figures 3 and 5).

- By means of the lens system L_1/L_2, one can choose between a pencil operation (light converging toward a point on the model) or a ribbon operation (light converging into a plane of zero thickness). A sliding indexed mount enables the

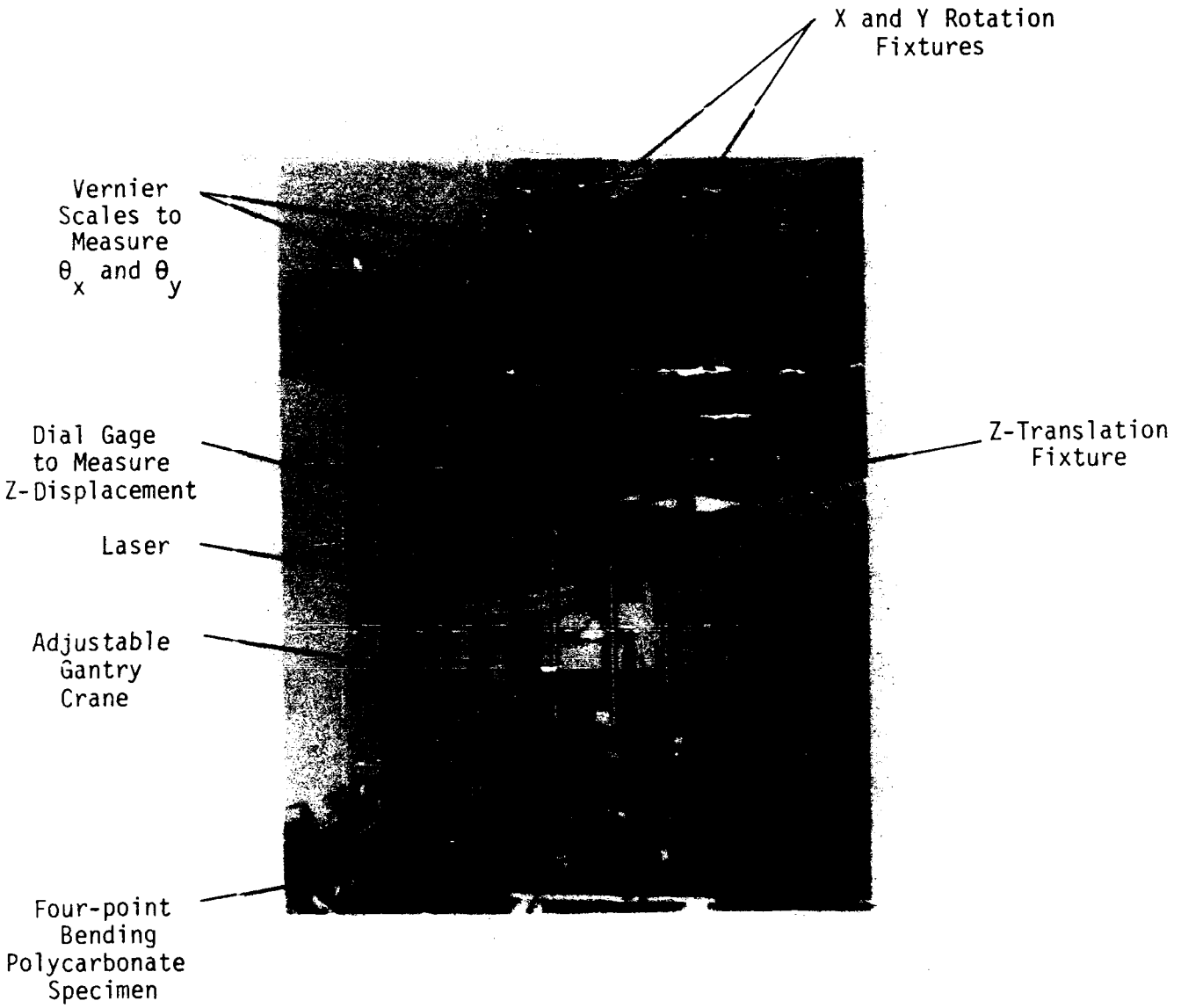

Figure 3. Scattered-Light Photoelastic Test Facility.

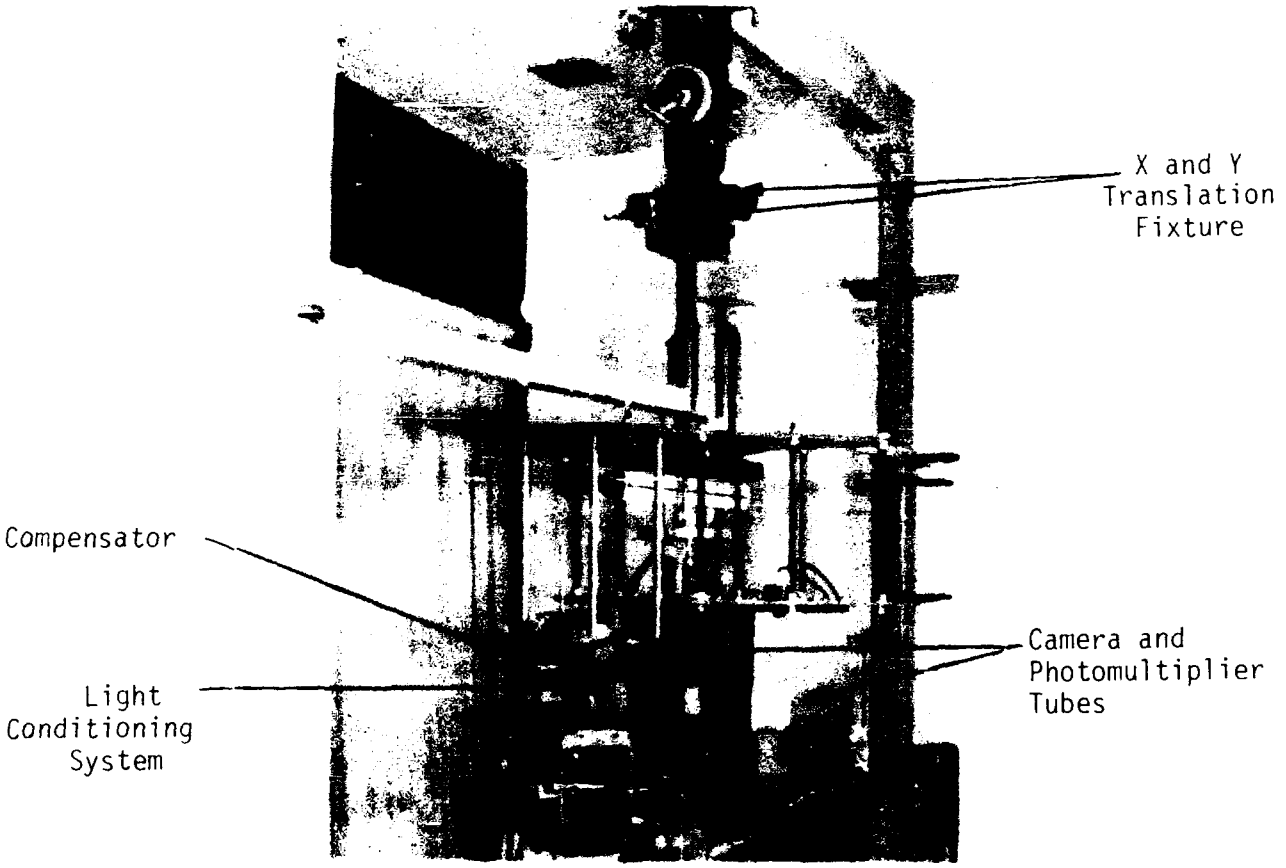

Figure 4. Scattered-Light Photoelastic Test Facility.

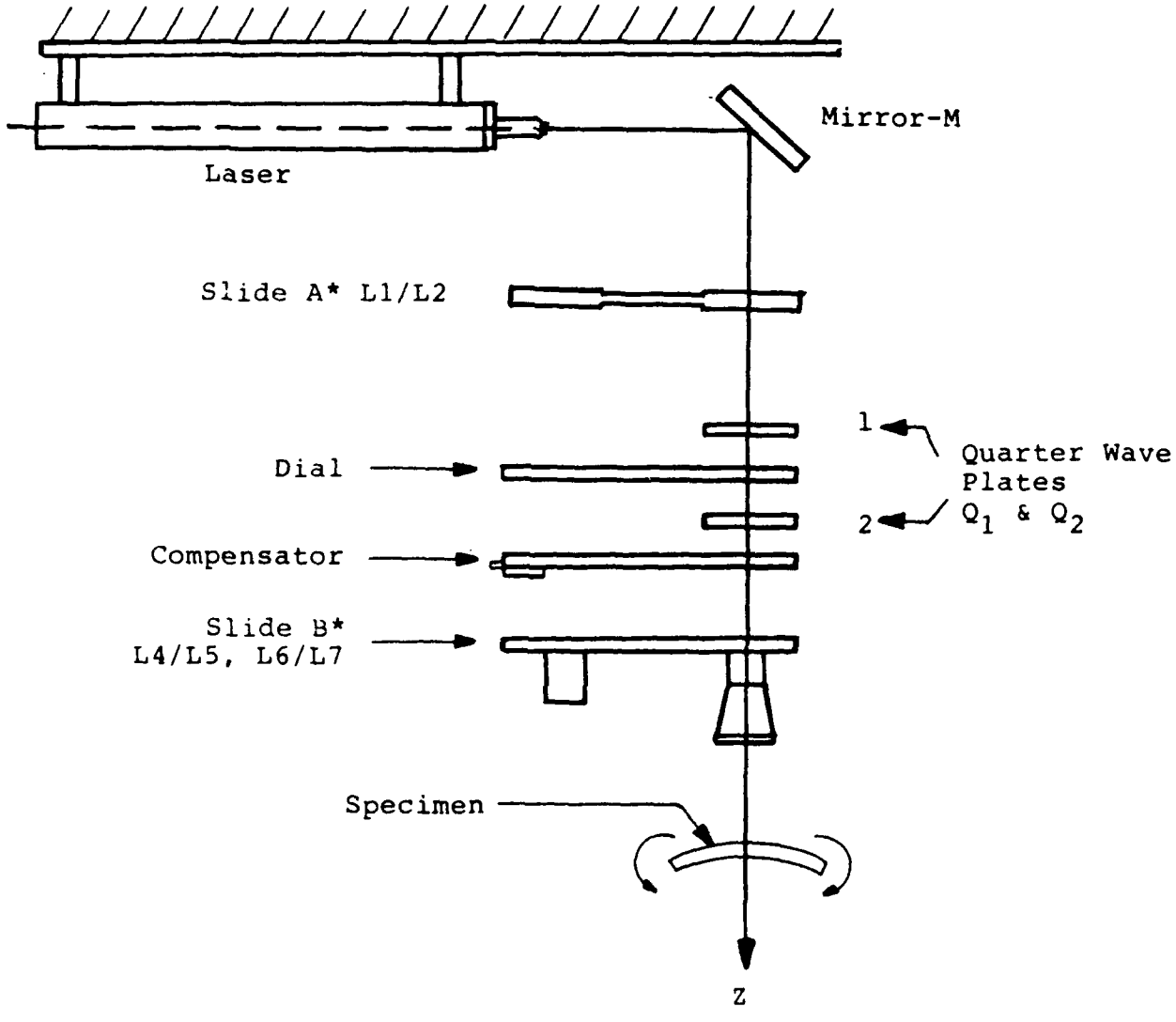

Figure 5. Schematic View of Light Source and Light Conditioning System

selection of light desired (Figure 5). The position of the sliding mount can be adjusted along the light path such that a converging light beam with a node approximately 15 to 20 inches below these lenses is produced.

- The ribbon of light can be expanded by manipulation of the lens system L_4/L_5 and L_6/L_7 in order to obtain better photographic records and for easier observation of the fringe patterns. The L_4/L_5 lens system expands the light beam to 0.60 inches and the L_6/L_7 lens system expands the light beam to 1.5 inches. The beam generated by the laser is plane-polarized and the plane of polarization coincides with the vertical symmetry plane of the laser. Insertion of the quarter-wave plate Q1 produces circular polarization. A second quarter-wave plate transforms the light back into plane polarization. The second quarter-wave plate Q2 is mounted in a rotatable mount, and its motion is indexed on a large graduated dial indicating the direction of emerging polarization.

- The compensator is a Babinet-Soleil digital readout uniform field compensator, and its measuring accuracy determines the sensitivity of the system. The retardation can be adjusted by rotation of a lead screw which is connected to a calibrated counter. The counter indicates the retardation, which is 105 counts per fringe for the laser light used in the scattered-light device. The compensator axes coincide with its length and width.

2.2.3 Data Acquisition System

The data acquisition system, manufactured by the Photoelastic Division of Measurements Group Inc., was used to collect the photoelastic information from the model being tested. Three different methods of acquiring the data were provided (Figures 6 and 7). They are:

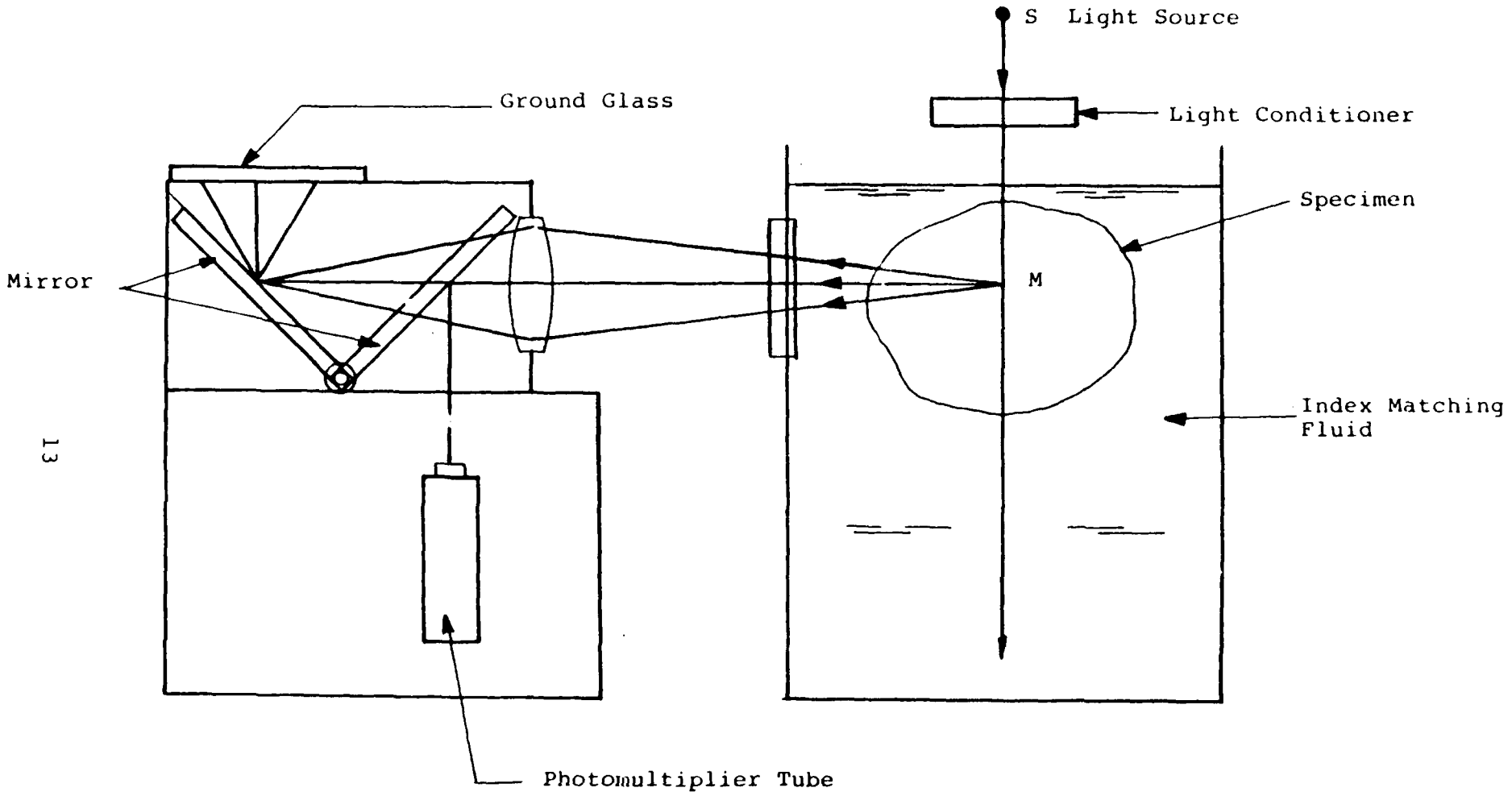

Figure 6. Data Acquisition System.

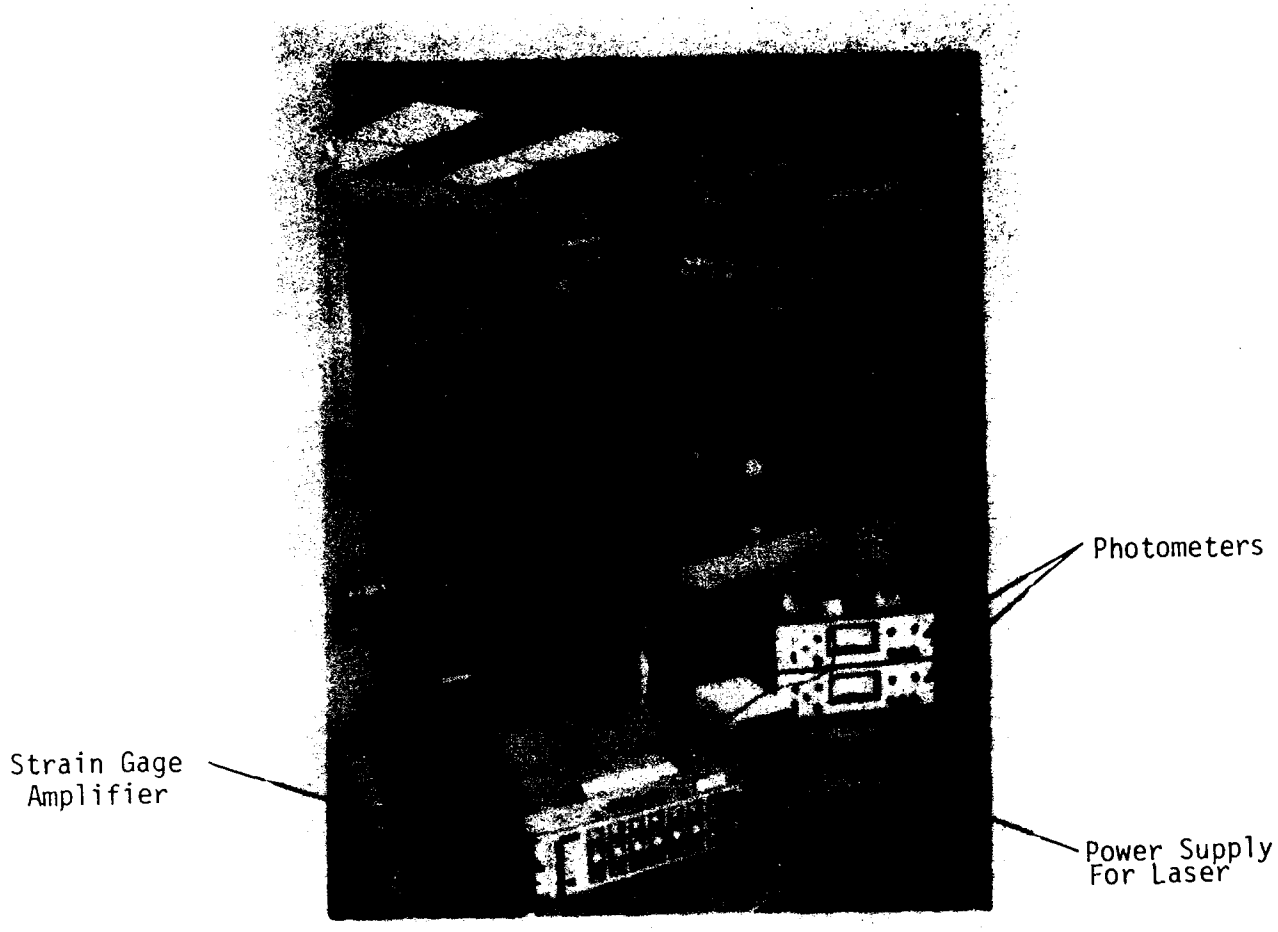

Figure 7. Scattered-Light Photoelastic Test Facility.

- Visual - the photoelastic pattern is directly observed on a ground glass screen.

- Photographic - a photographic record of the observed pattern is made on cut or Polaroid 4x5 film.

- Photoelectric - a photomultiplier tube is incorporated in the data acquisition system which provides an electrical output proportional to the light intensity emerging from the observed scattered-light photoelastic fringe pattern. The distance between fringes can be very accurately determined by photoelectric measurement. A photometer measures the light intensity (Figure 7).

2.3 THEORY OF SCATTERED-LIGHT PHOTOELASTICITY

Light emerging from the light conditioning system is polarized and propagates in direction Z. The polarized light vector can be represented (Figure 8(a)) by equation:

$$\bar{A} = A \cos\omega t \qquad (3)$$

The reference axes X-Y in the plane perpendicular to Z are selected as follows.

- The direction X coincides with the analyzer effect ($M\bar{O}$ perpendicular to MX)

- The direction of MY coincides with $M\bar{O}$.

- β is the angle of the polarizer to OX.

- θ is the direction of maximum secondary principal stress p with reference to X.

When the beam of light arrives at the stressed body, it splits into two waves, polarized and vibrating in the p and q planes, respectively (Figure 8):

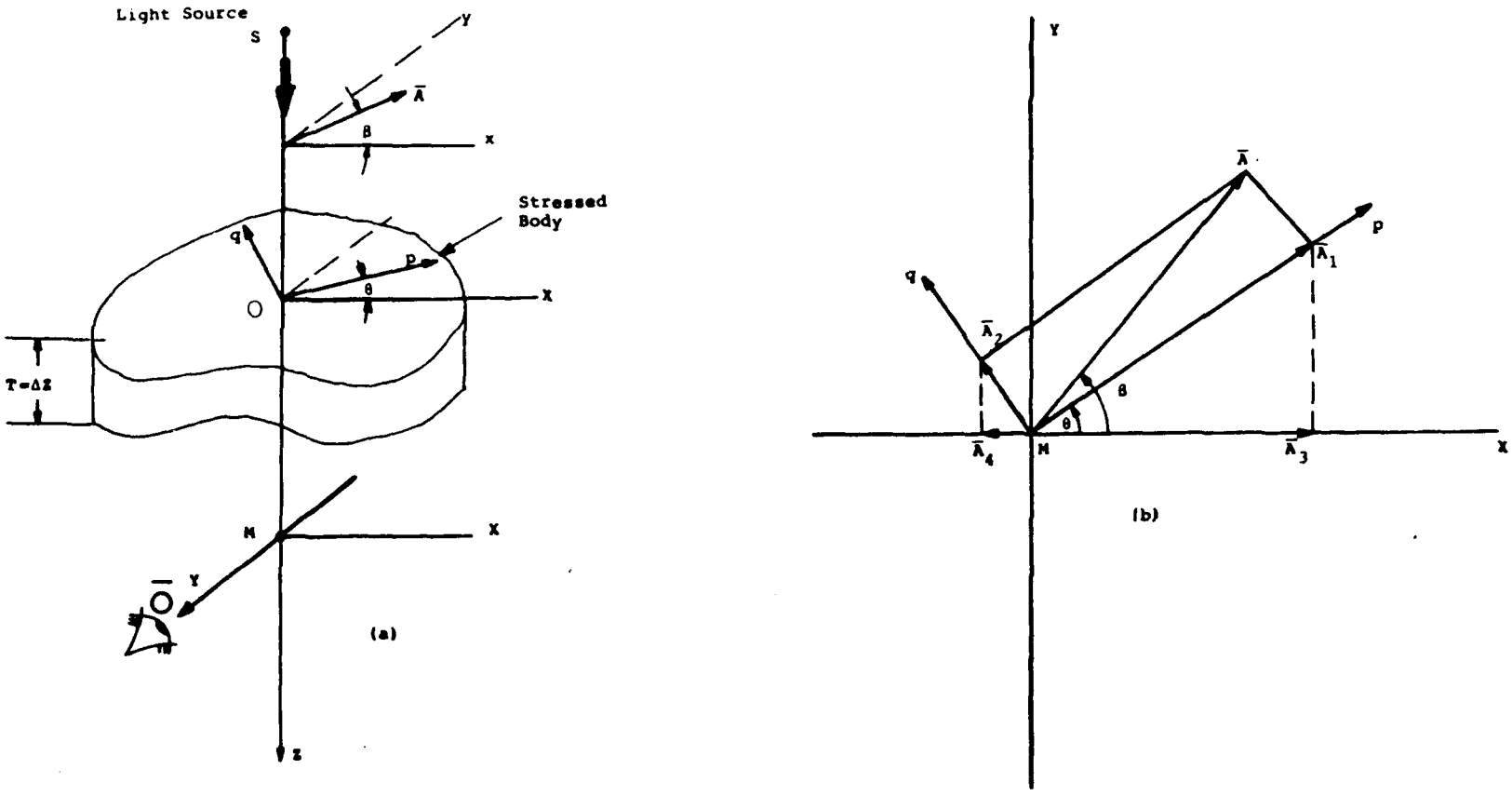

Figure 8. Schematic of Light Propagation Through a Stressed Body.

- in the p-plane: $A \cos(\beta-\theta) \cos\omega t$
- in the q-plane: $A \sin(\beta-\theta) \cos\omega t$

The two waves propagate at different velocities, and their relative retardation increases with travel. The increase in retardation after crossing $T=\Delta Z$ is:

$$\Delta\delta = \Delta N\lambda = \frac{\lambda T}{\bar{C}} (p-q) = \frac{\lambda \Delta Z}{\bar{C}} (p-q) \qquad (4)$$

The resulting angular phase shift after crossing thickness ΔZ is:

$$\phi = \frac{2\pi\delta}{\lambda} \qquad (5)$$

The components arriving at the analyzer at point M are:

$$\bar{A}_1 = A \cos(\beta-\theta) \cos\omega t \qquad (6)$$
$$\bar{A}_2 = A \sin(\beta-\theta) \cos(\omega t+\phi) \qquad (7)$$

The intensity of light observed at this point will be the same as if a polarizing filter (analyzer) with its axis coinciding with MX was placed there. Projecting the two waves on the analyzer (which is always along the X direction and not rotatable) as in Figure 8(b), the following equations result:

$$\bar{A}_3 = A \cos(\beta-\theta) \cos\theta \cos\omega t \qquad (8)$$
$$\bar{A}_4 = A \cos(\beta-\theta) \sin\theta \cos(\omega t+\phi) \qquad (9)$$

and the relative phase difference between these two waves is ϕ. The resulting light intensity is then [19,20]:

$$I = \frac{A}{2} [1+\cos 2(\beta-\theta) \cos 2\theta - \sin 2((\beta-\theta) \sin 2\theta \cos\phi] \qquad (10)$$

2.3.1 Visual Observation and Photographic Recording

For visual observation and photographic recording, the polarizer and analyzer will usually be crossed so that $\beta=90°$. The light intensity expression will then be similar to a transmission polariscope operation:

$$I = \frac{1}{2}(1-\cos\phi)\ \sin^2 2\theta \qquad (11)$$

When the illuminated ribbon is observed, dark fringes will be seen when $\cos\phi=1$ or

$$\phi = 0,\ 2\pi,\ 4\pi,\ldots,2N\pi,$$
$$\delta = 0,\ \lambda,\ 2\lambda,\ldots,N\lambda \qquad (12)$$

where N is the fringe order. Light intensity becomes zero, and full-order dark fringes are observed. The light intensity becomes maximum when:

$$\cos\phi = -1 \text{ or}$$

$$\phi = \pi,\ 3\pi,\ 5\pi,\ldots,(2N-1)\pi \qquad (13)$$

$$\delta = \frac{\lambda}{2},\ \frac{3}{2}\lambda,\ \frac{5}{2}\lambda,\ldots,\frac{(2N-1)}{\lambda}$$

where N is the fringe order. Half-order light fringes are observed. When the model rotates, the angle θ between the maximum secondary stress p and the x-y axes changes. When $\theta=0$, the principal directions in the X-Y plane coincide with the X-Y axes, the light intensity becomes zero, and an isoclinic is observed. The secondary principal stress direction can thus be determined. The highest contrast (highest light intensity of half-order light fringes) is obtained when

$$\sin 2\theta = \pm 1 \text{ or } \theta = \pm\frac{\pi}{4} + n.90° \tag{14}$$

where n=1,2,3,..., that is, when the direction of secondary principal stresses is at 45° to the axes of polarizer X-Y.

2.4 METHOD TO SEPARATE THE SECONDARY PRINCIPAL STRESSES

The method of separating the secondary principal stresses [13] (Figure 13) can be illustrated for the case of bending stresses in a four-point bending specimen. The equation for the stress optic law is given by (Figure 9):

$$p-q = \bar{C}\,\frac{dN}{dZ} \tag{15}$$

When the laser is directed at $\bar{\theta}$ to the vertical (Figure 10), the equation for the stress optic law takes the following form:

$$\pm(p^*-q) = \bar{C}\,\frac{d\bar{N}}{dZ}, \tag{16}$$

The direction cosines of OX′ are

$$\begin{aligned} \ell_1 &= \cos\bar{\theta} \\ m_1 &= 0 \\ n_1 &= -\sin\bar{\theta} \end{aligned} \tag{17}$$

Equation 16 takes positive values if p*>q and negative values if p*<q, which can be evaluated by noting the direction of the maximum secondary principal axis which is discussed next.

$$p^* = \sigma_x \ell_1^{\,2} + \sigma_y m_1^{\,2} + \sigma_z n_1^{\,2} + 2\sigma_{xy}\ell_1 m_1 + 2\sigma_{xz}\ell_1 n_1 + 2\sigma_{yz} m_1 n_1 \tag{18}$$

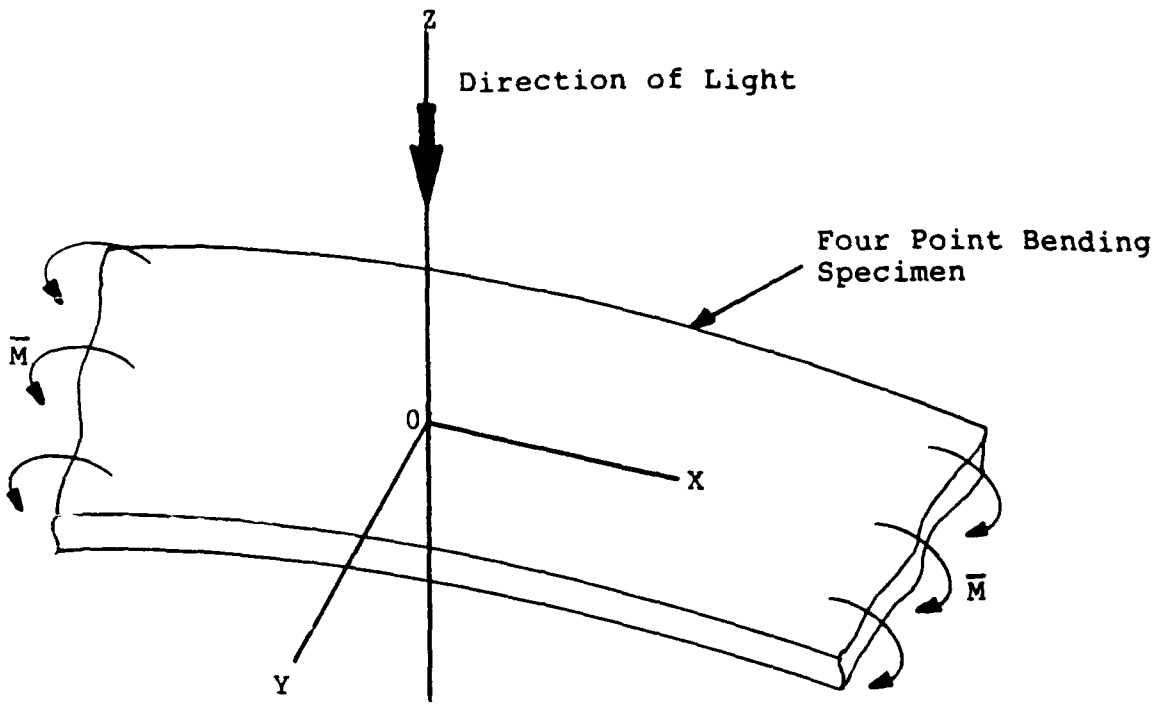

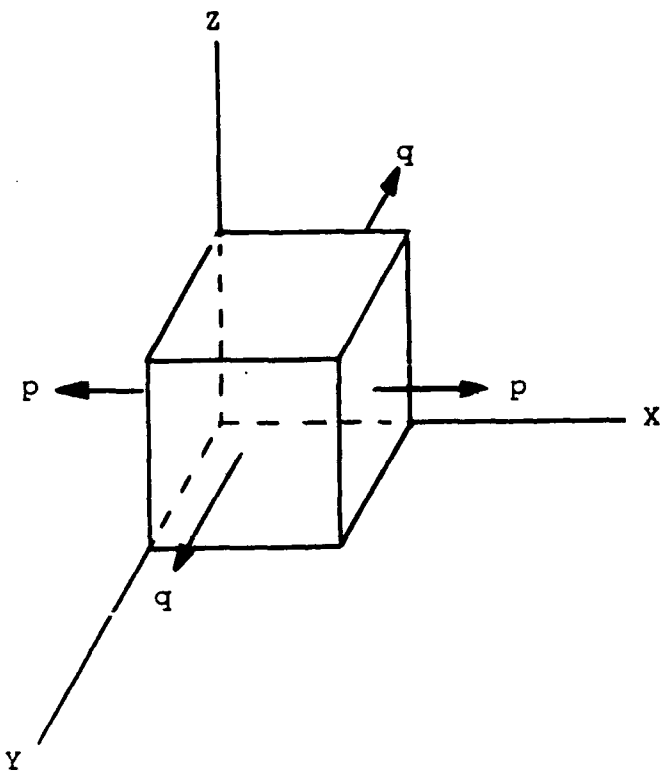

Figure). The Secondary Principal Stresses in an Element at '0' Near the Top Edge When the Light is Directed Vertically.

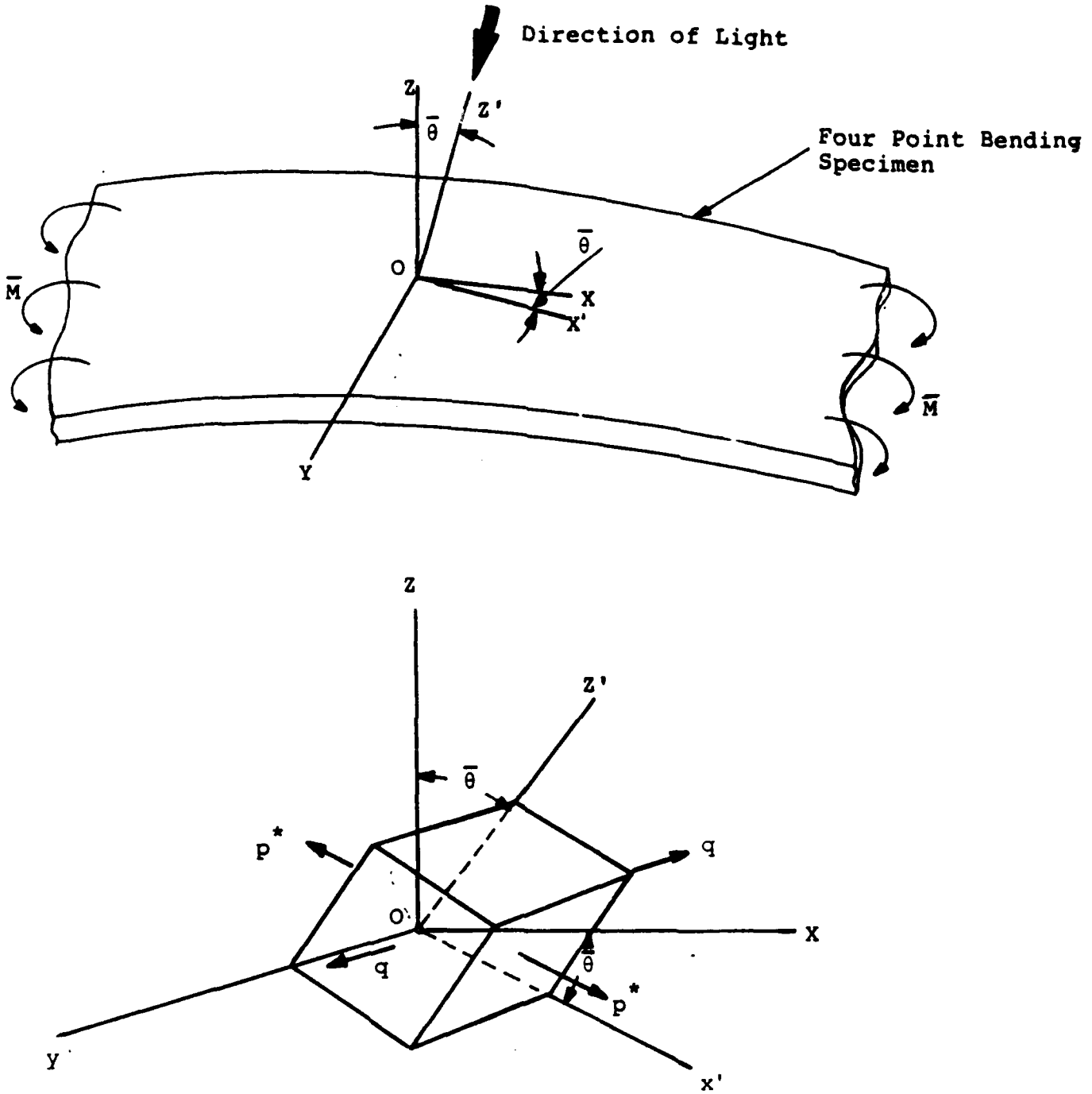

Figure 10. **The Secondary Principal Stresses in element at '0' Near the Top Edge When the Light is Directed at an Angle 'θ' with the Vertical.**

At the surface of the beam,

$$\sigma_z = \sigma_{xz} = \sigma_{yz} = 0$$

$$\sigma_x = p,\ \sigma_y = q,\ \sigma_{xy} = 0 \tag{19}$$

Therefore, the value of p* reduces to

$$p^* = p \cos^2\theta \tag{20}$$

Solving Equations 15, 16, and 20 for p and q,

$$p = \frac{\bar{C}\left(\frac{dN}{dZ} \mp \frac{d\bar{N}}{dZ},\right)}{\sin^2\bar{\theta}} \tag{21}$$

$$q = p - \bar{C}\frac{dN}{dZ} \tag{22}$$

Positive values of p and q obtained from solving Equations 21 and 22 indicate the stresses are tensile while the negative values indicate the stresses to be compressive.

2.5 METHOD TO DETERMINE THE DIRECTION OF MAXIMUM OR MINIMUM SECONDARY PRINCIPAL STRESSES BY USE OF COMPENSATOR

The direction of secondary principal axes can be determined by rotating the model until the fringe patterns disappear completely, but this technique does not indicate which of the axes is maximum or minimum. A method [18] to determine the direction of maximum or minimum secondary principal stress is presented in the following paragraphs.

When a compensator such as the Soliel-Babinet is introduced into the light path and aligned with its axis along the direction of maximum secondary principal axis p, the equations for the two components of light waves as they arrive at the stressed body become (Figure 8):

$$\begin{aligned} &\cos(\beta-\theta)\ \cos(\omega t+\Delta\phi) \quad \text{in the p plane} \\ &\sin(\beta-\theta)\ \cos\omega t \qquad\quad \text{in the q plane} \end{aligned} \tag{23}$$

where $\Delta\phi$ is the small amount of angular phase shift introduced by the compensator. These two waves propagate at different velocities, and their relative retardation increases with travel. The fast axis for many photoelastic materials is the maximum secondary principal stress axis. Then the components arriving at the analyzer at point M are

$$\begin{aligned} &\cos(\beta-\theta)\ \cos(\omega t+\Delta\phi) \\ &\sin(\beta-\theta)\ \cos(\omega t+\phi) \end{aligned} \tag{24}$$

The phase difference between these two waves is $\phi-\Delta\phi$. The intensity of light can be expressed as

$$I = \frac{A}{2}\,[1-\cos(\phi-\Delta\phi)]\,\sin^2 2\theta \tag{25}$$

If the angle of observation is fixed at 45°, Equation 25 reduces to

$$I = \frac{A}{4}\,[1-\cos(\phi-\Delta\phi)] \tag{26}$$

Differentiating Equation 26 with respect to $\Delta\phi$, we get

$$\frac{dI}{d(\Delta\phi)} = -\frac{A}{4}\sin(\phi-\Delta\phi) \tag{27}$$

which gives the change of light intensity at a point due to angular phase shift $\Delta\phi$ introduced by the compensator along the direction of the maximum secondary principal stress. For constant intensity,

$$dI = 0 \tag{28}$$

Then,

$$\sin(\phi-\Delta\phi) = 0 \tag{29}$$

Equation 29 implies that

$$\phi-\Delta\phi = 0,\ \pi,\ 2\pi,\ldots,N\pi \tag{30}$$

but the function $\phi(Z)$ is strictly an increasing function of Z, the distance of light path (Figure 8), so that

$$\phi = \phi(Z)$$

$$\frac{d\phi}{dZ} \geq 0 \tag{31}$$

This follows from the fact that ϕ is proportional to the non-negative difference in secondary principal stresses (Equations 4 and 5). Now, let an observer view a specific point in the specimen and note the scattered-light intensity at that point. In order for the noted intensity to remain the same as angular phase shift $\Delta\phi$ introduced by the compensator, the observer must move his observation point along the light path. Mathematically expressing this view,

$$I = \text{constant} \tag{32}$$

then

$$\phi-\Delta\phi = \text{constant} \tag{33}$$

as indicated by Equation 30. Now, if the retardation is decreased by the compensator corresponding to $\Delta\phi$, then ϕ must increase, but recalling that ϕ is an increasing function of Z, then Z must increase also. This gives the appearance of the fringes moving down and away from the light source.

When the compensator axis is aligned along the minimum secondary principal stress axis q (slow axis), then the equation for the light waves as they arrive at the stressed body becomes (Figure 8):

$$\begin{aligned} &\cos(\beta-\theta)\ \cos\omega t \qquad \text{in the p plane} \\ &\sin(\beta-\theta)\ \cos(\omega t+\Delta\phi) \quad \text{in the q plane} \end{aligned} \tag{34}$$

These two waves propagate at different velocities, and their relative retardation increases with travel. The components arriving at the analyzer at point M are

$$\begin{aligned} &\cos(\beta-\theta)\ \cos\omega t \\ &\sin(\beta-\theta)\ \cos(\omega t+\phi+\Delta\phi) \end{aligned} \tag{35}$$

The phase difference between these two waves is $\phi+\Delta\phi$. Therefore, the retardation is increased by the compensator corresponding to $\Delta\phi$, therefore ϕ must decrease. Because ϕ is an increasing function of Z, then Z must decrease. This gives the appearance of fringes moving up and towards the light source.

Secondary isotropic points being points of zero retardation will remain stationary and will take the appearance of source (or sink) out of (or into) which fringes will move and can easily be observed as the retardation is changed. This effect exists for the case where the directions of the maximum and minimum secondary principal stresses interchange their identity on opposite sides of the secondary isotropic points such as in the case of a four-point bending beam.

2.6 CALIBRATION OF POLYCARBONATE AND ACRYLIC PLEX II MATERIAL

An accurate determination of stresses in a photoelastic model requires a careful calibration of the photoelastic model material. Although the value of $\bar{C}$ found in the technical literature is reasonably accurate, the stress-optical constants of photoelastic materials vary with the supplier, the batch of resin, temperature, and age of the plastic.

The calibration tests were conducted in the Stress Analysis Laboratory of the Civil Engineering and Engineering Mechanics department of the University of Dayton School of Engineering using their transmission photoelastic polariscope. The circular disc loaded in diametral compression (Figure 11) was employed as a calibration model for both the polycarbonate and acrylic material. The principal stresses σ_1 and σ_2 at the center of the disc are given by (Reference 21):

$$\sigma_1 = \frac{2Q}{\pi hD}$$

$$\sigma_2 = -\frac{6Q}{\pi hD} \qquad (36)$$

The difference in the principal stresses

$$\sigma_1 - \sigma_2 = \frac{8Q}{\pi hD} = \frac{N\bar{C}}{h}$$

Therefore, the stress-optical constant is

$$\bar{C} = \frac{8Q}{\pi DN} \qquad (37)$$

where

Q = diametral compression load, lbs.

D = diameter of disc, inches

h = thickness of disc, inches

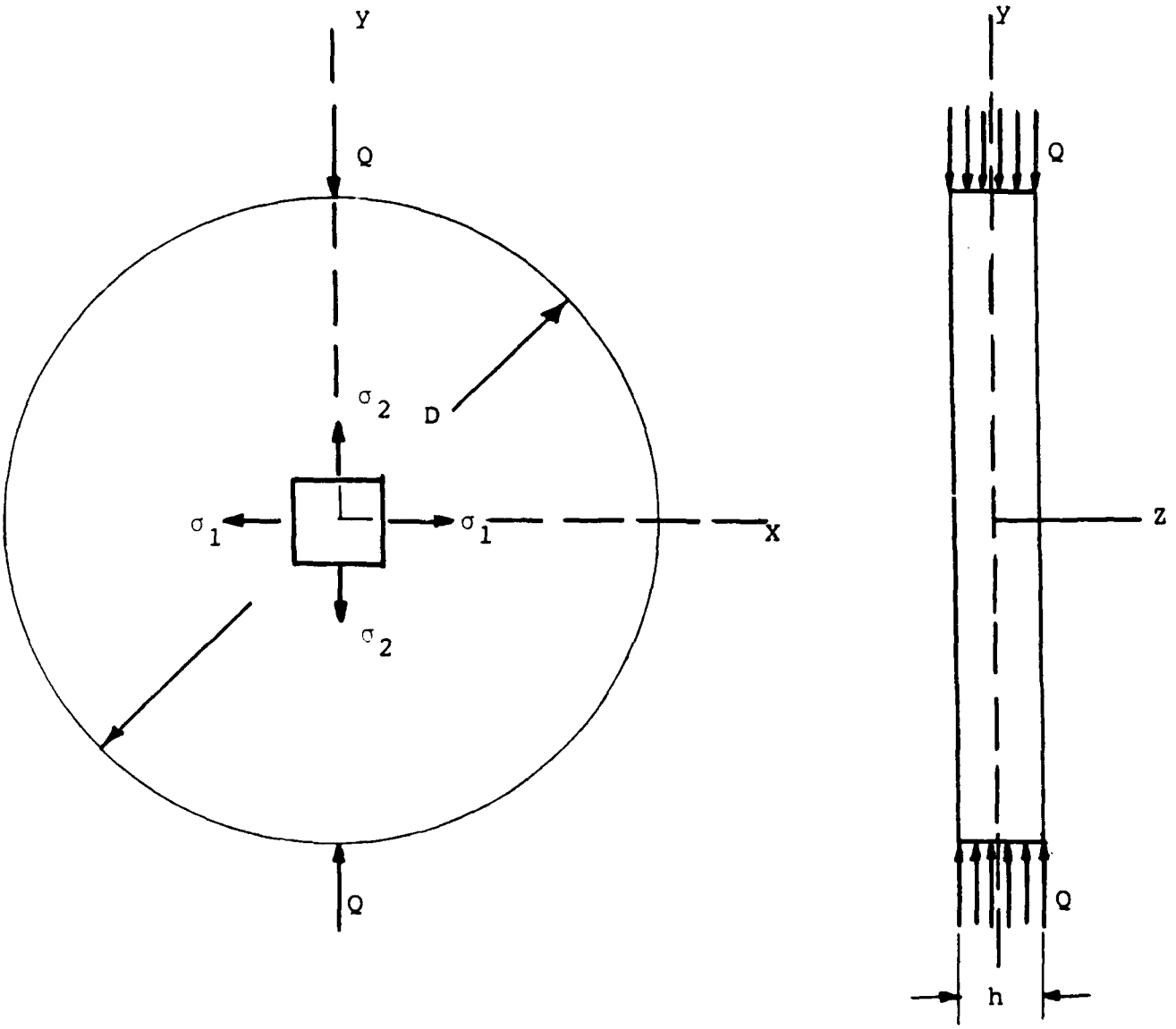

Figure 11. Circular Disc Loaded in Diametral Compression.

The calibration model was loaded in increments, and the fringe order N at the center of the disc and the applied loads were noted. A curve of the load Q was plotted as a function of N (Figure 12) and the slope of the straight line drawn through these points was used as the value of Q/N in Equation 37 to average out small errors in the reading of the load Q and the fringe order N. The value of stress-optical constants are given in Table 1. The scattered-light photoelastic technique cannot be applied to acrylic plastic material due to the poor light scattering properties and the high value for the stress-optical constant $\bar{C}$.

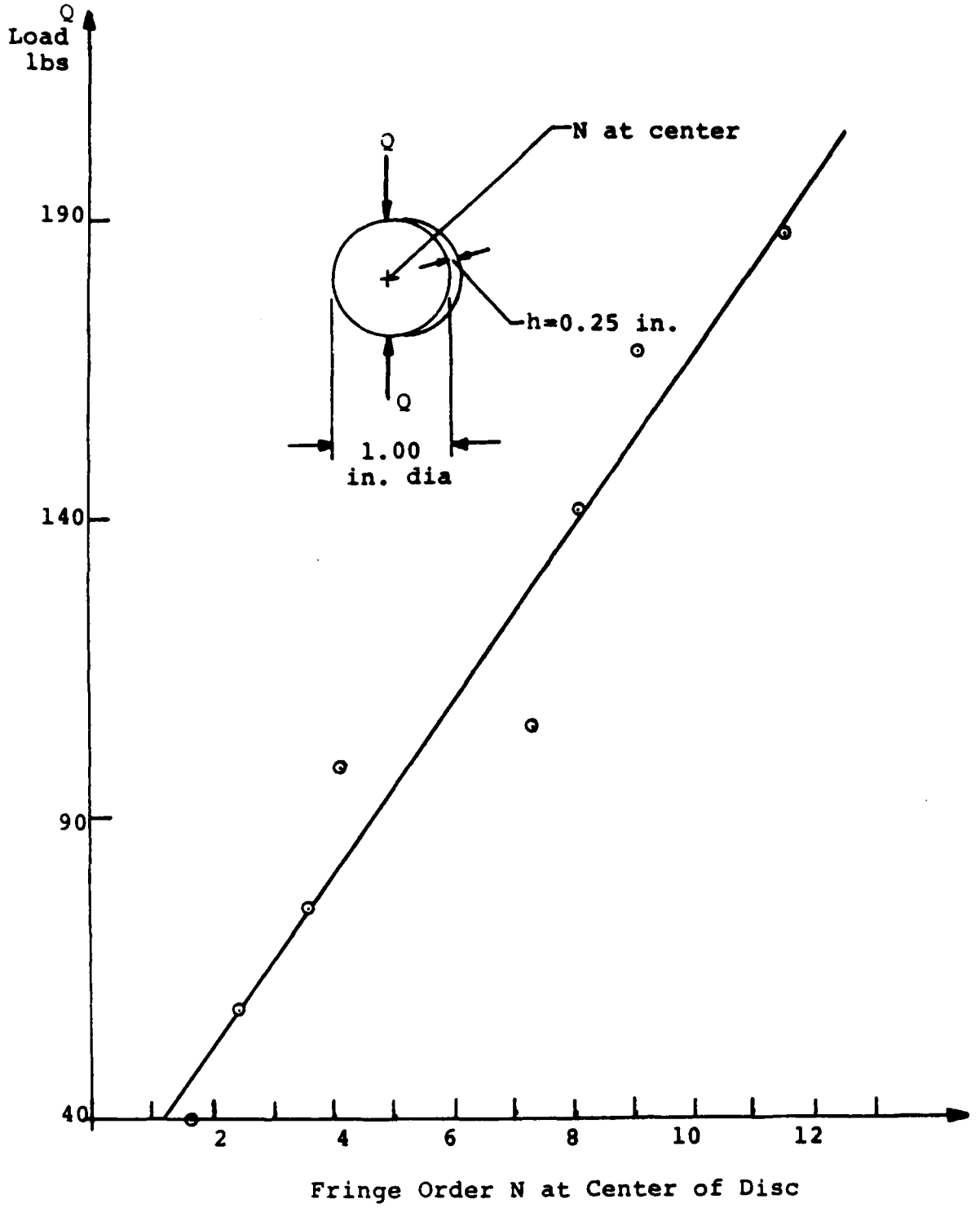

Figure 12. Typical Calibration Curve for Polycarbonate Material Obtained Using a Circular Disc Specimen in Diametral Compression.

TABLE 1

STRESS-OPTICAL CONSTANT $\bar{C}$ FOR POLYCARBONATE† AND ACRYLIC PLEX II* MATERIAL

MATERIAL	EXPERIMENTAL VALUE OF $\bar{C}$ (psi/fringe/inch)	VALUE OF $\bar{C}$ From Ref. 21, pp 486 psi/fringe/inch
Polycarbonate	41	40
Acrylic Plex II	600	-

† Commercial grade, manufactured by General Electric Company

* Supplied by Sierracin/Sylmar

SECTION 3

EVALUATION OF SCATTERED-LIGHT PHOTOELASTIC TECHNIQUE FROM TESTS ON FOUR-POINT BENDING SPECIMENS

The four-point bending experiments were conducted in order to evaluate the accuracy of the scattered-light photoelastic technique. A brief description of the four-point bending specimens and loading device is given in the following paragraphs. The tests performed during this program are summarized later in this section. Experimental procedure is described and the experimental results are presented and discussed.

3.1 TEST SPECIMENS

The dimensions of the test specimens are shown in Figure 13 and summarized in Table 2. These specimens were made from commercial grade polycarbonate manufactured by General Electric Company. One edge parallel to the length direction was polished, and the scattered-light photoelastic fringes were viewed and photographed through this edge. The opposite edge had strain gages as shown in Figure 14.

3.2 FOUR-POINT BENDING LOAD DEVICE

The four-point bending load device used in this investigation has features shown in Figures 15 and 16. The description of the four-point bending loading device is given in Reference 22.

3.3 STRAIN GAGE INSTRUMENTATION

Seven Micromeasurements WA-13-060WT-120 2 element 90° 'Tee' stacked rosettes were installed on the edge, and in the center back-to-back on the front and rear surfaces of the test specimen shown in Figures 14 and 15. These strain gage circuits were

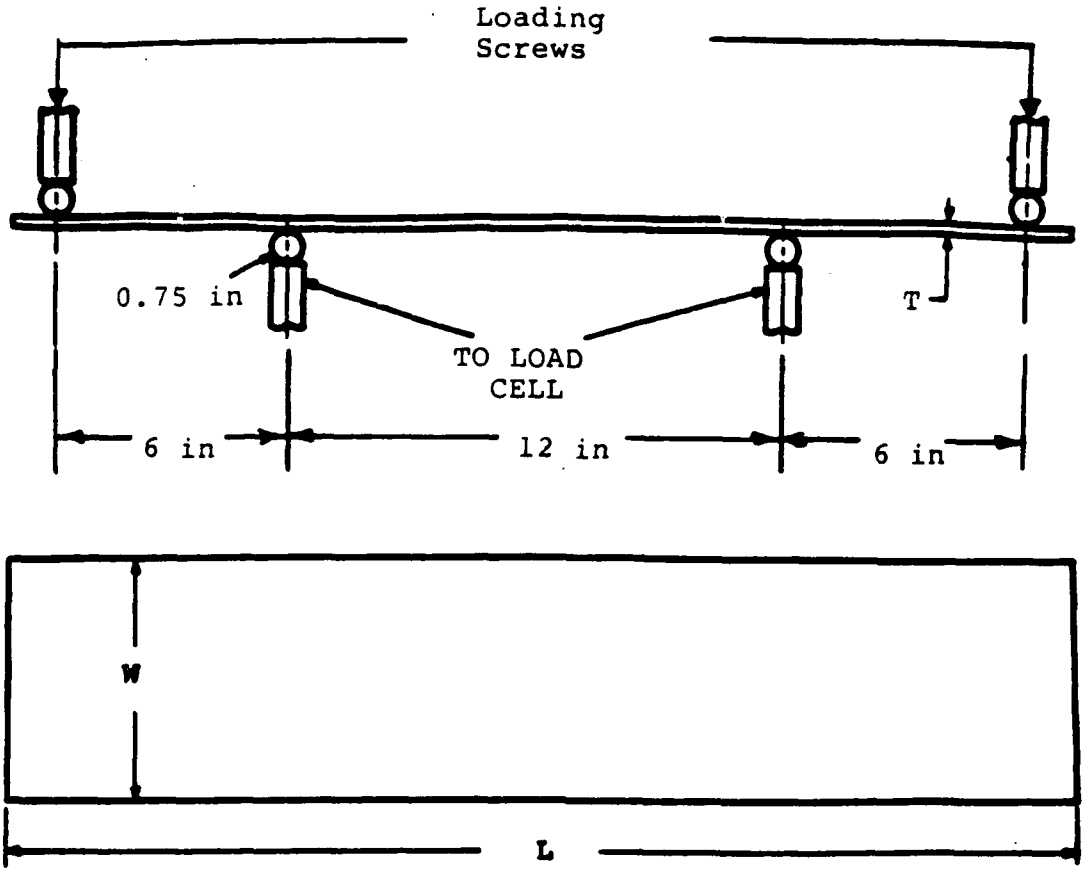

Figure 13. Four-Point Bending Specimen.

TABLE 2

FOUR-POINT BENDING SPECIMEN DIMENSIONS

Specimen Designation	Material	Geometry		
		Length-L	Width-W	Thickness-T
A	Polycarbonate	26.00 in	3.5 in	0.82 in
B	Polycarbonate	26.00 in	6.00 in	0.46 in

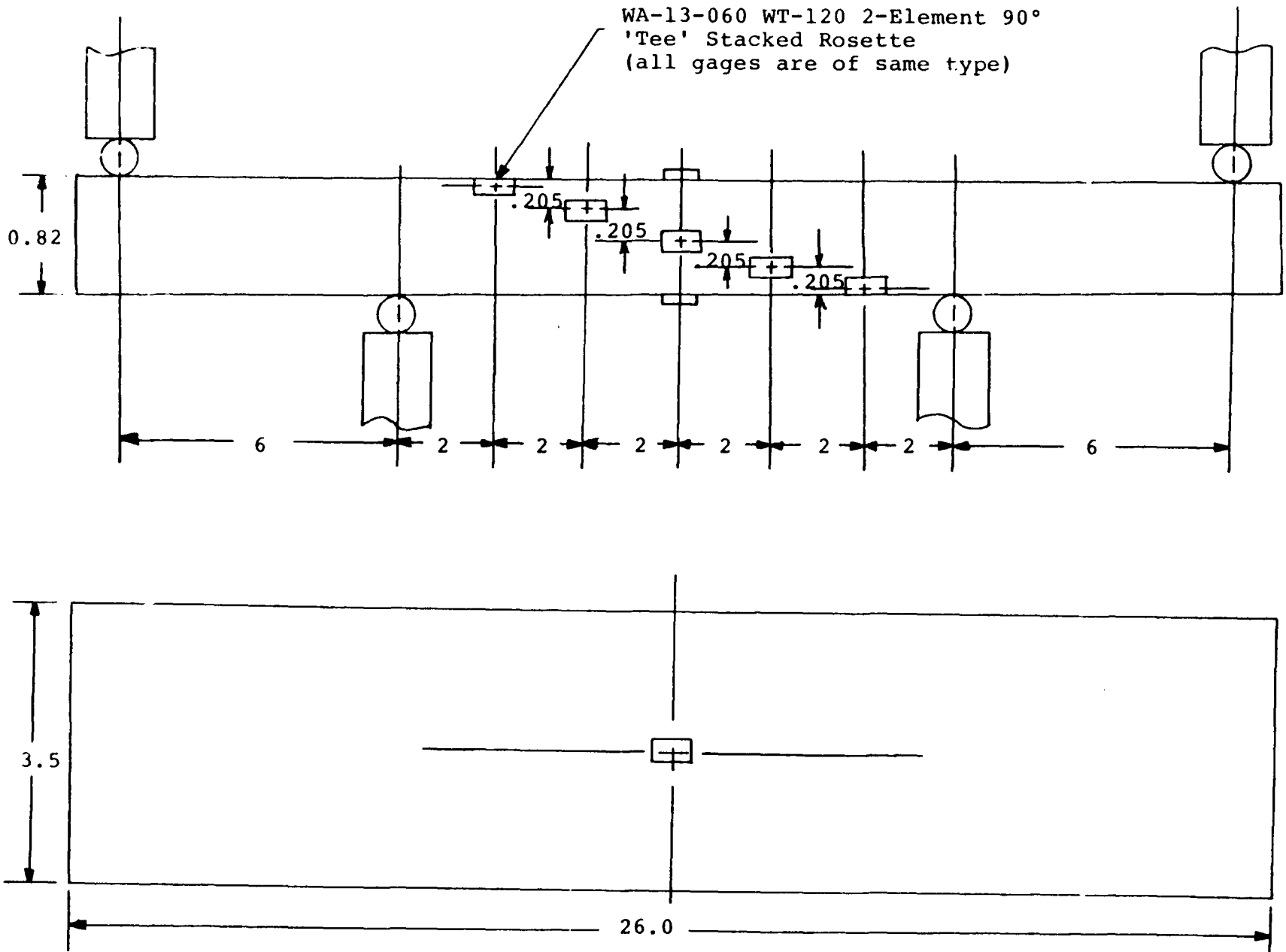

Figure 14. Strain Gage Stations on Four-Point Bending Specimen.

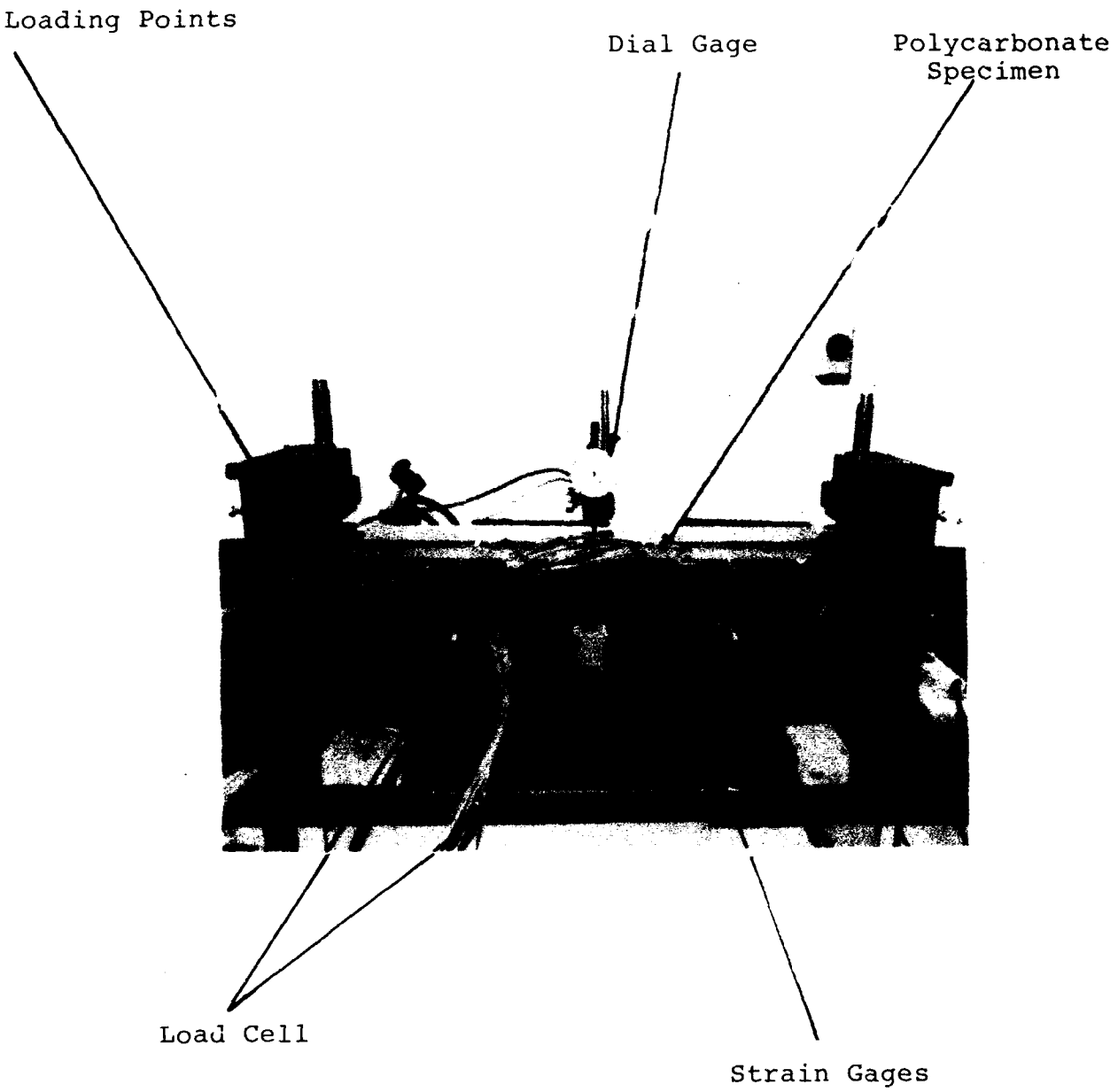

Figure 15. Four-Point Bending Specimen with Strain Gages.

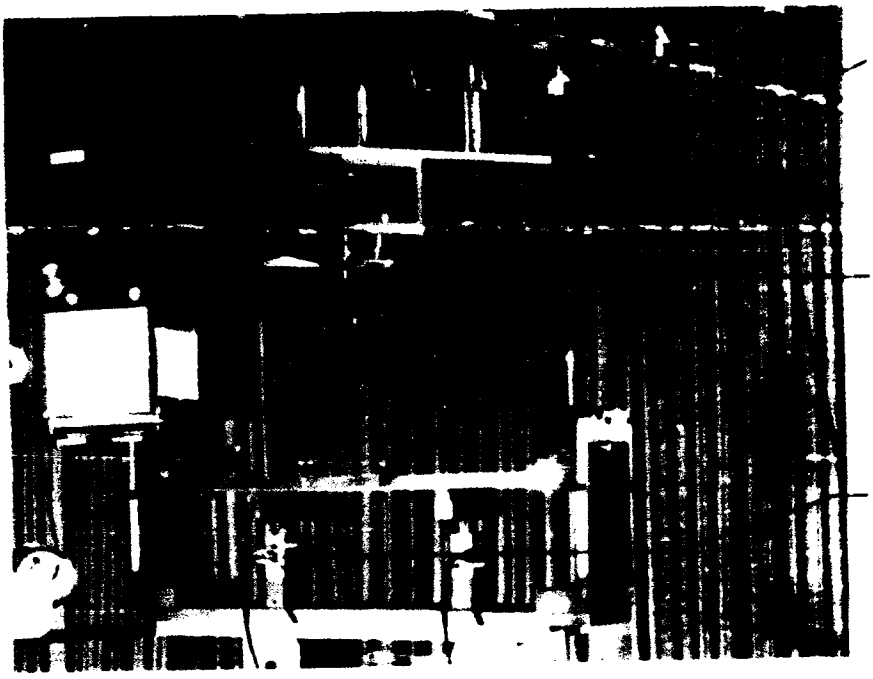

(a) Light Directed Vertically

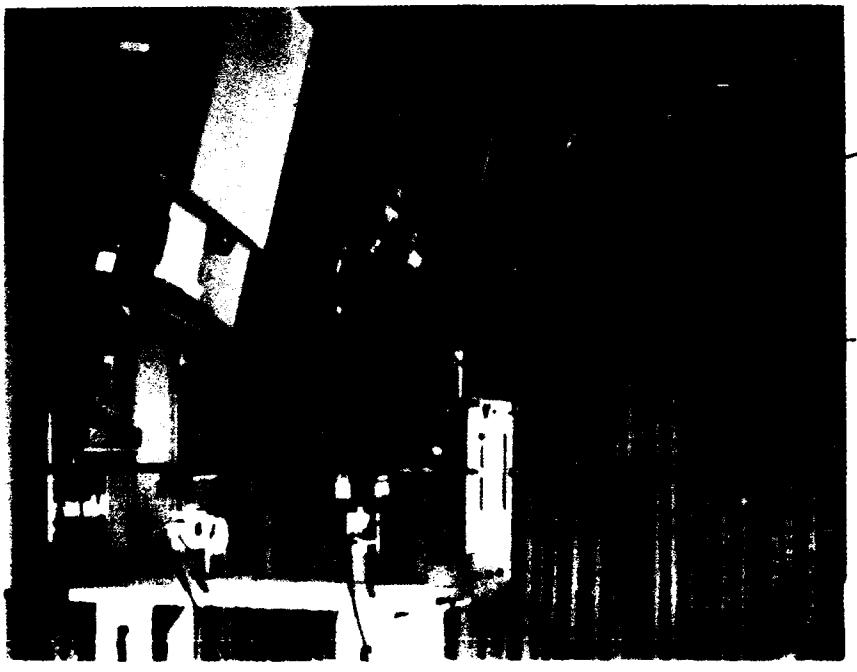

(b) Light Directed at 15° to Vertical

Figure 16. Four-Point Bending Apparatus.

balanced on a 20-channel bridge balance and were read using a microprocessor and printer of the Micromeasurement Strain Data Handling Sytem 4000. A dial indicator gage whose sensitivity was 0.001 inch was used to measure the deflections at the center of the specimen.

3.4 MATRIX FOR FOUR-POINT BENDING EXPERIMENTS

The experimental effort conducted is summarized in Table 3.

3.5 EXPERIMENTAL PROCEDURE

3.5.1 Scattered-Light Photoelastic Tests

The basic data measured in the scattered-light experiments were:

- o The direction θ of the secondary principal stresses
- o The difference of secondary principal stresses, (p-q)

The direction θ was established visually. With the direction of polarization of light and analyzer crossed (β=90°), the loaded model was rotated until the light intensity became zero (and the ribbon darkened completely). Then the secondary principal stresses and the X-Y direction coincided. This determined the direction of one of the secondary principal stresses. The loaded model was then rotated until maximum light intensity was observed. Maximum contrast of the photoelastic fringes was seen when the secondary principal stress was at 45° with the X-Y axes (Figure 17). The bright and dark fringes would be parallel to the top and bottom edges of the plate at Section GG (Figure 17(b)). However, these fringes were seen through the edge CD, Figure 17(a), and hence the actual magnification of the

TABLE 3

MATRIX OF SCATTERED-LIGHT PHOTOELASTIC AND STRAIN GAGE TESTS ON POLYCARBONATE FOUR-POINT BENDING SPECIMENS

Specimen	Direction of Light	Load (lbs)				
		30	50	75	100	125
A	Vertical		1	1	1	1
	15° to Vertical			1		
B†	Vertical	1				
	15° to Vertical	1				

† Strain gage tests were not conducted on Specimen B.

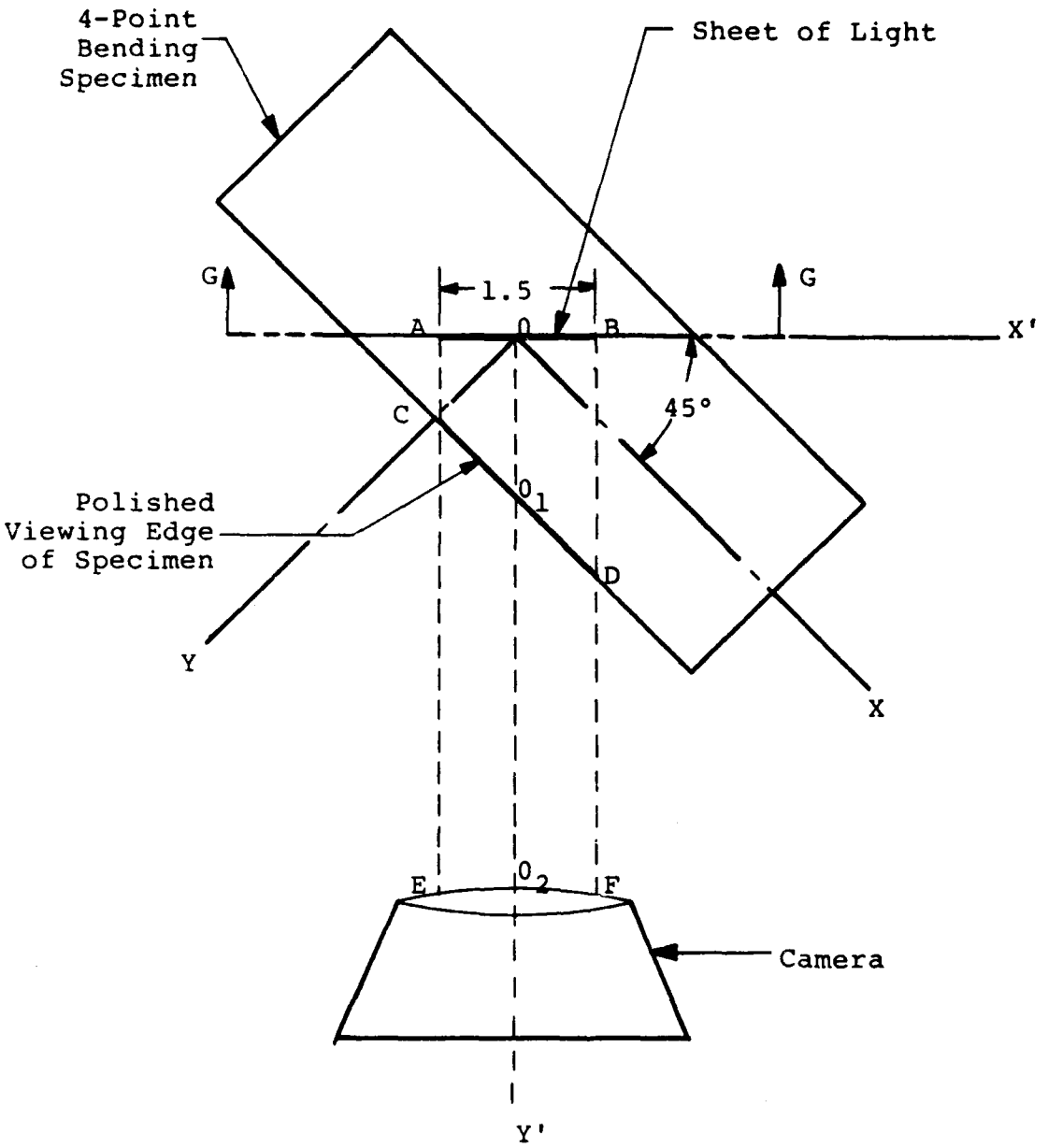

Figure 17. Schematic View of Four-Point Bending Specimen Illustrating the Propagation of Light and Film Magnification of the Scattered-light Photoelastic Fringes.

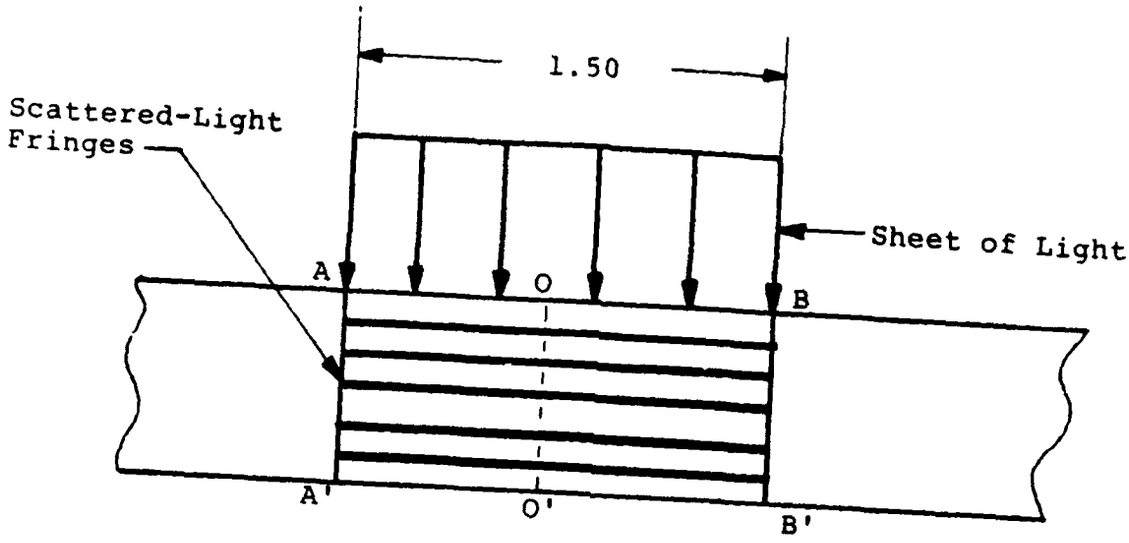

(b) Section on G G

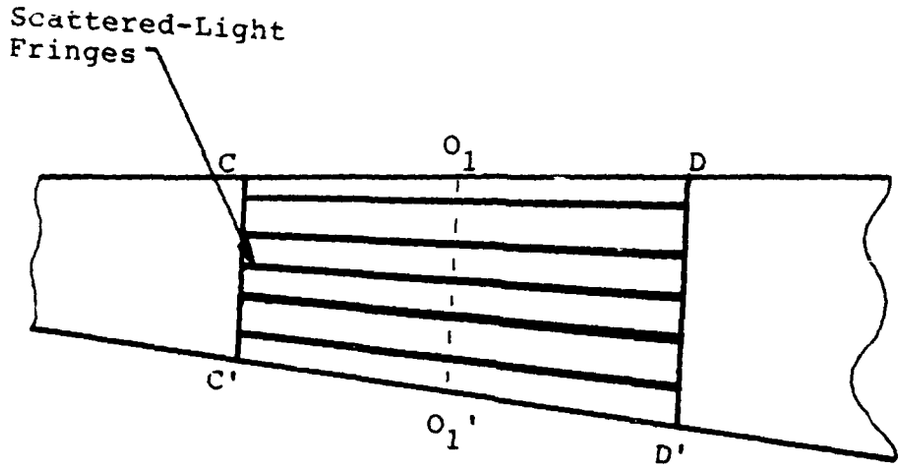

(c) Effect of Film Magnification on the Fringe Pattern

Figure 17 (continued)

fringes formed on photographic film was as shown in Figure 17(c). Fringes formed near the line DD′ had greater magnification than the fringes formed near the line CC′. This was because the point D was nearer to the camera lens than the point C (CE>DF). The film magnification factor for reducing the test data for locating the fringe positions along the thickness direction of the specimen was arrived at by equating the distance $O_1O'_1$, CC′ or DD′ to the actual thickness of the four-point bending specimen, and measuring the fringe positions using these scale factors at any one of these sections.

The film magnification was also obtained by another method which consisted of placing a scale with two lines ruled at 0.5 in. distance apart at the position AB (Figure 17(a)) and photographing these ruled lines from the same distance as that used for photographing the fringes. The film magnification factor determined by this method was slightly different as the camera focusing for the fringes would be different from the focusing needed for the ruled scale. The difference in magnification factors between these two methods was due to the small changes in the magnification of the image whenever focusing of the object changed. For evaluating experimental results, the film magnification obtained directly from the fringe photographs was used.

The scattered-light photoelastic fringe patterns were photographed corresponding to the two positions of the directions of light. In position 1, light was directed vertically (Figures 9 and 16(a)), and in position 2, light was directed at angle 15° to the vertical (Figures 10 and 16(b)).

The scattered-light photoelastic fringe patterns were photographed using two different cameras. The first camera was a part of the data acquisition system. The camera had a 150mm lens with f=5.6. The camera lens was 18 inches from the

sheet of light entering the four point bending specimen. Three types of film were used to photograph the fringes:

- o Photographic Film 1, Polaroid 4 inches x 5 inches Land film, type 57/high speed, ASA 3000. Good photographs of the fringe patterns were obtained with f=64 and an exposure time of 5 minutes.
- o Photographic Film 2, Polaroid 4 inches x 5 inches Land film, Type 52, ASA 400. Good photographs of the fringe patterns were obtained with f=64 and an exposure time of 15 minutes.
- o Photographic Film 3, Polaroid 4 inches x 5 inches Land film, Type 51/high contrast, ASA 125. The light provided by the laser was insufficient to obtain any photographs of the fringe patterns.

Enlargements (4 inches x 5 inches) of the area of fringe patterns were obtained by copying the Polaroid photographs of the fringe patterns by a camera equipped with a macrolens. The copied film was processed by three separate procedures: (1) Acufine method, increased the speed to ASA 250 but normal time (8 minutes was used to develop the film); (2) D-76 double solution doubled the processing time to increase the contrast; and (3) standard method, used the normal processing time of 8 minutes and normal speed.

The second camera used for photographing the scattered-light photoelastic fringes was a Nikon 2020 with a 50mm, f=1.8 lens. A closeup lens (Number 4) was used to photograph the fringes from a distance of 8 inches from the sheet of light entering the four-point bending specimen. This procedure enabled the camera to focus on the region of the fringe pattern only.

Two types of 35mm roll film were evaluated: (1) Kodak Tri-X pan roll film for black and white prints, ASA 400, with typical exposure time of one minute for f=22; and (2) Kodak Plus-X pan roll film for black and white prints, ASA 125, with typical exposure time of 3 minutes for f=22.

Better clarity and contrast were obtained with the Nikkon 2020 and Kodak Plus-X film and hence this combination was used to photograph the fringe patterns of the four-point bending specimen. The camera was supported on a tripod stand with an extension arm.

3.5.2 Strain Gage Tests

The strain gages were zeroed without any load. A preload of 10.85 pounds was applied to firmly position the specimen against the supports. The initial strain gage readings were recorded. Loads of 60.85 pounds, 85.85 pounds, 110.85 pounds and 135.88 pounds were applied to the specimen and strains were recorded at each load. The strains at each load were obtained as the difference between the strain gage reading at that load and the preload. The stresses in the beam were computed from these strains, using the modulus determined from the rosette gage WA-13-060WT-120 (Appendix).

A dial gage was positioned to measure the deflection at the center of specimen. The initial reading of the dial gage was recorded at the preload. The dial gage readings were also recorded at the same loads as were applied for strain measurement. The deflection at each load was obtained as the difference between the dial gage reading at that load and the preload. These deflections were used to compute the Young's modulus for the four-point bending specimen material (Appendix).

3.6 EXPERIMENTAL RESULTS

The scattered-light photoelastic fringes, the curves of birefringence, and a comparison of the secondary principal stresses in the four-point bending specimens A and B are presented in the following paragraphs.

3.6.1 Scattered-Light Photoelastic Fringe Patterns

The scattered-light photoelastic fringe patterns are presented in Figure 18 for Specimen A, which was subjected to a load of 50 pounds. Figure 18(a) shows the fringe patterns when the compensator was not used. Figures 18(b), (c), and (d) show the fringe patterns when 1/4, 1/2, and 3/4 wavelength retardation was introduced by the compensator with its axis aligned parallel to the direction of the known maximum secondary principal stress axis. The fringe order was increased uniformly by the amount of retardation introduced and the fringes moved down. In short, this defines a method of determining the direction of maximum secondary principal stress, as discussed in Section 2.

Figures 19(a) and (b) present the scattered-light fringe patterns in Specimen A when the specimen was subjected to a load of 75 pounds and the light directed vertically and at an angle of 15° to the vertical, respectively. Figures 20(a) and (b) present the fringe patterns in Specimen A subjected to loads of 100 and 125 pounds, respectively. Figures 21(a) through (g) present the fringe patterns in Specimen B without the compensator and for various values of retardation introduced by the compensator aligned along the directions of maximum and minimum secondary principal stress axes.

3.6.2 Curves of Birefringence

Figures 22 through 26 show typical curves of birefringence for Specimen A subjected to various loads. A computer program was used to fit the experimental points by

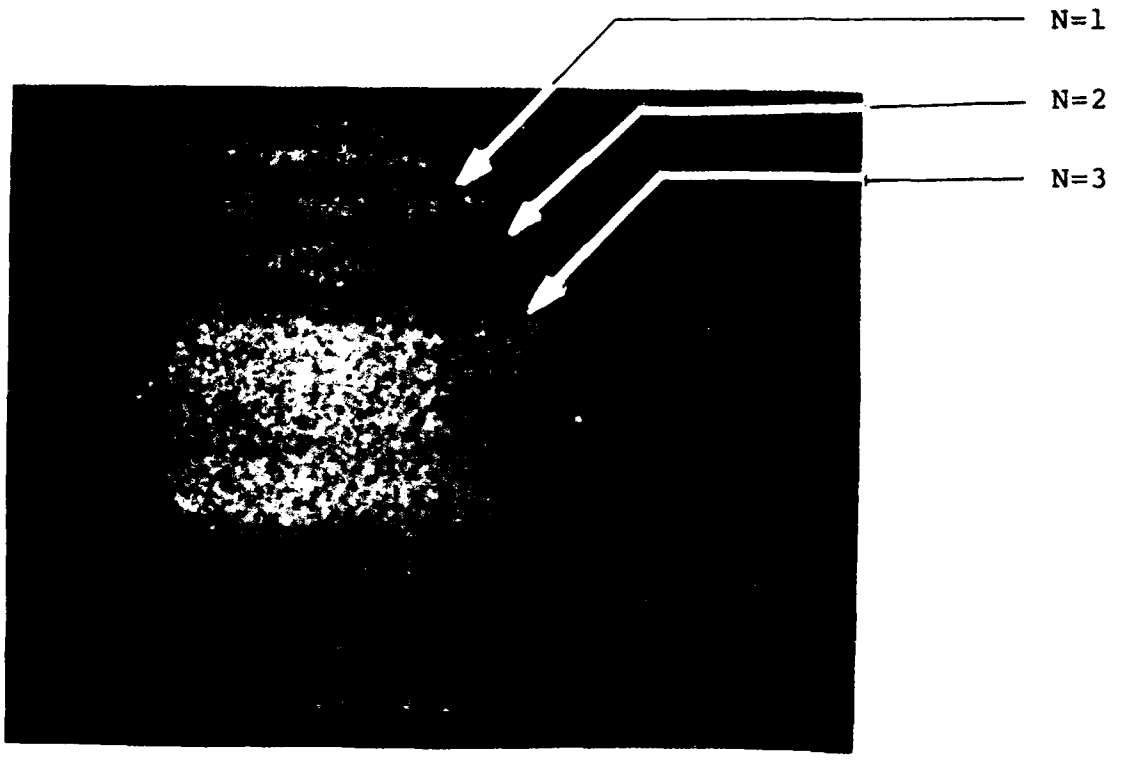

(a) No Compensator

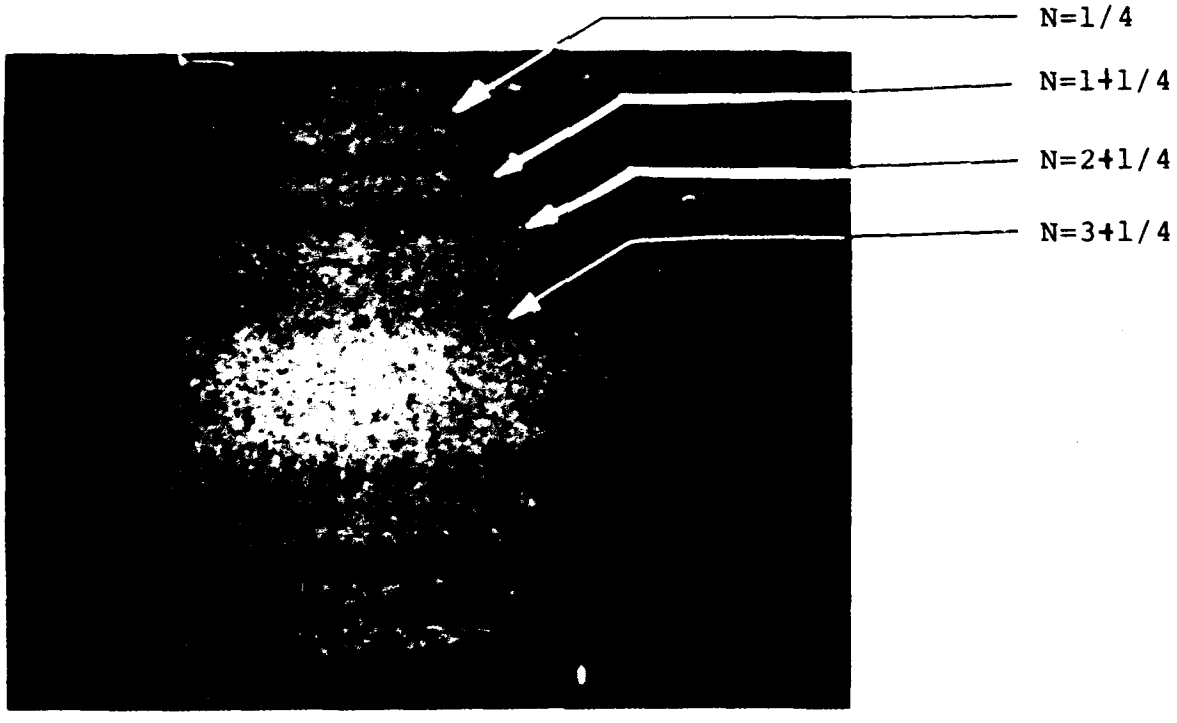

(b) Compensator Axis Parallel to Maxm. Secondary Principal Axis
Retardation: N=1/4

Figure 18. Scattered-Light Fringes from a Sheet of Light Passing Through the Specimen A, (Load=50 lbs)

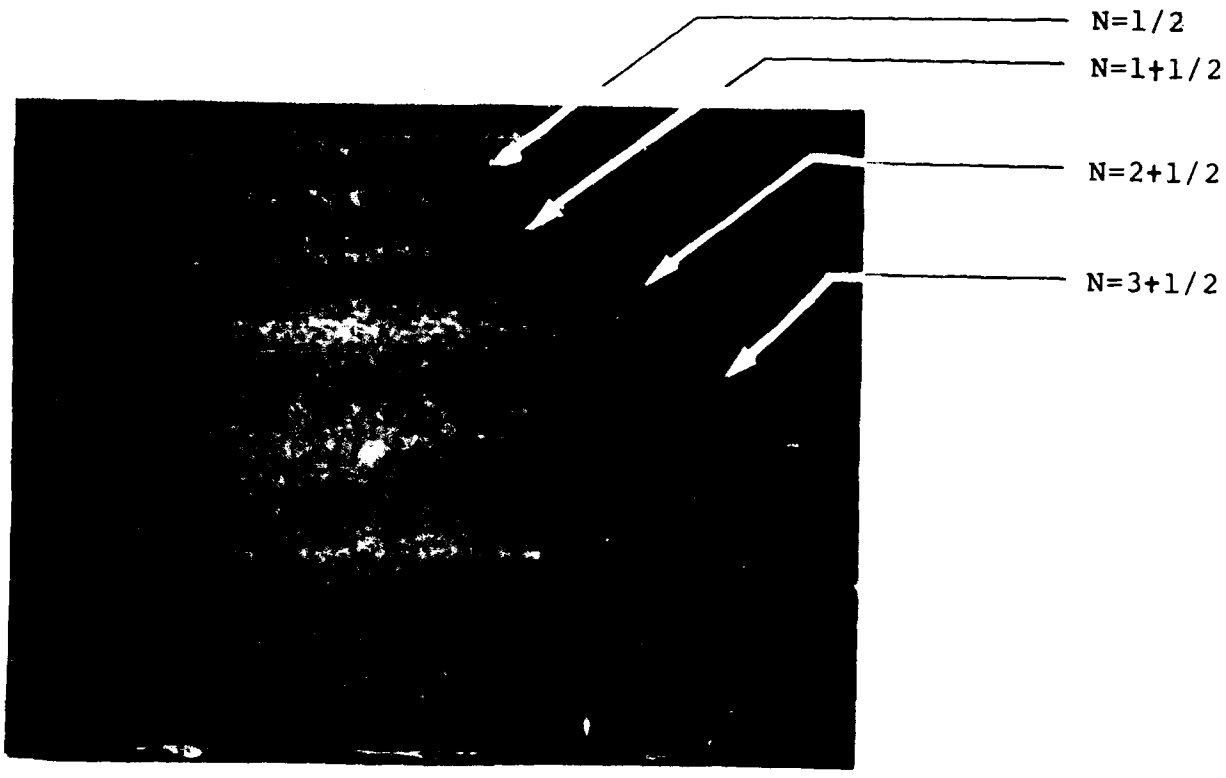

(c) Compensator Axis Parallel to Maxm. Secondary Principal Axis
Retardation: N=1/2

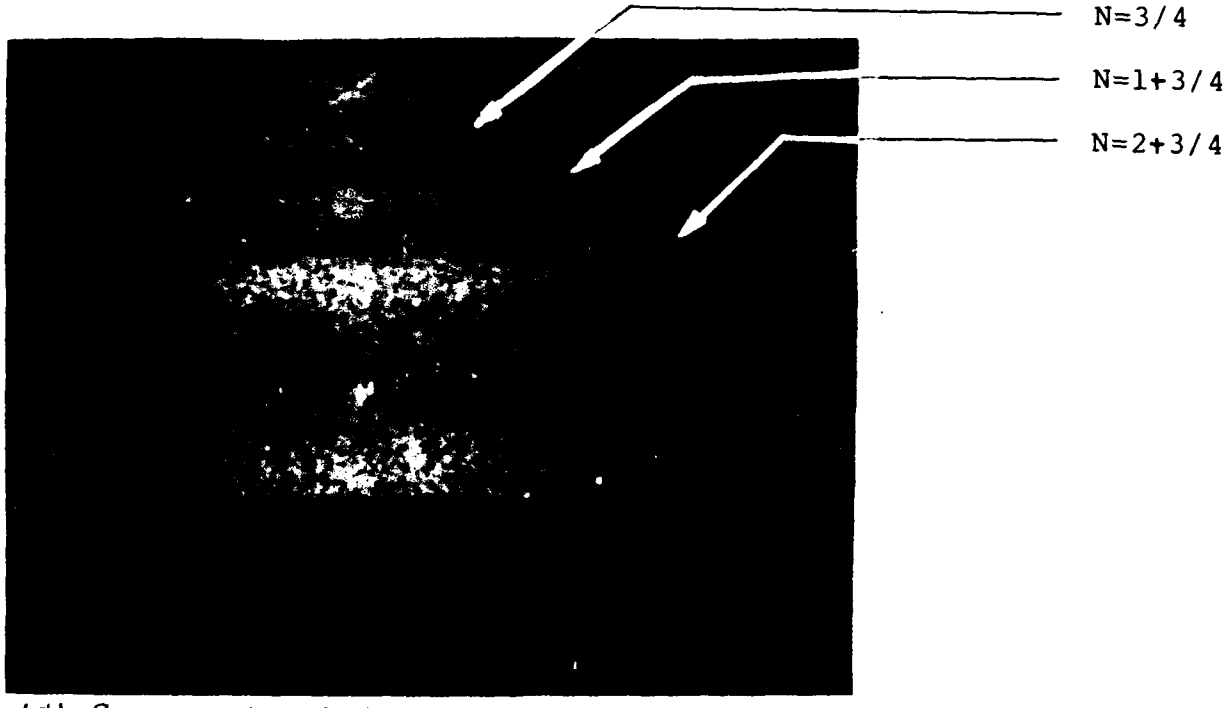

(d) Compensator Axis Parallel to Maxm. Secondary Principal Axis
Retardation: N=3/4

Figure 18 (continued)

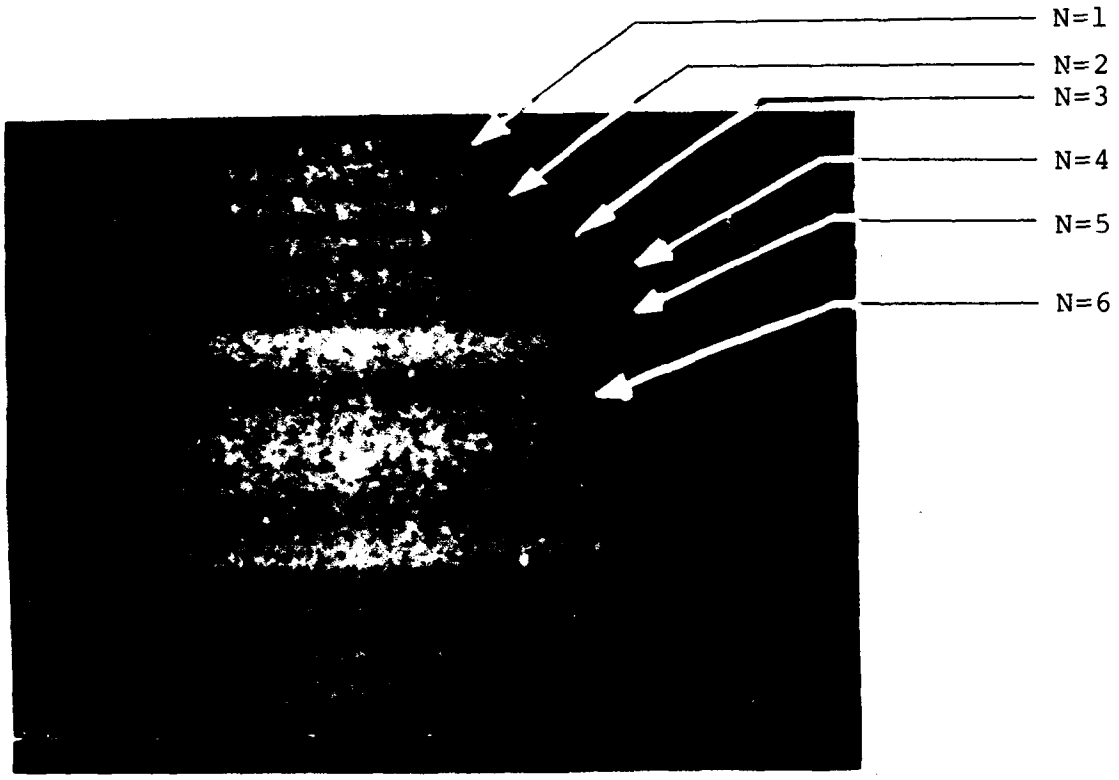

(a) Light Directed Vertically

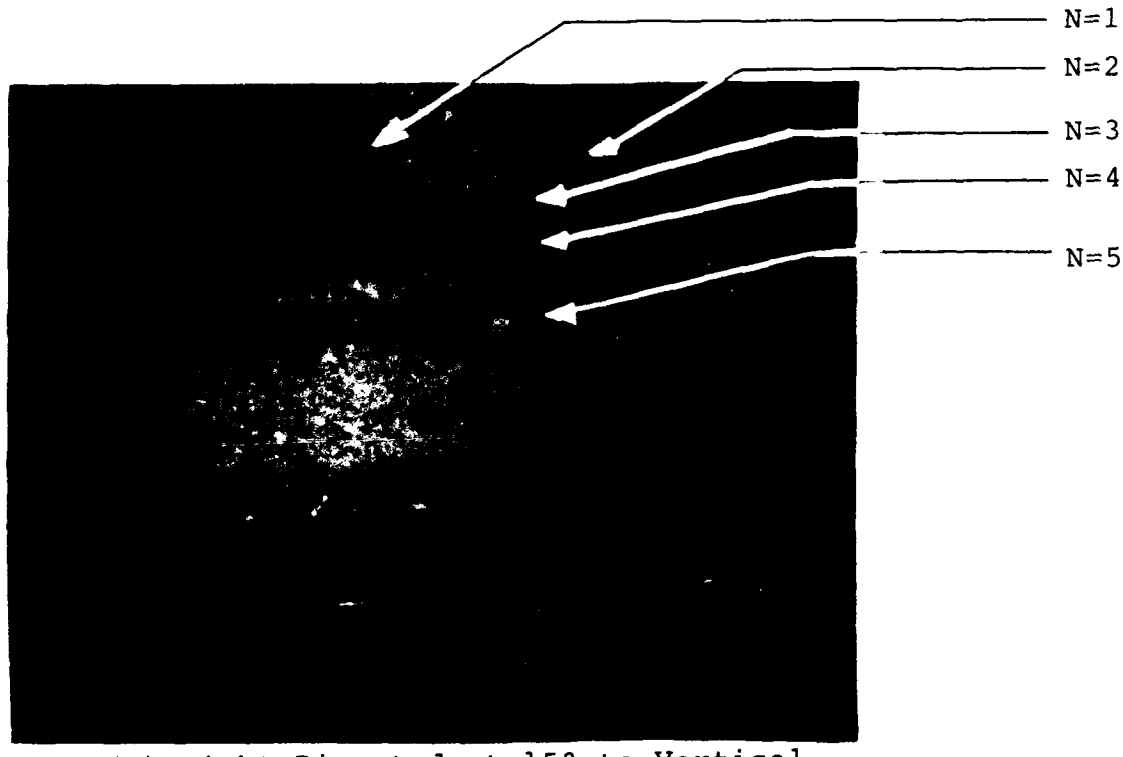

(b) Light Directed at 15° to Vertical

Figure 19. Scattered-Light Fringes from a Sheet of Light Passing Through the Specimen A (Load = 75 lbs)

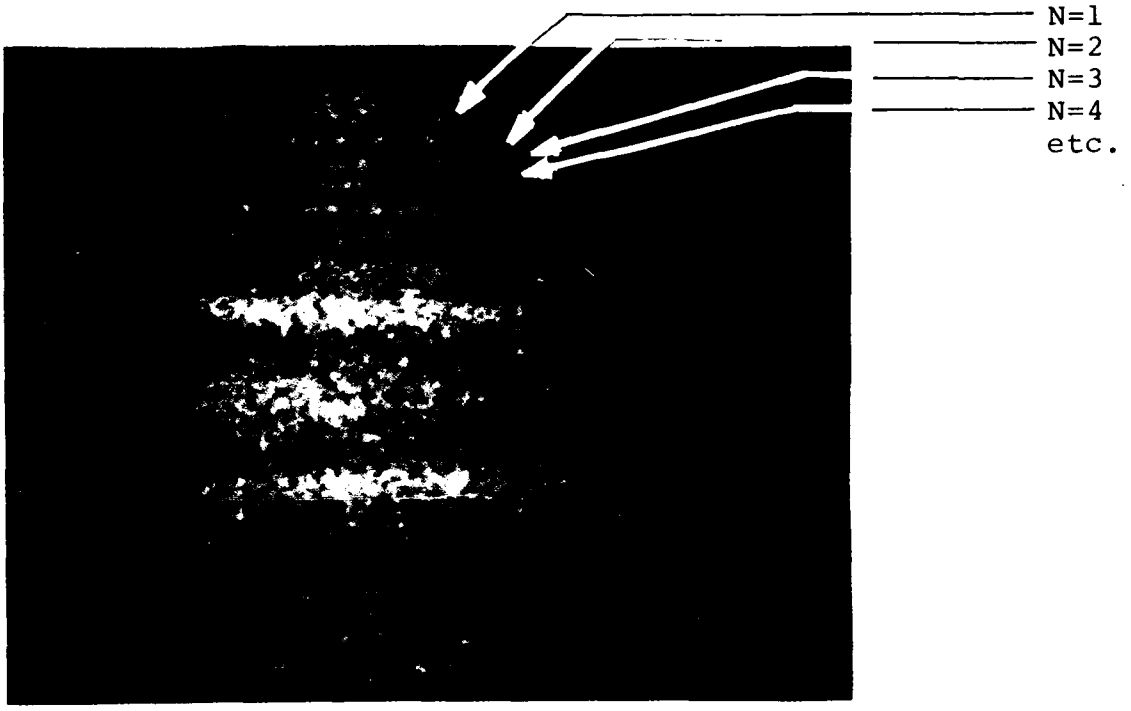

(a) Load = 100 lbs

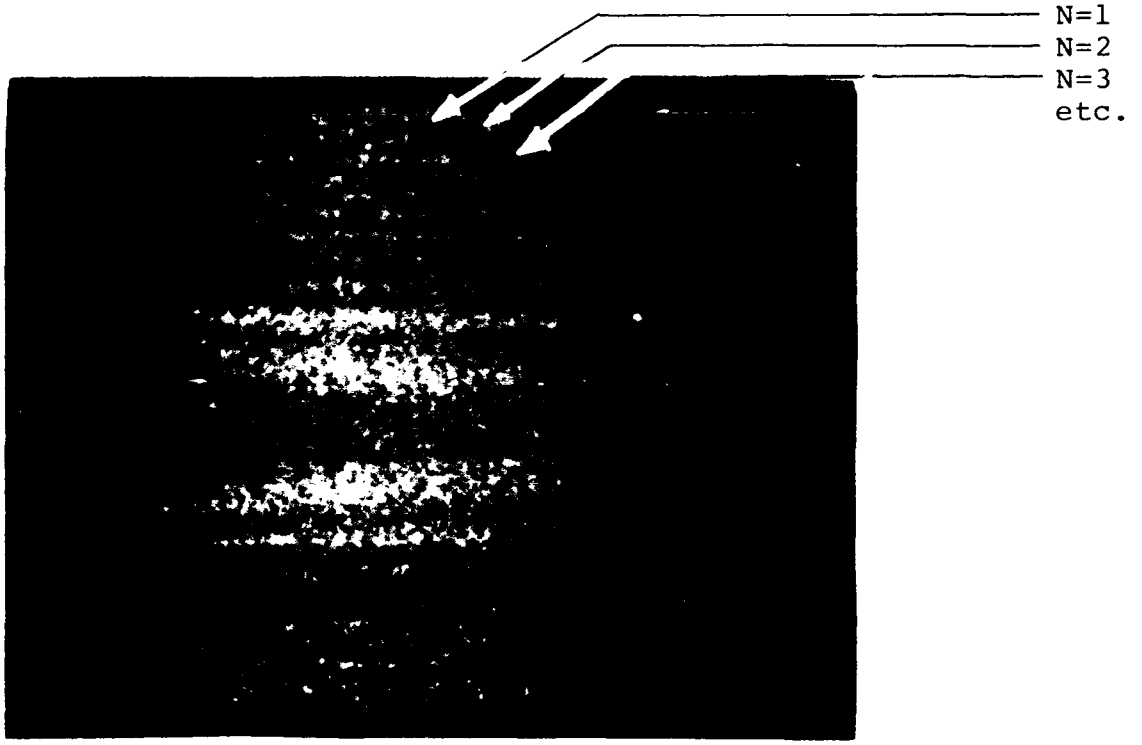

(b) Load = 125 lbs

Figure 20. Scattered-Light Fringes from a Sheet of Light Passing Through the Specimen A.

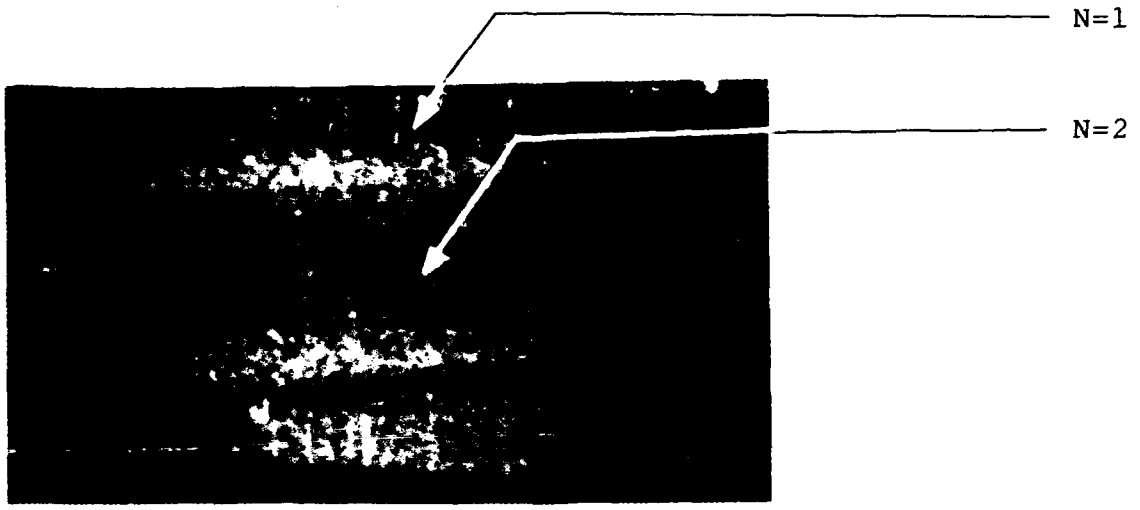

(a) No Compensator

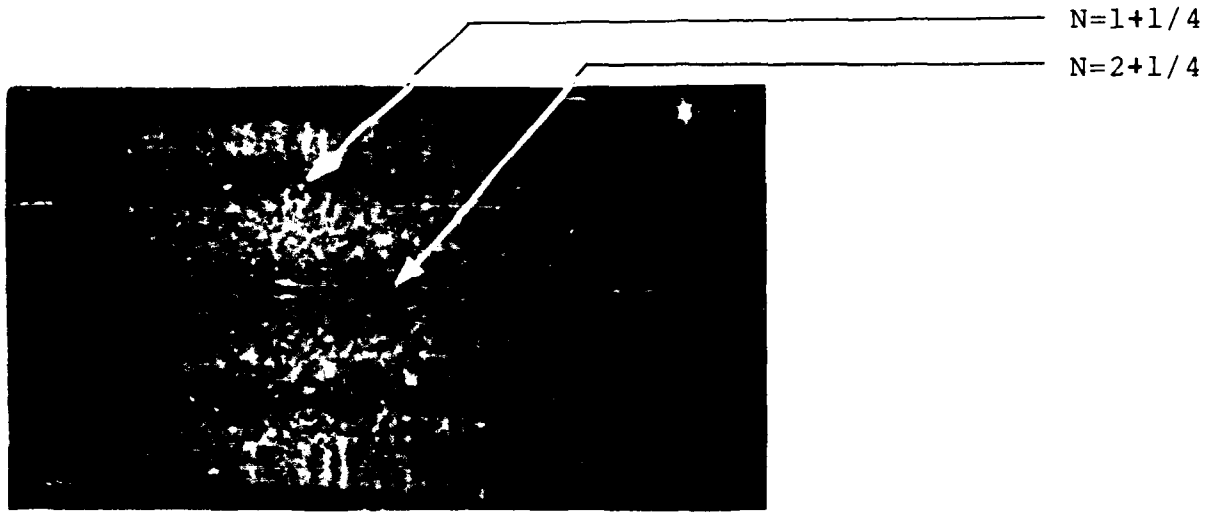

(b) Compensator Axis Parallel to Maxm. Secondary Principal Axis Retardation: N=1/4

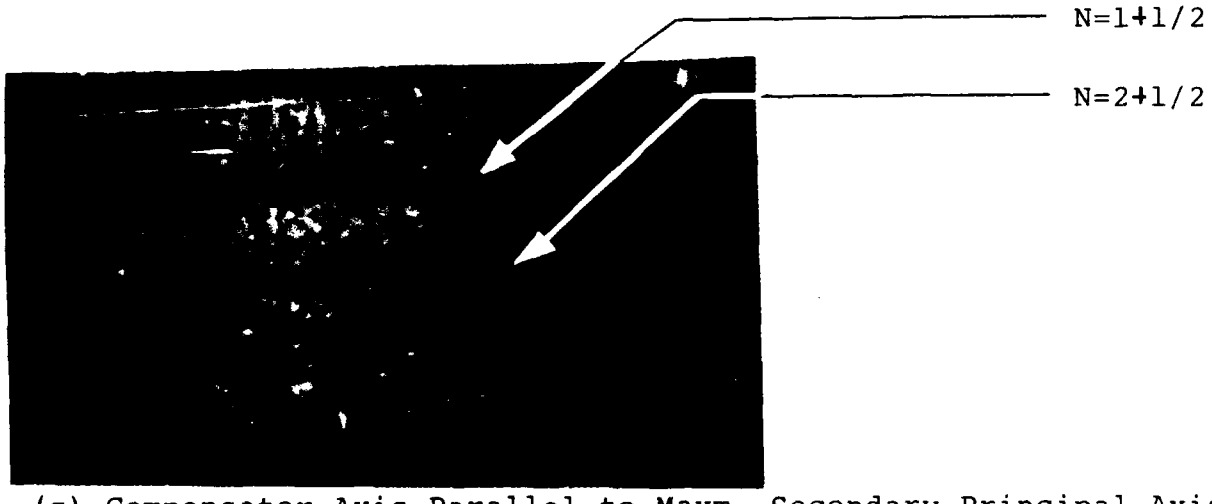

(c) Compensator Axis Parallel to Maxm. Secondary Principal Axis Retardation: N=1/2

Figure 21. Scattered-Light Fringes from a Sheet of Light Passing Through the Specimen B (Load = 30 lbs)

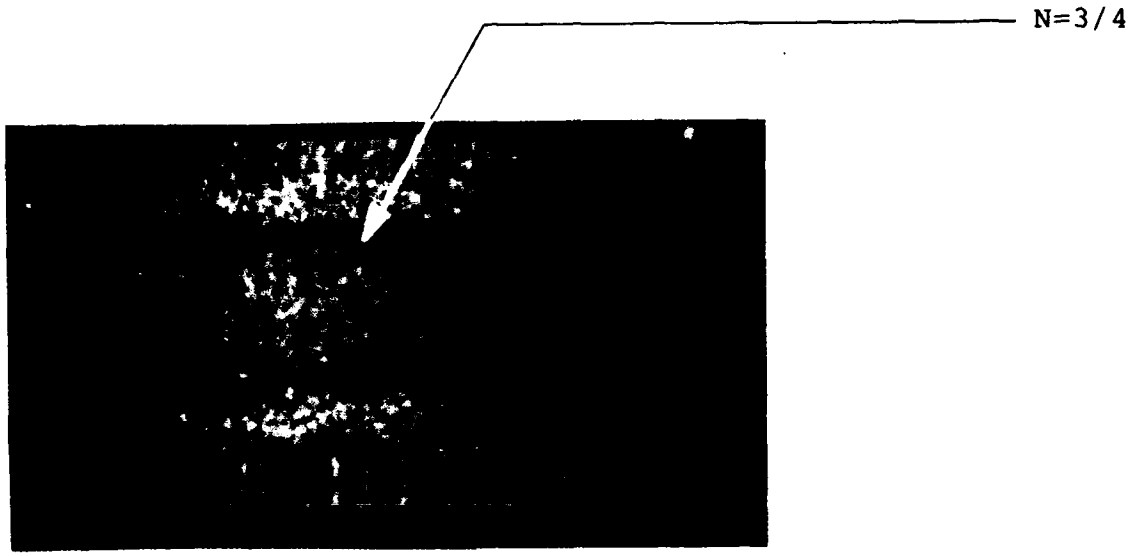

(d) Compensator Axis Parallel to Maxm. Secondary Principal Axis
Retardation: N=3/4

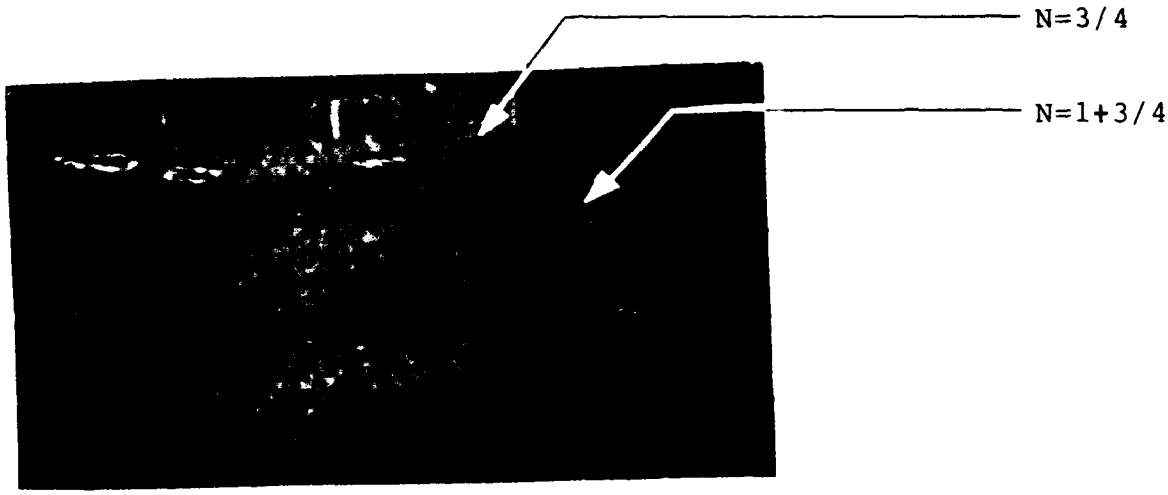

(e) Compensator Axis Parallel to Minimum Secondary Principal Axis
Retardation: N=1/4

Figure 21 (continued)

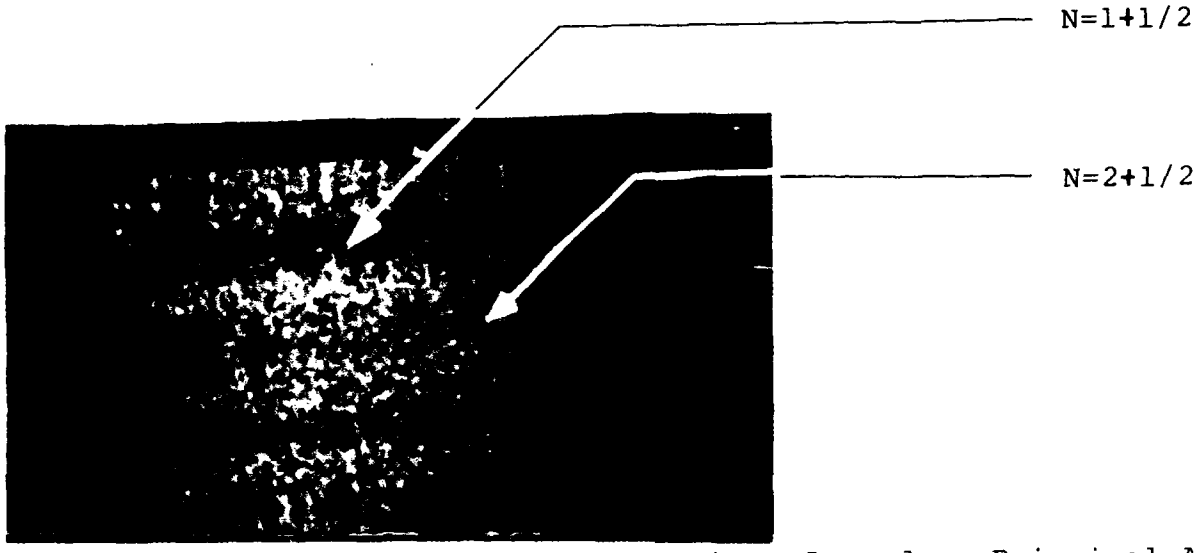

(f) Compensator Axis Parallel to Minimum Secondary Principal Axis
Retardation: N=1/2

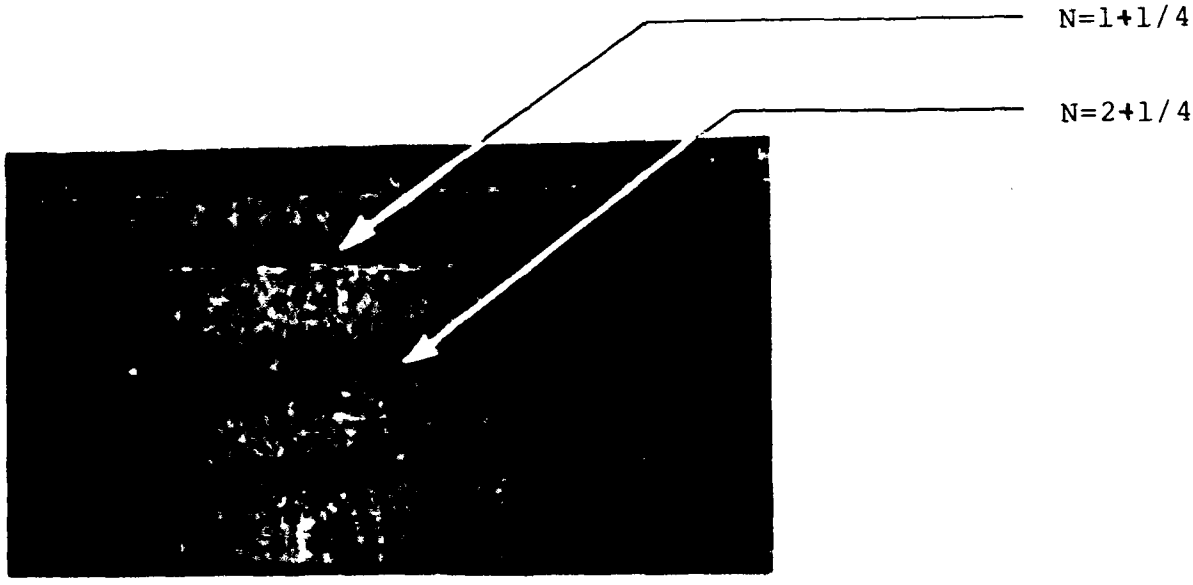

(g) Compensator Axis Parallel to Minimum Secondary Principal Axis
Retardation: N=3/4

Figure 21 (continued)

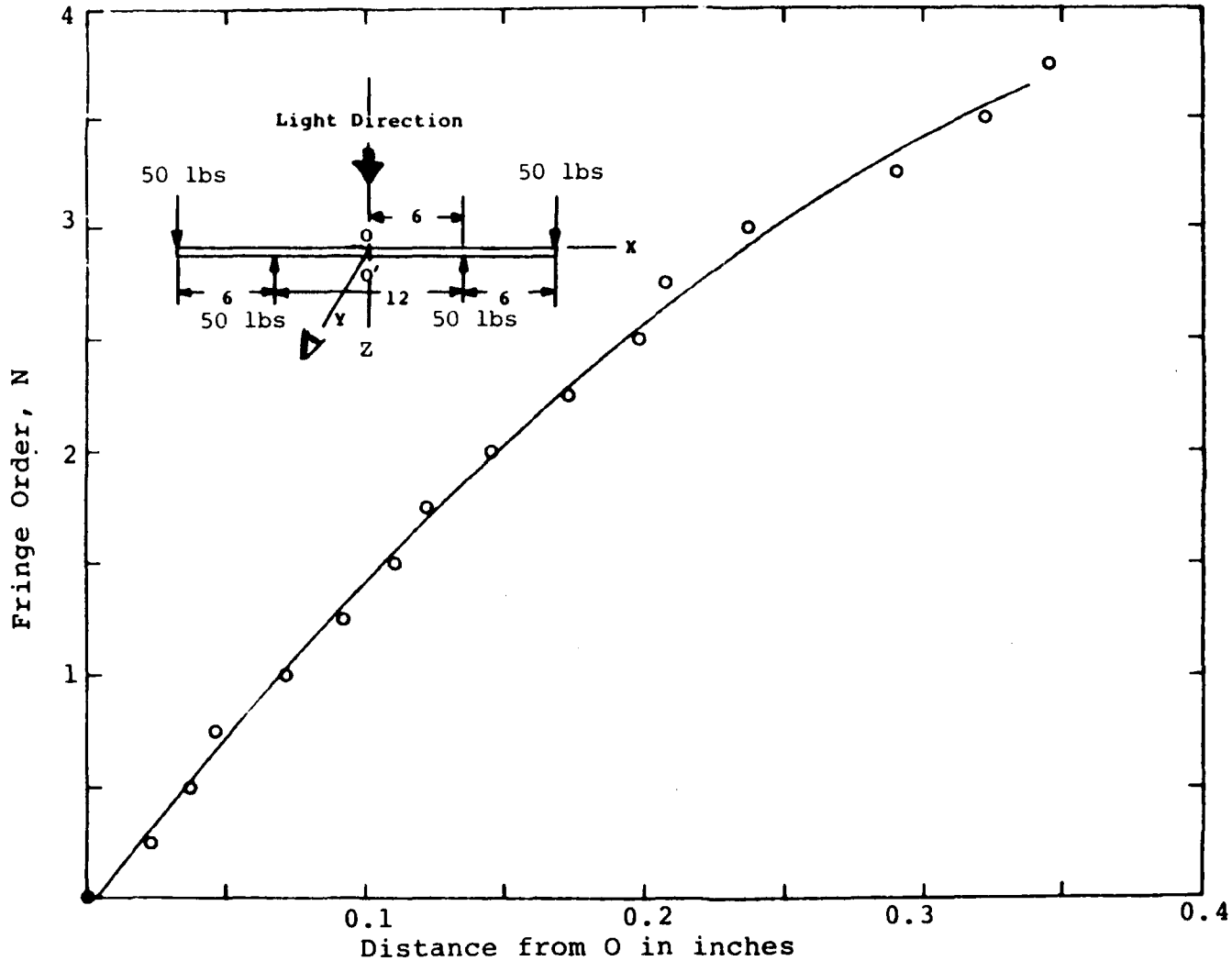

Figure 22. Second-order Polynomial Curve of Birefringence Along OO' for Specimen A, Load 50 lbs.

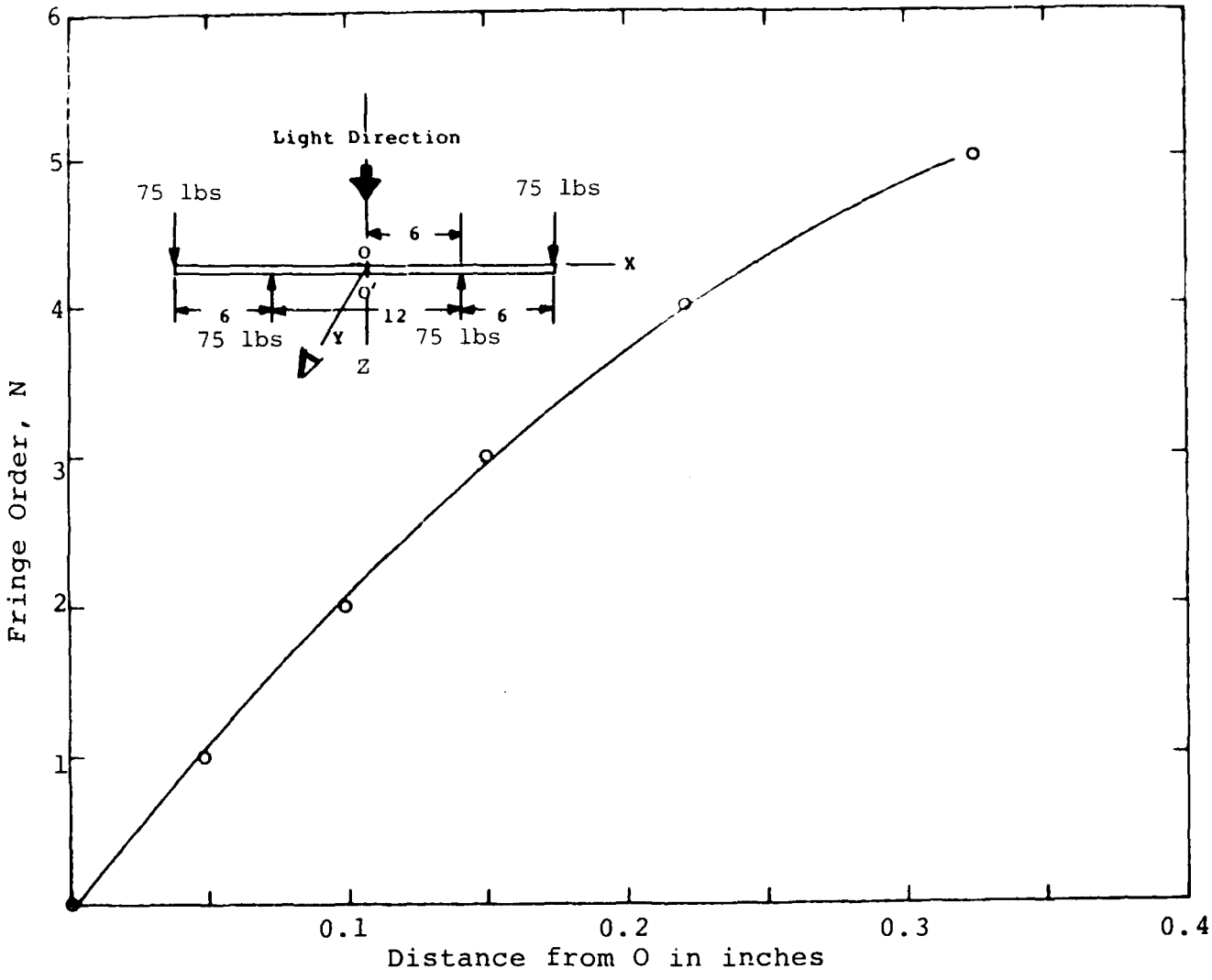

Figure 23. Second-order Polynomial Curve of Birefringence Along OO' for Specimen A, Load 75 lbs.

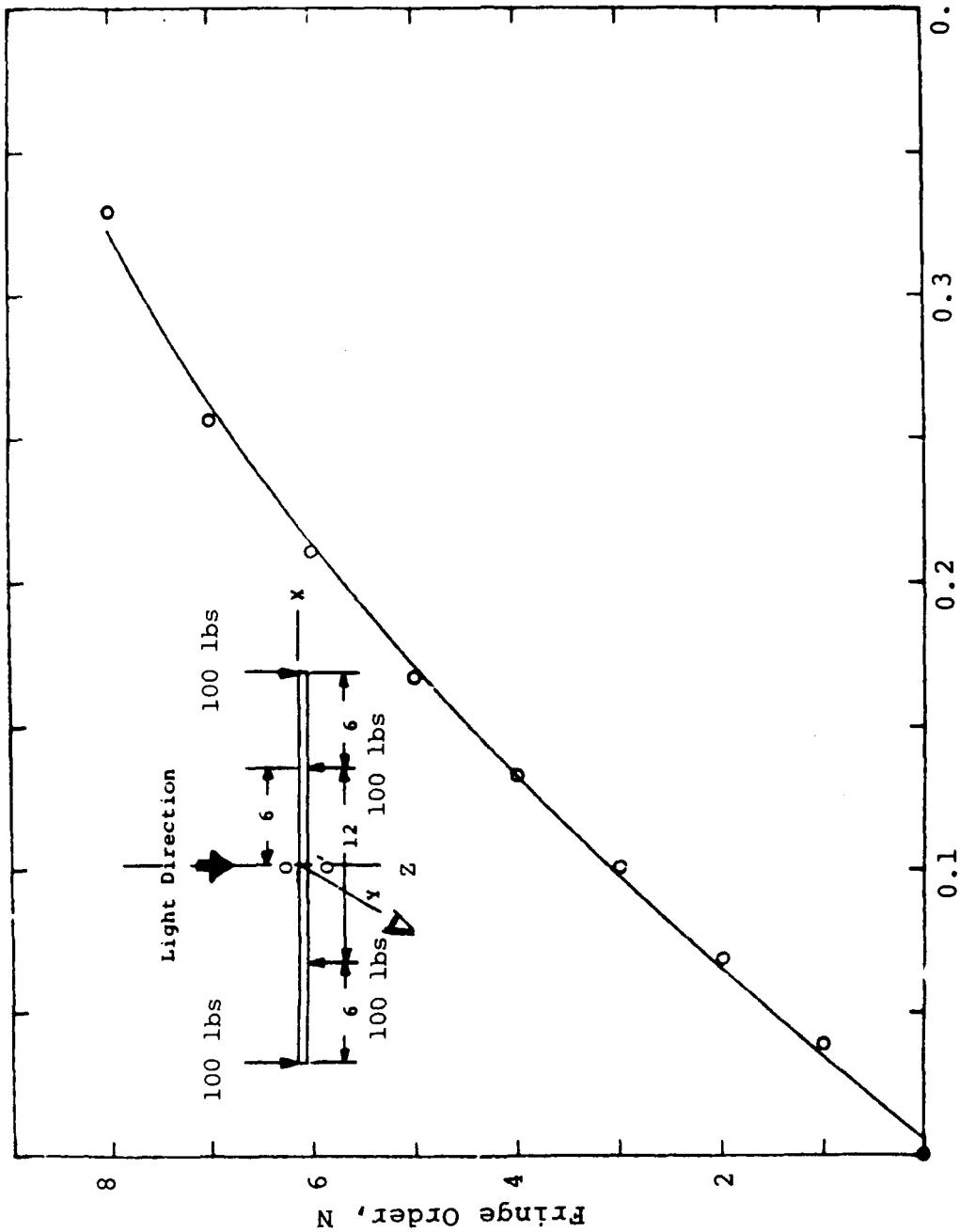

Figure 24. Second-order Polynomial Curve of Birefringence Along OO' for Specimen A, Load 100 lbs.

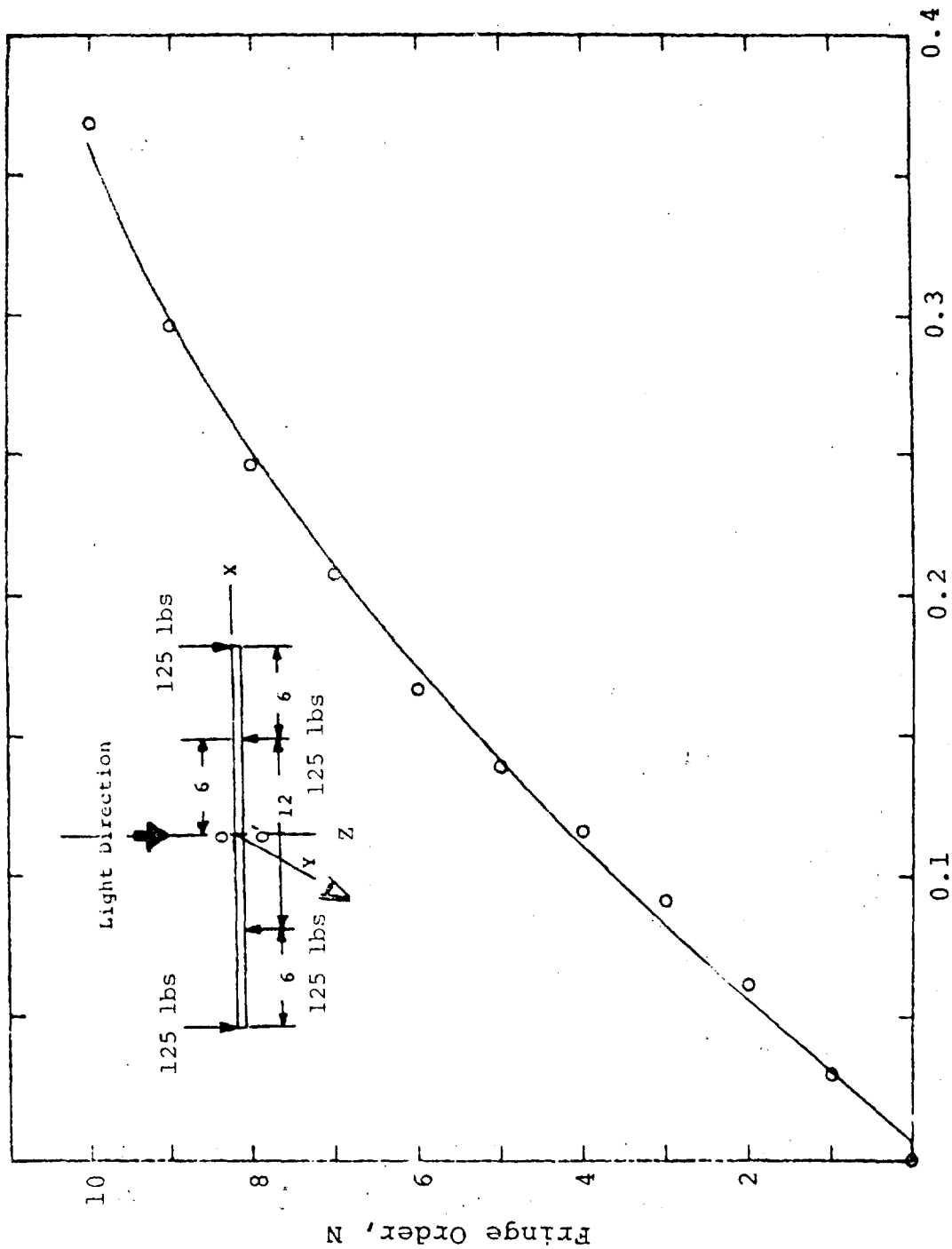

Figure 25. Second-order Polynomial Curve of Birefringence Along OO' for Specimen A, Load 125 lbs.

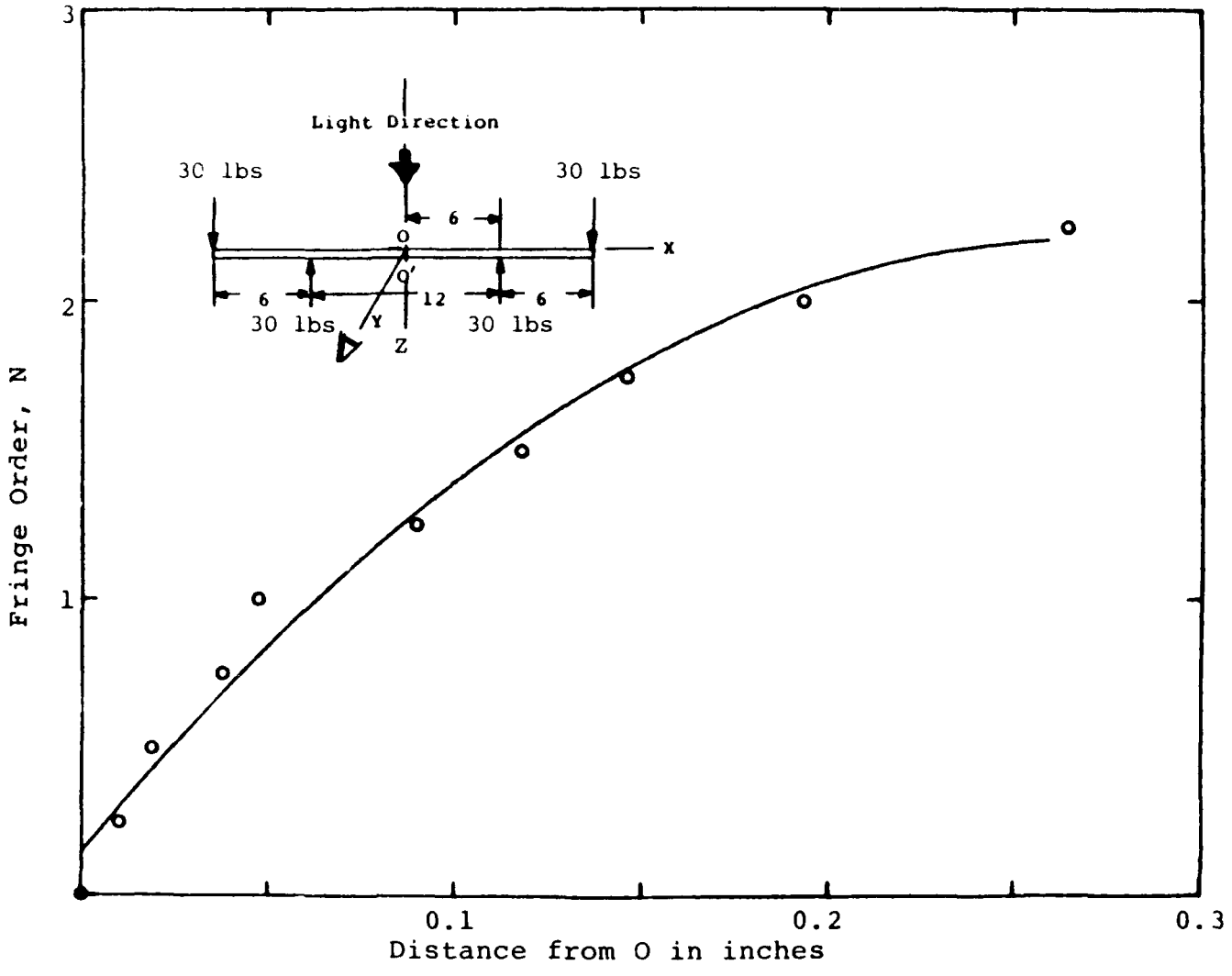

Figure 26. Second-order Polynomial Curve of Birefringence Along OO' for Specimen B , Load 30 lbs

curves of least square polynomials. The second-order polynomial was found to give the best fit for all the cases. Both the experimental points and fitted curves were drawn for each load case and each specimen in Figures 22 through 26. The coefficients of the second-order polynomial and the standard deviations are presented in Table 4.

3.6.3 Secondary Principal Stresses

The secondary principal stresses were computed from the fringe data by two methods:

Method 1. In this method, the minimum secondary principal stress q was assumed to be zero. The maximum secondary principal stress p was obtained from the stress optic law of Equation 15.

Method 2. The secondary principal stresses p and q were computed from Equations 21 and 22 using dN/dZ and $d\tilde{N}/dZ'$ values computed from fringe photographs taken with the light directed vertical and at 15° to the vertical (Figures 18(a) and (b)). Tables 5 and 6 present experimental results from both these methods, the theoretical solutions obtained from simple beam theory, and the experimental solutions obtained from strain gages. The Appendix describes the experiments conducted to determine the elastic constants of the polycarbonate material.

3.7 DISCUSSION OF RESULTS

3.7.1 Scattered-Light Photoelastic Fringe Photographs

The fringe photographs obtained using the Nikon 2020 camera had high resolution and contrast when compared with earlier fringe photographs obtained using the camera supplied by Measurements Group Inc. The Nikon camera photographs made it possible to determine the fringe positions more accurately. When the fringe density was lower (Figure 21) as in the case of

TABLE 4

COEFFICIENTS OF POLYNOMIAL USED TO CURVE-FIT DATA

$$N = A_o + A_1 Z + A_2 Z^2$$

Specimen	Load (lbs)	A_o	A_1	A_2	$S_{N/Z}$*
A	50	-0.5146E-01	0.1624E+02	-0.1565E+02	0.6484E-01
A	75	-0.4412E-01	0.2374E+02	-0.2512E+02	0.4754E-01
A	100	-0.2059	0.3613E+02	-0.3316E+02	0.1259
A	125	-0.2698	0.4303E+02	-0.4025E+02	0.1886
B	30	0.1799	0.1485E+02	-0.2706E+02	0.1069

$$S_{N/Z} = \left(\frac{\sum_{i=1}^{n} N_i^2 - A_o \sum_{i=1}^{n} N_i - A_1 \sum_{i=1}^{n} N_i Z_i}{n-4} \right)^{1/2}$$

where n = total number of points recorded on fringe photos.

*$S_{N/Z}$ = standard deviation which is a measure of the mean deviation of the experimental points from the fitted curve.

TABLE 5

COMPARISON OF P STRESS RESULTS DETERMINED BY SCATTERED-LIGHT PHOTOELASTICITY, STRAIN GAGES, AND SIMPLE BEAM THEORY FOR FOUR-POINT BENDING SPECIMENS
(q assumed to be zero)

Specimen	Load lbs	Z inches	Scattered-Light P, psi	Strain Gage P_S, psi	Beam Theory P_B, psi	Discrepancy % $\frac{P-P_S}{P_S} \times 100$	Discrepancy % $\frac{P-P_B}{P_B} \times 100$	Discrepancy % $\frac{P_S-P_B}{P_B} \times 100$
A	50	0	666	679	765	-2	-13	-11
	50	0.205	402	320	382	+31	+5	-16
	75	0	974	1025	1147	-5	-15	-11
	75	0.205	551	629	574	-12	-4	+10
	100	0	1481	1693	1530	-13	-3	+11
	100	0.205	923	1055	765	-13	+20	+40
	125	0	1764	2076	1913	-15	-8	+9
	125	0.205	1087	1242	956	-12	+14	+30
B	30	0	697		850		-18	
	30	0.115	405		425		-5	

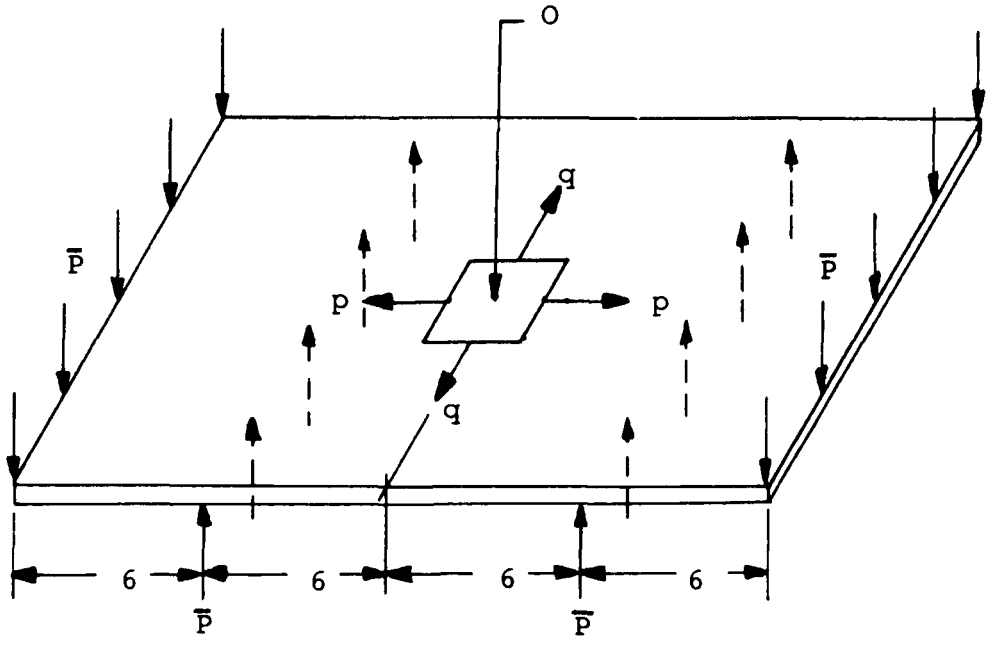

TABLE 6

COMPARISON OF 'p' AND 'q' STRESS RESULTS DETERMINED BY SCATTERED-LIGHT PHOTOELASICITY AND SIMPLE BEAM THEORY FOR FOUR-POINT BENDING SPECIMENS

Specimen	Load (lbs)	Stress (psi)	Experiment (psi)	Theory (psi)	Discrepancy (percent)
A	75	p	934	803	16
A	75	q	154	0	-
B	30	p	1064	850	25
B	30	q	554	0	-

$$\text{Discrepancy} = \frac{(\text{Experiment-Theory})}{\text{Theory}} \times 100$$

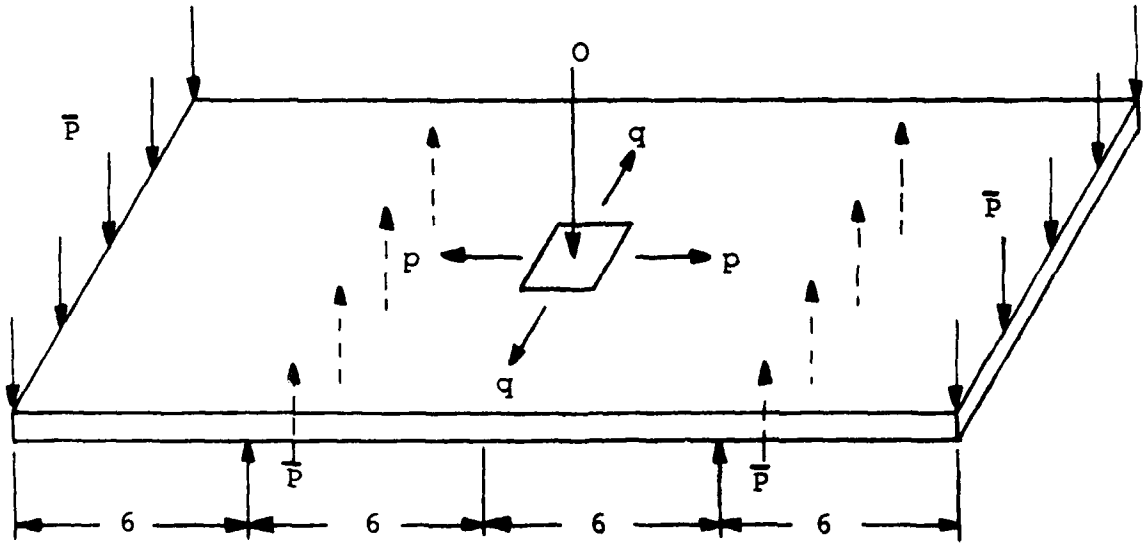

Specimen B subjected to 30 pounds load, additional fringes were obtained by introducing various levels of retardation with a compensator. This enabled one to obtain better defined birefringence curves from which the slope dN/dZ was determined. From these figures, it is inferred that the fringes moved down because of retardation introduced by a compensator whose axis was parallel to the maximum secondary principal stress axis, and moved up when the compensator axis was parallel to the minimum secondary stress axis. For higher loads, the fringe density increased (Figures 20(a) and (b)).

3.7.2 Curves of Birefringence

A second order polynomial curve fit was sufficient in all of the cases considered for Specimens A and B. The slope dN/dZ was obtained by computing dN/dZ from the polynomial equation

$$N(Z) = A_0 + A_1 Z + A_2 Z^2$$

and evaluating dN/dZ for various values of Z.

3.7.3 Secondary Principal Stresses

The maximum secondary principal stress p obtained by the first method (assuming the minimum secondary stress q to be zero) compared with simple beam theory within 20 percent (Table 5). The maximum discrepancy between experimental results and simple beam theory for the maximum secondary principal stress p determined by the second method was 25 percent.

The maximum discrepancy between the scattered-light method and the strain gage results was 15 percent except for the case of a 50 pound load at Z = 0.205. At quarter depth points the beam theory predicts lower stresses. At these points inside the beam, the agreement between scattered-light and the strain

gage results is generally good. Both the strain gage results and the scattered-light photoelastic results indicate a stretching of the middle surface of the beam, resulting in nonlinear variation of stress in the thickness direction of the beam.

3.8 TESTS ON ACRYLIC PLEX II FOUR-POINT BENDING SPECIMEN

Scattered-light fringes could not be detected in the acrylic Plex II specimen (0.75-inch thick) when it was subjected to 125 lb. load in the four-point bending test fixture. Therefore, the scattered-light photoelastic experiments on this acrylic plastic material could not be continued.

SECTION 4

DETERMINATION OF RESIDUAL STRESSES IN MONOLITHIC F-16 CANOPY USING SCATTERED-LIGHT PHOTOELASTICITY

The scattered-light photoelastic technique, developed and evaluated using the four-point bending specimens, was used to quantify the residual stresses in a monolithic polycarbonate F-16 canopy. A brief description of the specimen, the experimental procedure, and the results are presented and discussed in the following paragraphs.

4.1 TEST SPECIMEN

The specimen consisted of a monolithic polycarbonate F-16 transparency (Figure 27) which was identified as Air Force P/N FST 145/0103, manufactured 4/11/80 by Texstar Plastics, Inc. The specimen was placed on a table, with its edges unrestrained.

4.2 EXPERIMENTAL PROCEDURE

The experimental procedure used to determine the basic data, namely the direction of the secondary principal stresses θ, and the difference of secondary principal stresses p-q, was the same as that used for four-point bending specimens. However, because of the high surface curvatures of the F-16 canopy, it became necessary to use an index matching fluid in contact with the canopy surface to overcome the effects of refraction.

4.2.1 Refractive Index Matching Fluid Tank

The refractive index of polycarbonate is 1.589, and there are many mineral oils whose refractive indices match the refractive index of polycarbonate. Refractive index matching fluid type IMF-1618-A, supplied by the Photoelastic Division of Measurements Group Inc., was used in this investigation. The refractive index of this fluid was matched by conducting a simple

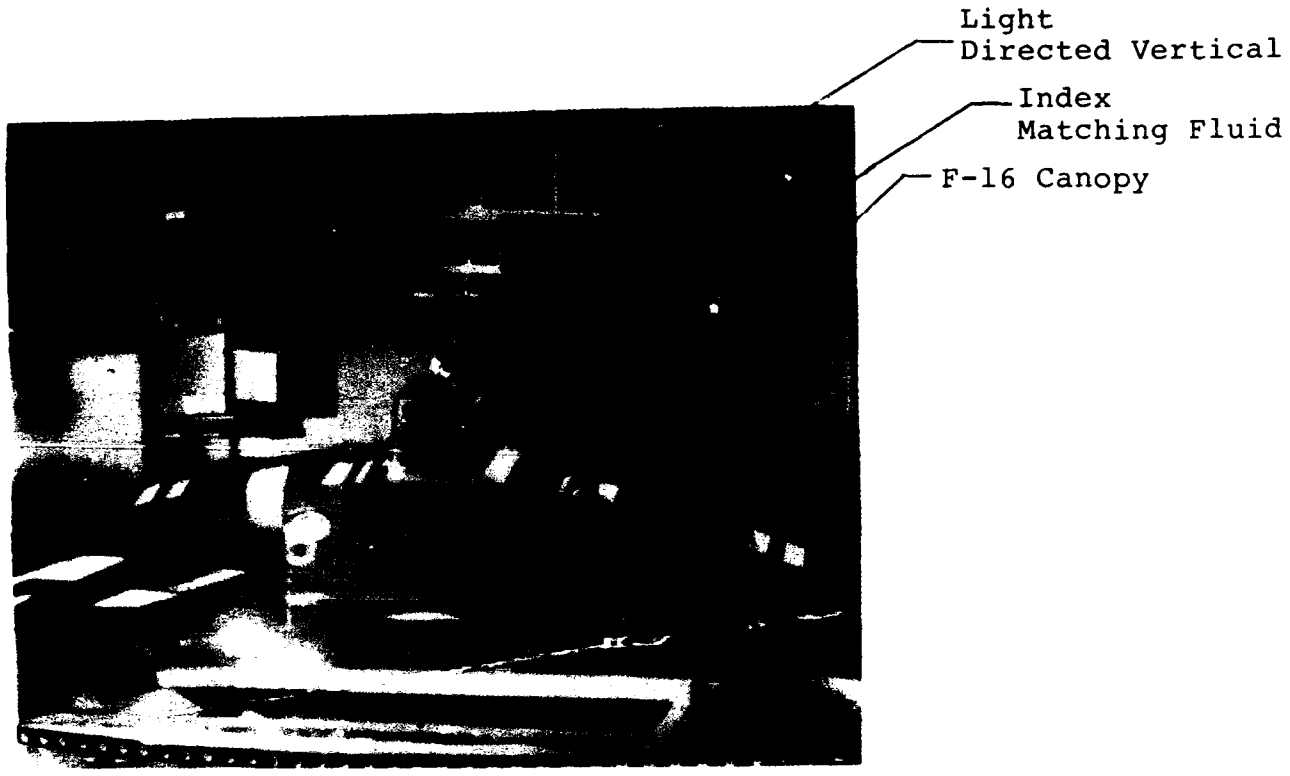

Figure 27. Monolithic Polycarbonate F-16 Canopy Placed Under Scattered-Light Device, Light Directed Vertically.

experiment using a model consisting of a wedge-shaped specimen made of polycarbonate and immersed in a glass tank filled with the fluid (Figure 28). The refractive index was matched when the wedge-shaped specimen no longer deflected the beam of light, as would happen in the unmatched condition. The refractive index of IMF-1618-A was found to match the refractive index of polycarbonate without the addition of mineral oil.

Since the polycarbonate material is chemically attacked by the matching fluid, it became necessary to enclose the fluid in a small tank. The coordinates of Station 0 on the F-16 canopy selected for the purpose of determining residual stresses were X = 5.07, Y = -43.72, and Z = 20.86 measured from origin O_1 (Figure 29). A small tank of dimensions 6"x8"x5" was fabricated with its lower surface matching the curvature of the F-16 canopy at this station and its top left open. Acrylic sheet of 0.03 in. thickness was selected for the lower surface of the tank. This material is not damaged in the presence of IMF-1618-A fluid, and will conform to the curvature of the canopy. The viewing side of the tank was made of 0.75 inch acrylic sheet. The other three sides of the tank were made of anodized (black) aluminum sheets of 0.5-inch thickness. Cyanoacrylate adhesive was used to bond the 0.03 inch acrylic sheet to the lower edges of the tank. Silicon Form-A RTV caulking was used on the four corner edges of the tank to prevent leakage.

The light was directed vertically (Figure 29) and the direction of the secondary principal stresses was determined using a procedure similar to that used for the four-point bending specimen experiments. The directions of secondary principal stresses were along OX and OY (Figure 29). The F-16 canopy was then rotated until maximum light intensity fringe patterns were observed. Maximum contrast of the photoelastic fringes was seen when viewed at an angle making 45 degrees with one of the

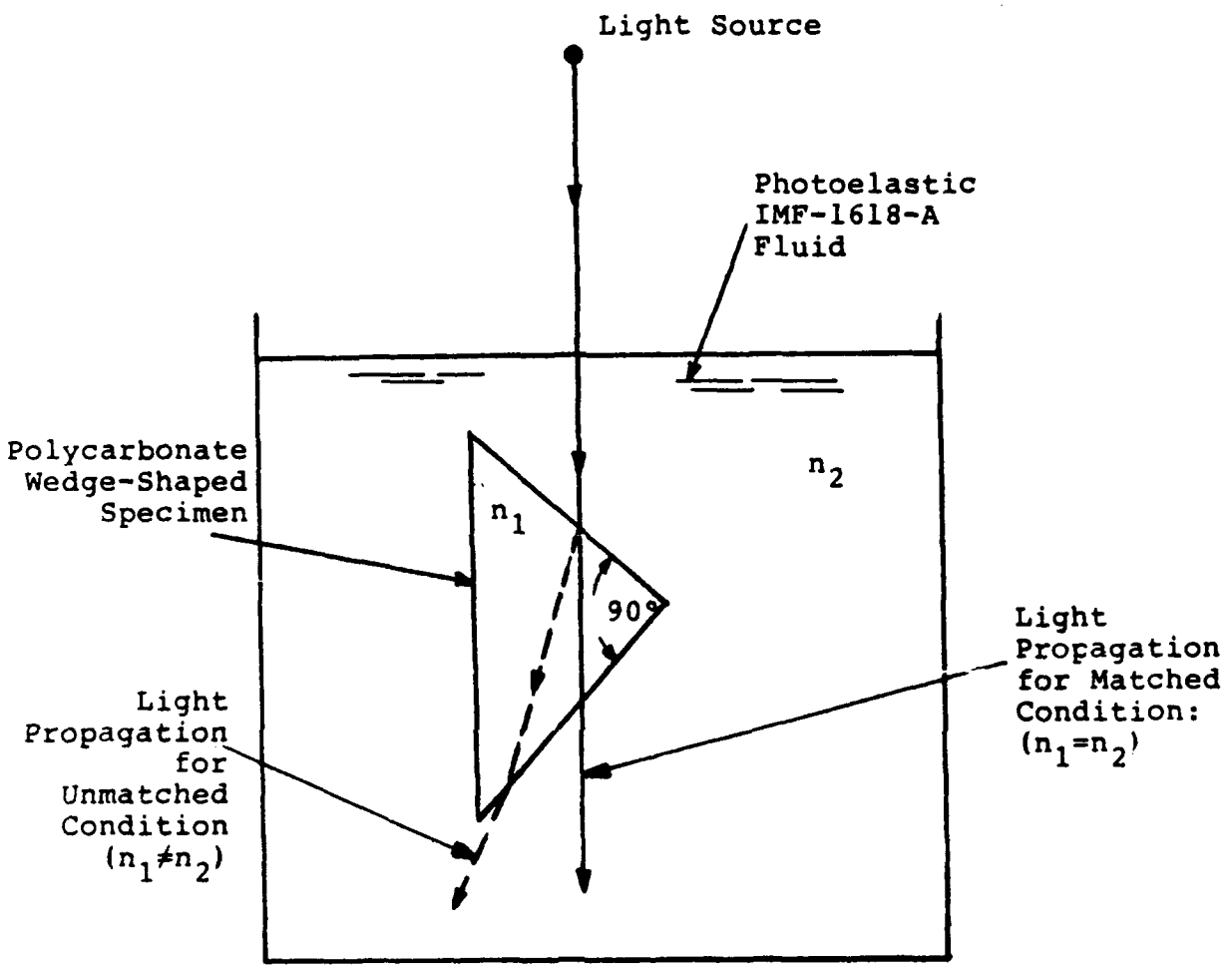

Figure 28. Matching of Refractive Indices of Polycarbonate Material and Index Matching Fluid, Photoelastic Type IMF-1618-A.

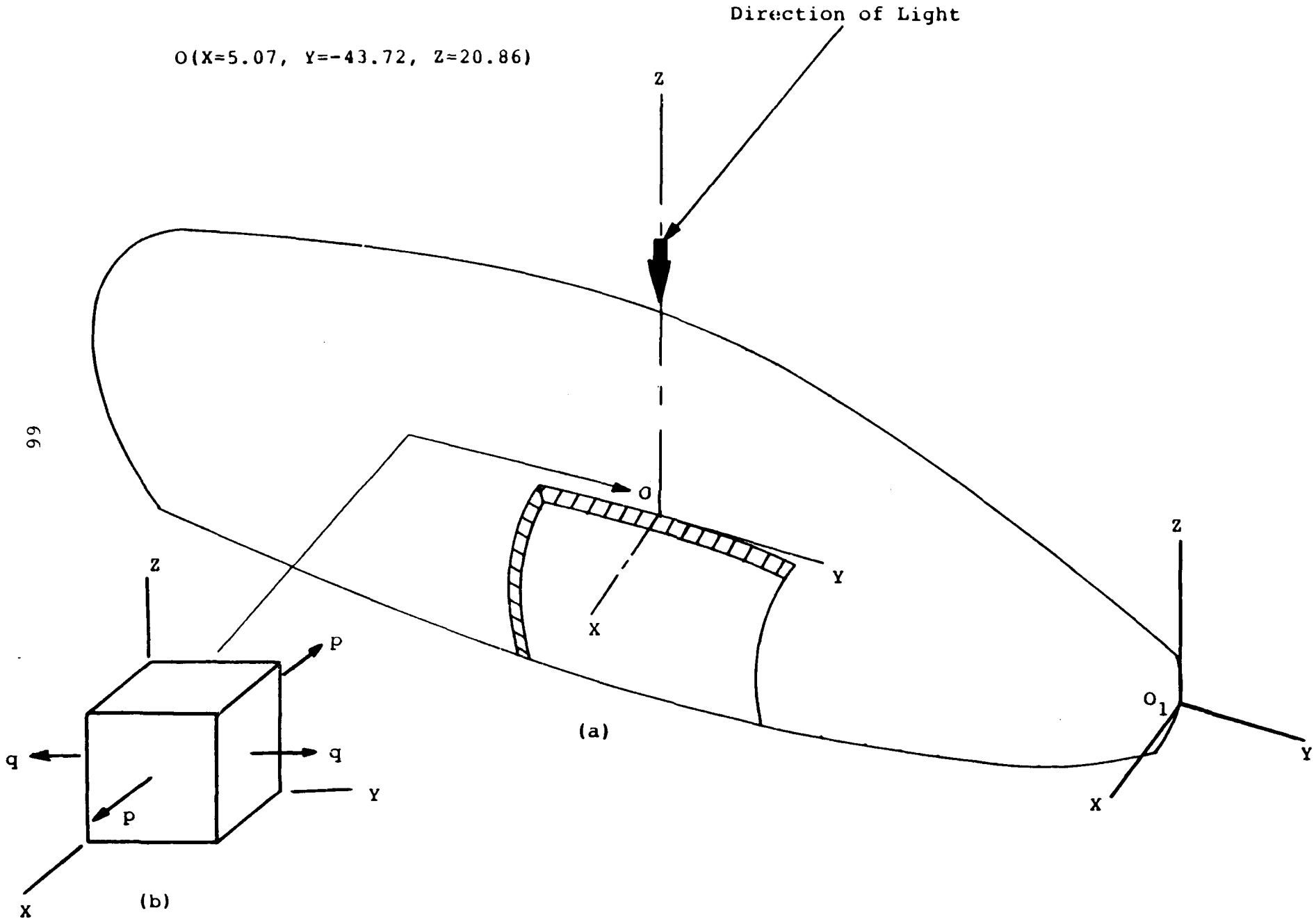

Figure 29. Secondary Principal Stresses at Point "O" in Monolithic Polycarbonate F-16 Canopy.

directions of the secondary principal stresses. The fringes had a very high density. These fringes were photographed by the Nikon 2020 camera equipped with close-up lens No. 2 and eyepiece magnifier (2X) from a distance of 13 inches from the sheet of light entering the F-16 canopy at Station O. Kodak Plus-X pan roll film with ASA 125 was used to photograph the fringes.

Film magnification was determined directly from the fringe photographs and the known vertical thickness of the canopy (0.672 inch) at Station O, by a method similar to that used for four-point bending specimens.

4.3 EXPERIMENTAL RESULTS

A discussion of the scattered-light photoelastic fringes, the curves of birefringence, and the secondary principal stresses for the F-16 canopy are presented in the following paragraphs.

4.3.1 Scattered-Light Photoelastic Fringes

Figure 30 presents the scattered-light photoelastic fringes at point O for the F-16 canopy when the light was directed vertically. Figure 31 presents the scattered-light photoelastic fringes when a retardation N = 3/4 was introduced by a compensator whose axis was perpendicular to the symmetry axis of the F-16 canopy.

4.3.2 Curves of Birefringence

Figure 32 shows the second order curve of birefringence for the F-16 canopy and the experimental points. The coefficients of the polynomial are also shown in the same figure.

4.3.3 Secondary Principal Stresses

The direction of the maximum secondary principal stress p was determined from Figure 31. The fringe close to the

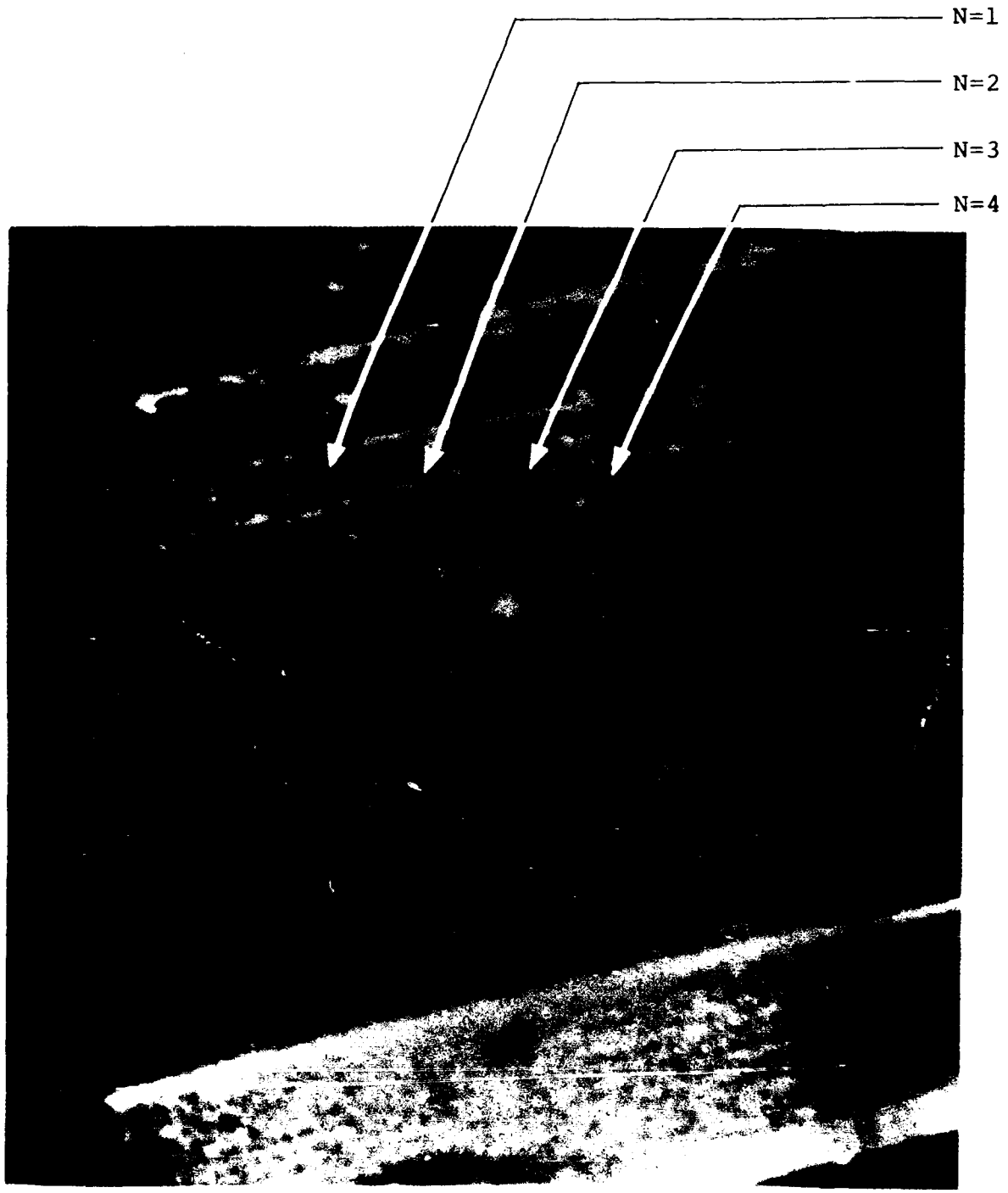

Figure 30. Scattered-Light Fringes from a Sheet of Light Passing Through Monolithic Polycarbonate F-16 Canopy, Light Directed Vertical.

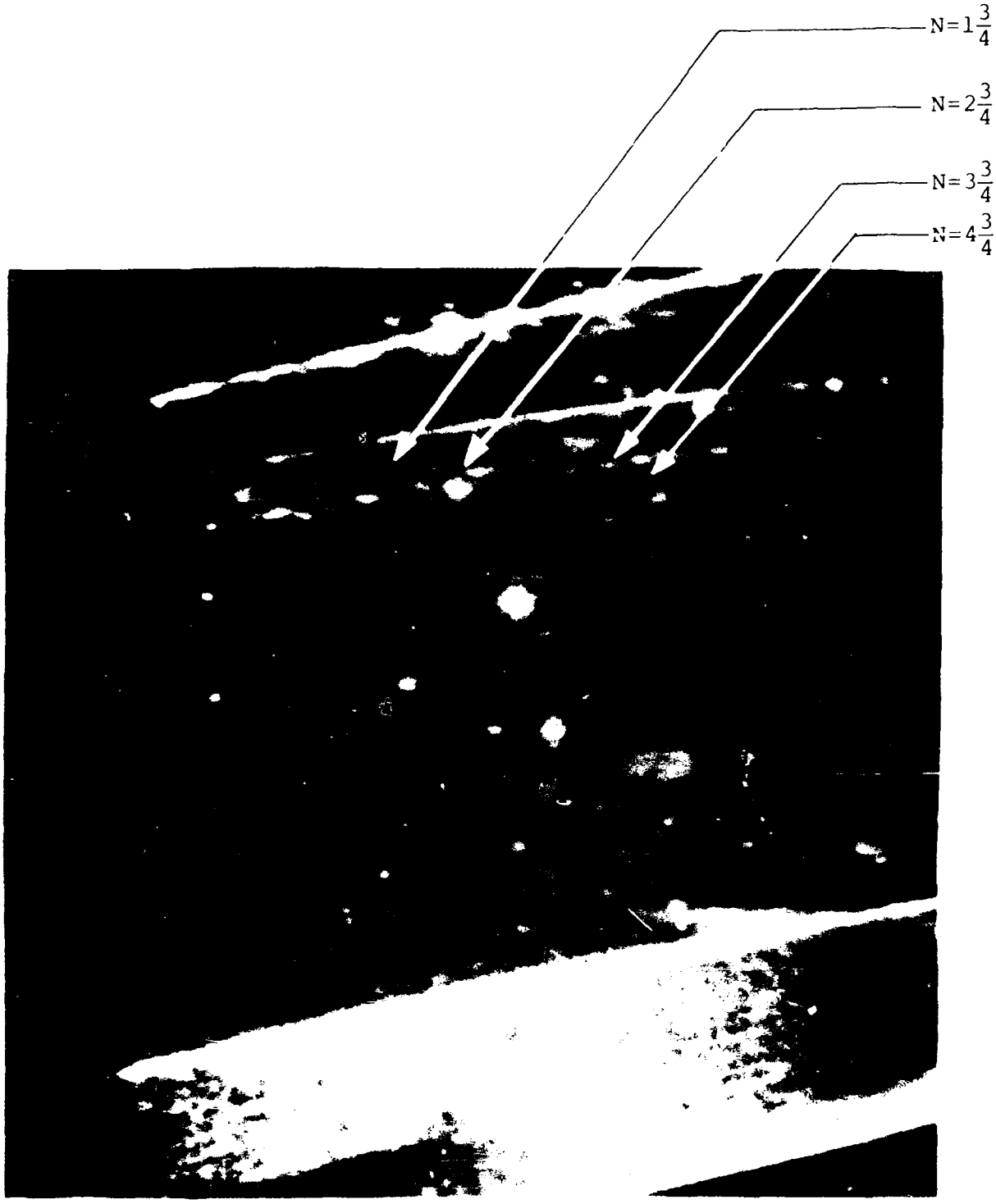

Figure 41. Scattered-Light Photoelastic Fringes from a Sheet of Light Passing through Monolithic Polycarbonate F-16 Canopy, Light Directed Vertical, Compensator Axis Perpendicular to Symmetry Axis, Retardation: $N=\frac{3}{4}$

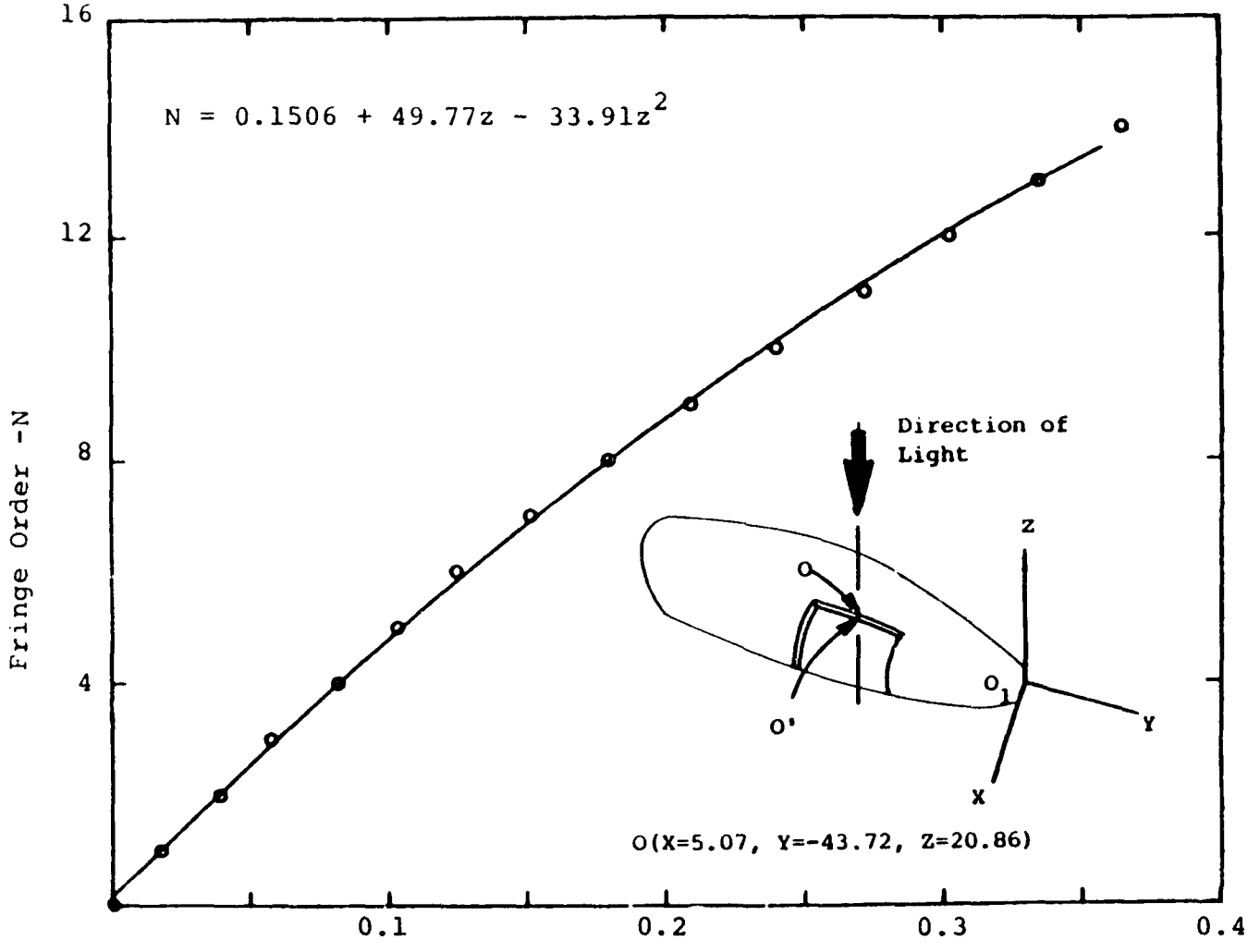

Figure 32. Second-Order Curve of Birefringence along line "OO'" in Monolithic Polycarbonate F-16 Canopy, Light Directed Vertically.

boundary moved down when a retardation of N = 3/4 was introduced by a compensator whose axis was perpendicular to the symmetry axis. Therefore, the direction of maximum secondary principal stress p coincided with the X axis (Figure 33).

The secondary principal stresses were computed from the fringe data by assuming that the secondary stress q in the direction of symmetry axis of the F-16 canopy was zero (see Figure 29). The residual stresses in the vertical direction at a point O in the F-16 canopy are shown in Figure 33.

4.4 DISCUSSION OF RESULTS

4.4.1 Scattered-Light Photoelastic Fringe Photographs

The striking feature of the scattered-light photoelastic fringes obtained from the F-16 canopy was the high fringe density. There were about 24 fringes in a thickness of 0.672 inches measured vertically at point O on the F-16 canopy. This gave a fringe density of 36 fringes per inch, or a fringe spacing of 0.028 inch.

4.4.2 Curves of Birefringence

Just as in the case of four-point bending beam, a second order polynomial was used to curve-fit the experimental points.

4.4.3 Secondary Principal Stresses

The assumption was made that one of the secondary principal stresses, q, was negligible. If most of the residual stress induced in the transparency was due to forming, and q=0, then the maximum secondary principal residual stress p in a plane perpendicular to the direction of light was tensile and in the direction perpendicular to the symmetry axis of the F-16 canopy. If this is not the case, then the stress reported is the difference in the principal stresses, p-q.

z (inches)	p (psi)	q (assumed) (psi)
0.0	2041	0
-0.10	1763	0
-0.20	1485	0
-0.30	1206	0

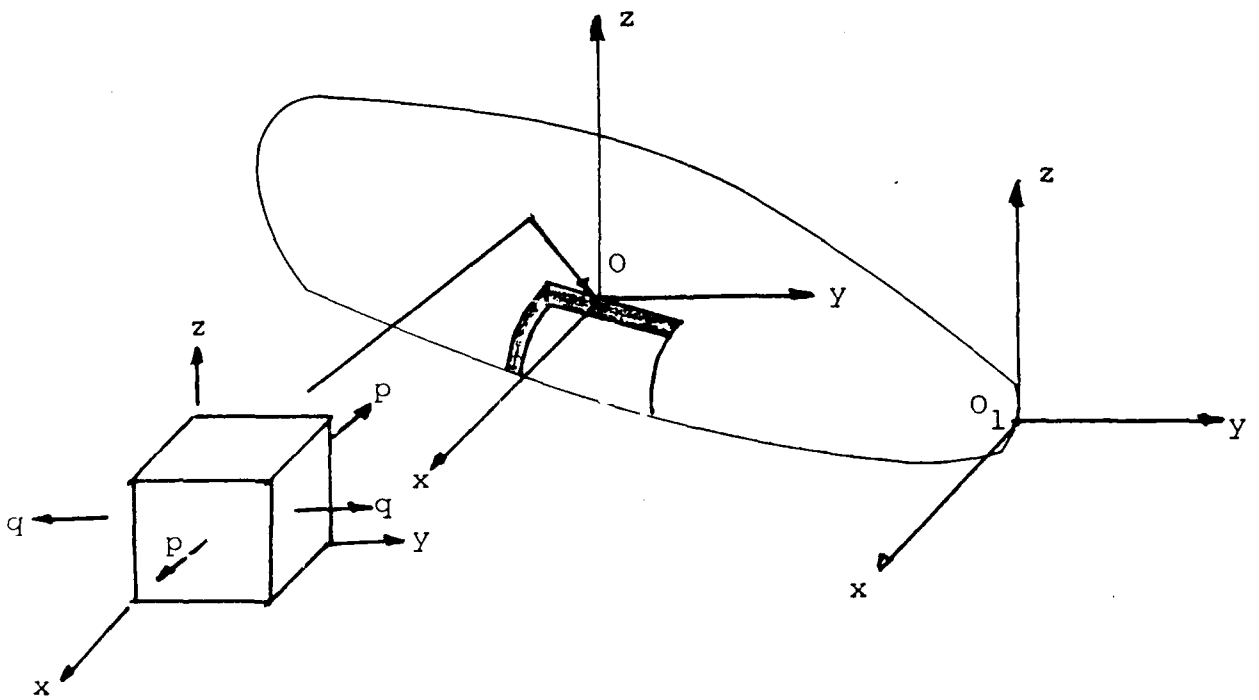

Figure 33. Residual Stresses Along a Vertical Line at O in F-16 Canopy.

SECTION 5
SURFACE WAVE ULTRASONIC TECHNIQUE

The experimental technique which was investigated us based on the measurement of changes in the velocity of acoustic surface (Rayleigh) waves due to internal stresses in acrylic plastic material (References 25 and 26). In order to apply the technique to aircraft transparencies, a surface wave transducer which had a sensitivity to measure stresses of the order of 500-2000 psi in acrylic plastics was required. The following paragraphs describe the efforts made in the development of a surface wave transducer and its experimental evaluation.

5.1 SURFACE WAVE TRANSDUCER

The design and fabrication of the transducer is based upon the transducer information given in Reference 25. The transducer consists of a piezo-electric crystal which contacts the sample surface via a thin element, producing a line contact (Figures 34 and 35). The element thickness must be less than half a wavelength. The couplant used between the transducer and the acrylic plastic was honey. When the crystal is driven by a short electrical pulse it generates a displacement, normal to the surface of the polymer, of those regions in contact with the transducer elements. Most of the energy of the excitation is converted to bulk wave propagation in the polymer, but a small amount is coupled into a surface wave traveling normal to the plane of the transducer elements. The pulse is detected by a similar transducer contacting the surface in the path of the wave at a predetermined distance from the first transducer element (Figure 34).

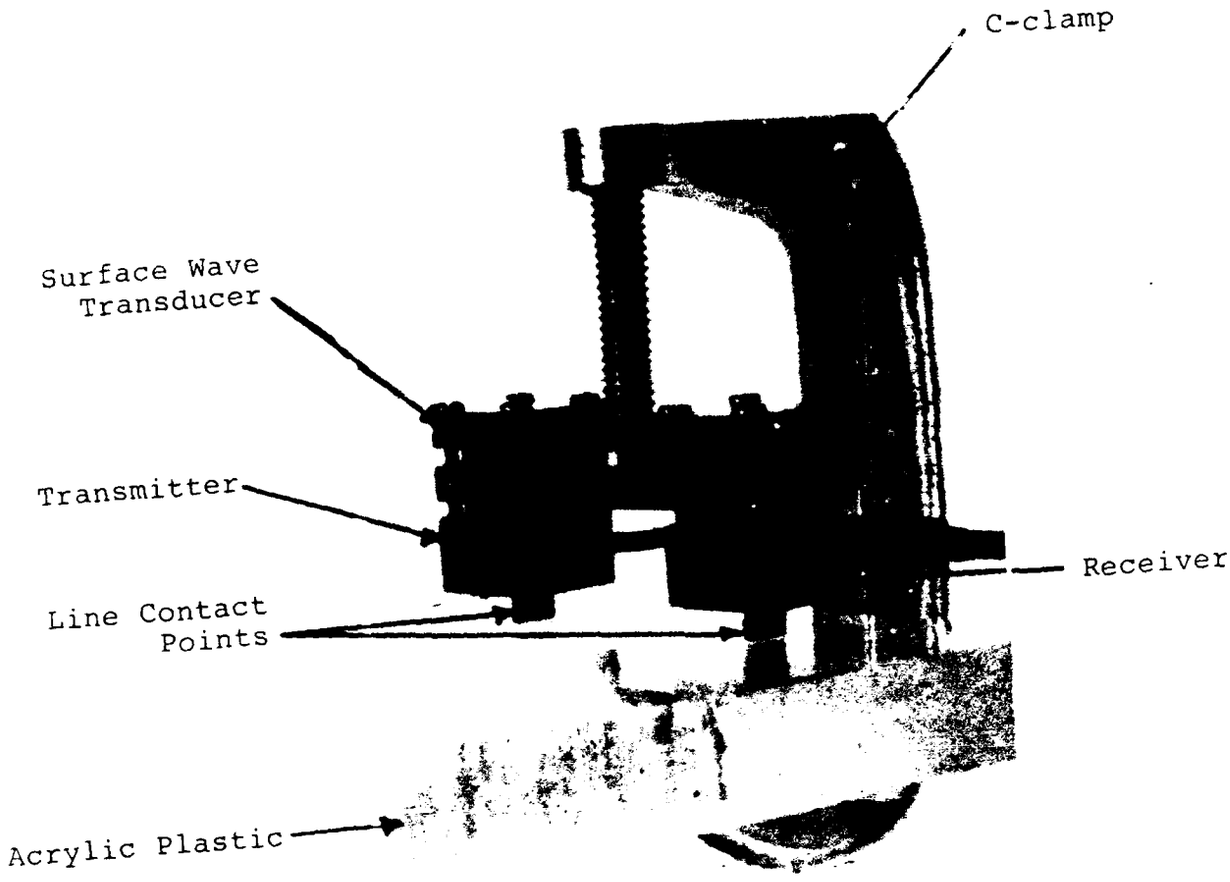

Figure 34. Surface Wave Transducer.

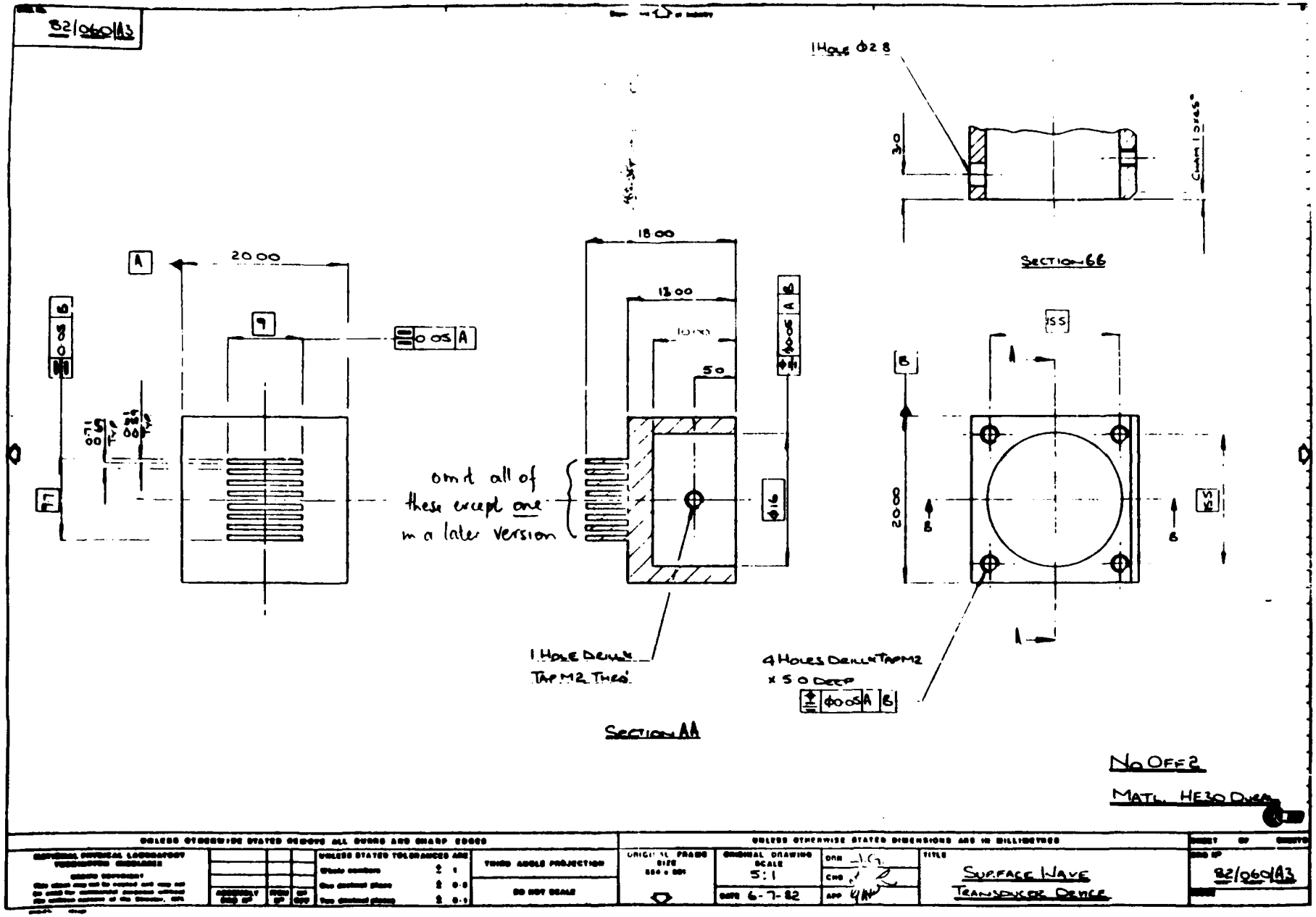

Figure 35. Aluminum Housing of Surface Wave Transducer (Supplied by NPL, U.K.).

5.2 EVALUATION OF SURFACE WAVE TRANSDUCER

The surface wave transducer was manufactured by Harisonic Laboratories, Inc. as per the details provided in Reference 25. A performance documentation report was supplied by the manufacturer (Figures 36 and 37) along with the details of the instrumentation used in the performance evaluation. From these figures it is seen that peak energy was at a frequency of 1 MHz, but the surface wave consisted of a mixture of waves of several frequencies and the wave amplitude itself was small. A pure 1 MHz monofrequency surface wave was not observed. Figure 37 shows the first cycle seen at a 5 KHz repetitive rate.

The performance evaluation was independently checked at the NDE Branch, Materials Laboratory, AFWAL, and in the Electrical and Computer Engineering Division of UDRI. The schematic of instrumentation used in the NDE Branch for evaluating this transducer is shown in Figure 38. The surface waves and the Fourier transform of the surface waves in acrylic plate material generated by this transducer are shown in Figures 39 and 40. The Fourier transform of the surface wave in the frequency domain which was obtained by the Electrical and Computer Engineering Group, using a spectrum analyzer, is shown in Figure 41. From these figures it is also seen that the surface wave launched by the transducer in acrylic plastic material consisted of a mixture of several wave components at different frequencies.

Using the transducer shown in Figure 35, a monofrequency surface wave could not be launched in polycarbonate material, and hence it cannot be used for the determination of residual stresses in aircraft transparencies. This is consistent with the results reported in Reference 25.

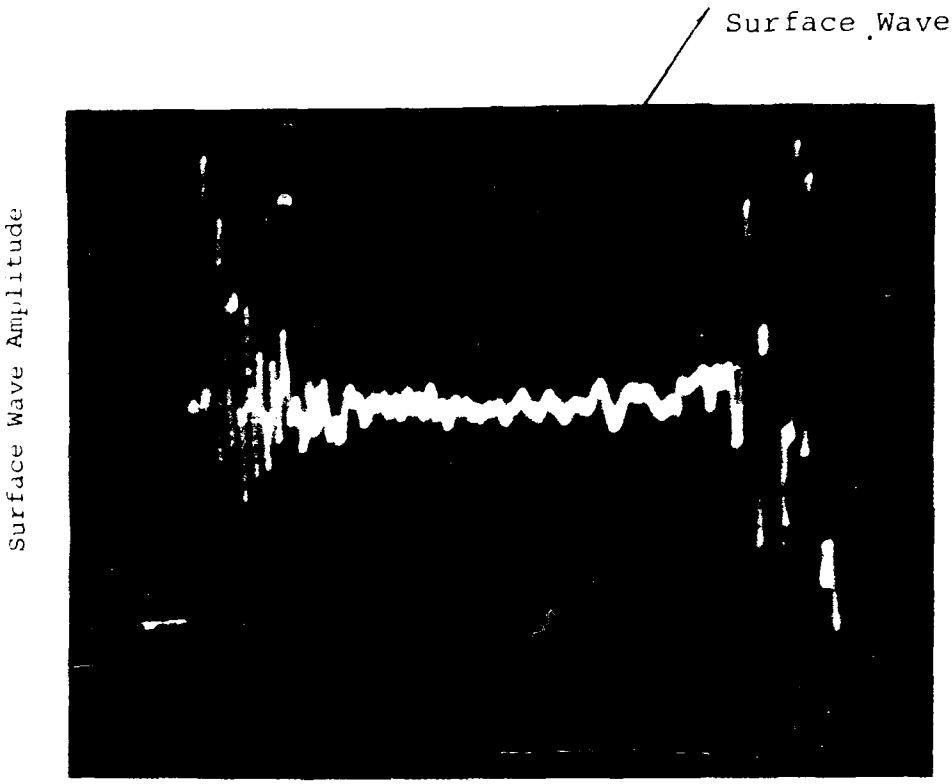

(a) Surface Wave in Time Domain

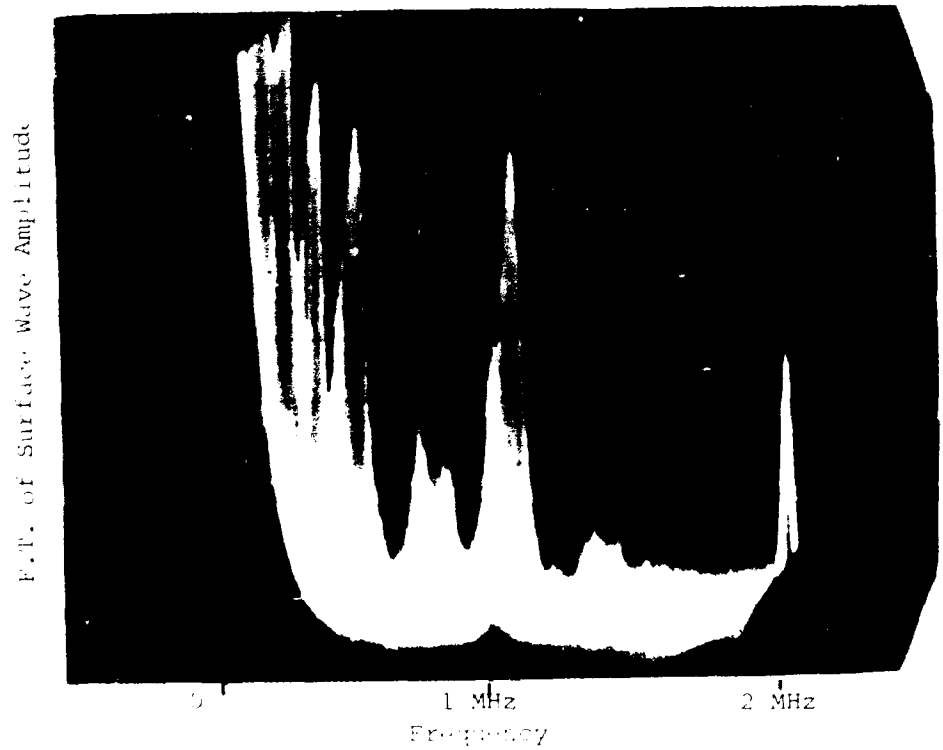

(b) Surface Wave in Frequency Domain

Figure 36. Surface waves in Acrylic Plastic Materials (Obtained by Harisonic Laboratories Inc.).

Surface Wave

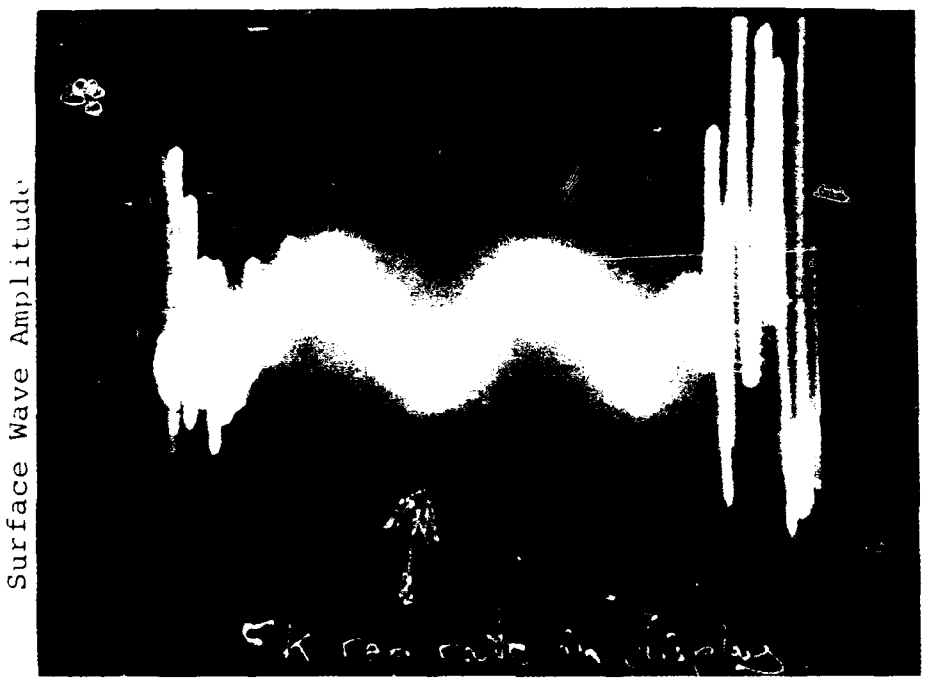

Figure 37. Surface Waves in Acrylic Plastic Material (First Cycle) (Obtained by Harisonic Laboratories, Inc.).

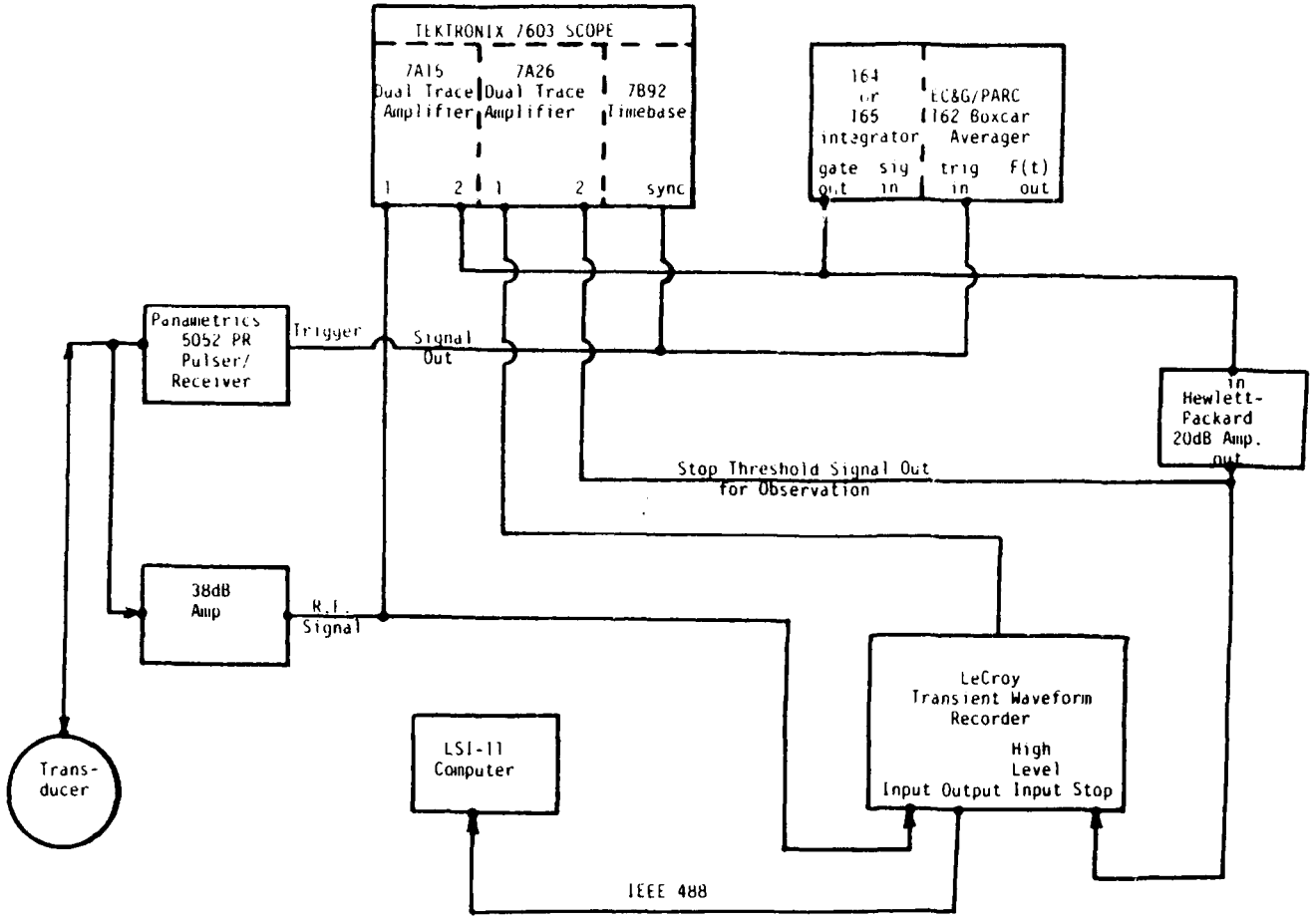

Figure 38. Experimental Setup for Transducer Evaluation (NDE Branch, Materials Division, AFWAL).

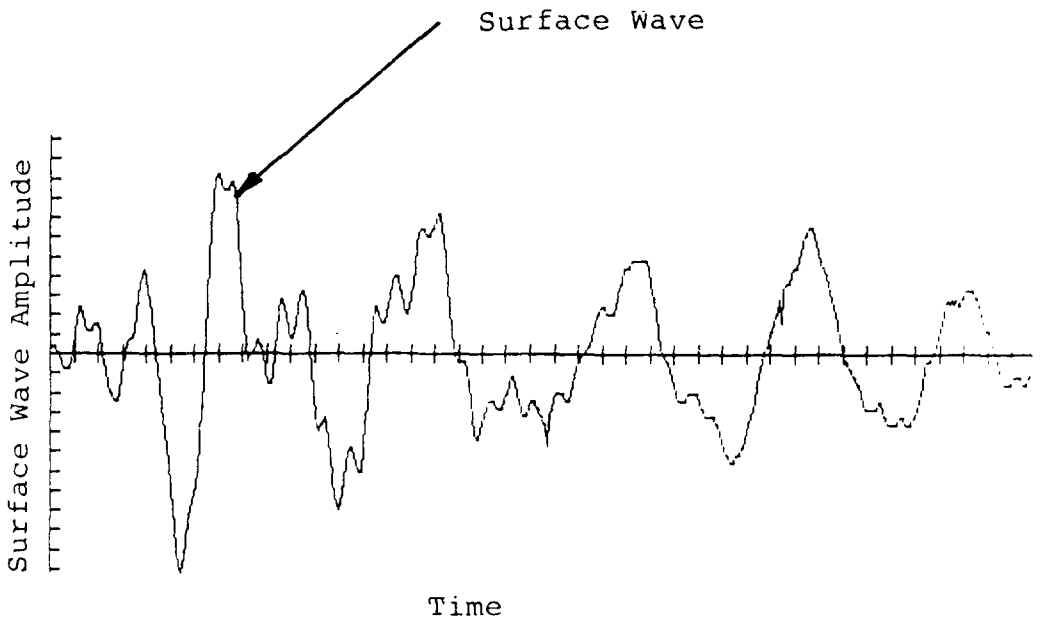

Vertical: 1 DIV = 5 mV

Horizontal: 1 DIV = 1 μseconds

Figure 39. Surface Waves in Acrylic Plastic Materials (Obtained by NDE Branch, Materials Laboratory, AFWAL).

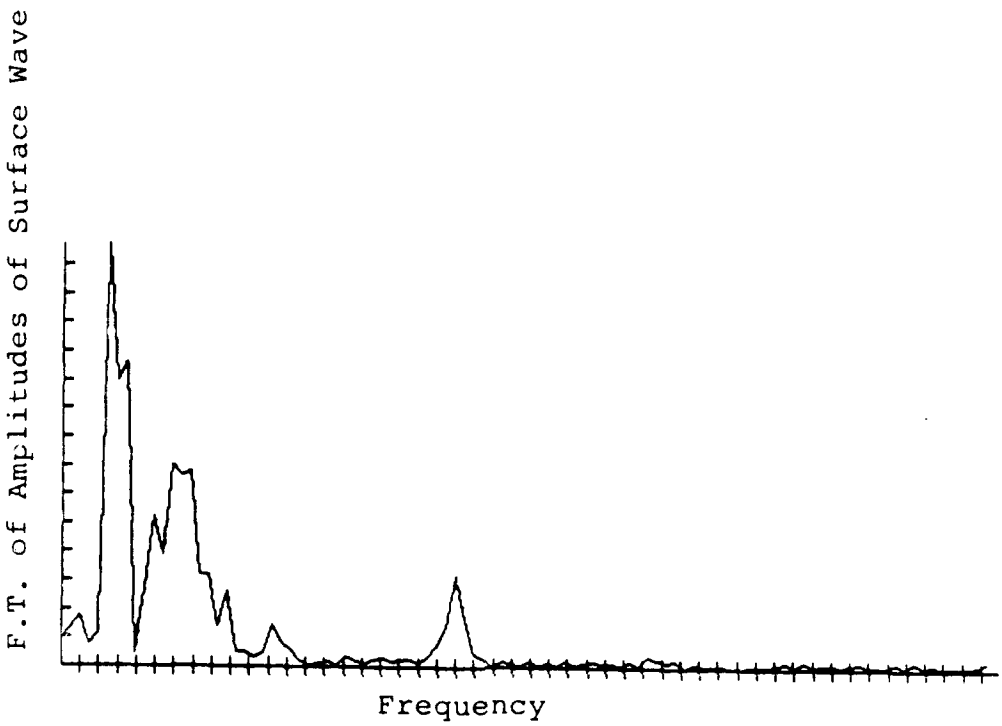

Scale: Vertical = 20 μV per division
Horizontal - 50 KHz per division

Figure 40. Fourier Transform of the Amplitudes of Surface Wave (Obtained by NDE Branch, Materials Laboratory, AFWAL).

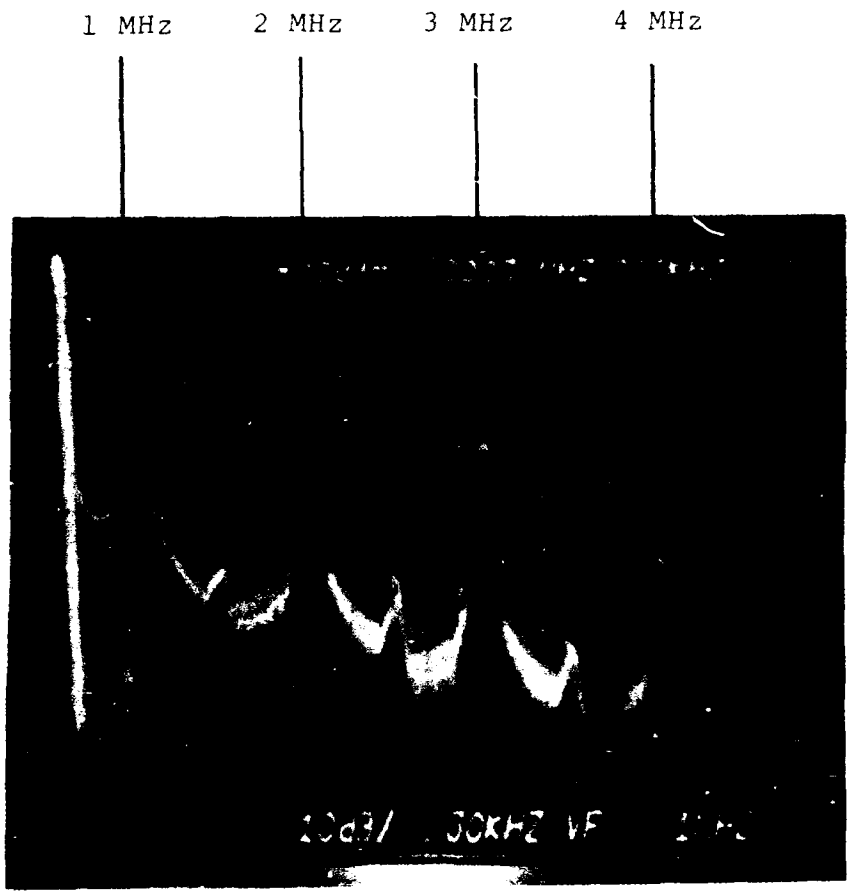

Scale: Vertical: 10 db/cm
Horizontal: as marked

Figure 41. Fourier Transform of Surface Wave Amplitude in the Frequency Domain (Obtained by Electrical and Computer Engineering Group, UDRI).

SECTION 6
CONCLUSIONS AND RECOMMENDATIONS

6.1 CONCLUSIONS

- The scattered-light photoelastic technique shows promise for nondestructively evaluating the surface stress level in monolithic and laminated transparencies having polycarbonate outer plies.

- The scattered-light photoelastic technique cannot be used with acrylic material due to the poor light scattering properties of the material.

- The surface wave ultrasonic technique could not be successfully applied to acrylic material. This application is limited by the state of the art in surface wave transducers.

- The surface wave ultrasonic technique is not feasible for use with polycarbonate material because the amplitude of the waves is too small to provide reliable measurements of wave velocity.

- The laboratory setup required for the scattered-light photoelastic technique does not provide encouragement for reduction to a portable "suitcase" type field technique. However, automation could make it feasible to set up a field station at an operational base and bring the aircraft to the evaluation station. The equipment could then be considered "portable" between operational bases.

6.2 RECOMMENDATIONS

- Further substantiate the repeatability, accuracy, and sensitivity of the scattered-light photoelastic technique for monolithic polycarbonate by determining the stress levels at several additional locations on the F-16 canopy. Determine

stresses at the same locations by an established experimental technique such as the blind-hole drilling technique and compare results.

- Improve the resolution and accuracy of high density scattered-light photoelastic fringes by replacing the Nikon 2020 camera with a Nikon F-3 camera equipped with a 6X high magnification eyepiece finder and a 200 macrolens. Also investigate the determination of fringe positions by use of a photoelectric tube and photometer.

- Verify the scattered-light photoelastic technique for use on laminated transparencies having polycarbonate outer plies.

- Further investigation of the surface wave ultrasonic technique is not recommended with current state-of the-art transducers.

REFERENCES

1. Raju, B. Basava, "A Review Study of Nondestructive Test Techniques for Residual Stresses in Aircraft Transparencies," AFWAL-TR-83-3108, Flight Dynamics Laboratory, Wright-Patterson Air Force Base, Ohio, January 1984.
2. Weller, R., "Three-Dimensional Photoelasticity Using Scattered-Light," Journal of Applied Physics, Vol. 12, August 1941, pp. 610-616.
3. Weller, R. and J. K. Bussey, "Photoelasic Analysis of Three-Dimensional Stress Systems Using Scattered Light," NACA Technical Note No. 737, November 1939.
4. Jessop, H. T., "The Scattered Light Method of Exploration of Stresses in Two- and Three-Dimensional Models," British Journal of Applied Physics, Vol. 2(9), September 1951, pp. 249-260.
5. Frocht, M. M. and L. S. Srinath, "A Non-destructive Method for Three-Dimensional Photoelasticity," Proceedings of the Third U.S. National Congress of Applied Mechanics, ASME, 1958, pp. 329-336.
6. Srinath, L. S. and M. M. Frocht, "Scattered-Light in Photoelasticity--Basic Equipment and Techniques," Proceedings of the Fourth U.S. National Congress of Applied Mechanics, ASME, 1962, pp. 775-781.
7. Srinath, L. S., "Analysis of Scattered-Light Methods in Photoelasticity," Experimental Mechanics, vol. 26, No. 2, October 1969, pp. 463-468.
8. Srinath, L. S. and A.V.S.S.R. Sarma, "Determination of the Optically Equivalent Model in Three-dimensional Photoelasticity," Experimental Mechanics, Vol. 31, No. 1, March 1974, pp. 118-122.

9. Cheng, Y. F., "Some New Techniques for Scattered-Light Photoelasticity," Experimental Mechanics, Vol. 20, No. 2, November 1963, pp. 275-278.
10. Cheng, Y. F., "A Dual Observation Method for Determining Photoelastic Parameters in Scattered-Light," Experimental Mechanics, Vol. 7, No. 3, March 1967, pp. 140-144.
11. Cheng, Y. F., "An Automatic System for Scattered-Light Photoelasticity," Experimental Mechanics, Vol. 26, No. 2, September 1969, pp. 407-412.
12. Cheng, Y. F., "A Scattered-light Photoelastic Method for the Determination of Tempered Stresses in Aircraft Windshields," Strain, Vol. 3, No. 2, 1967, pp. 17-22.
13. Swinson, W. F., J. L. Turner, and W. F. Ranson, "Designing with Scattered-Light Photoelasticity," Experimental Mechanics, Vol. 37, No. 2, November 1980, pp. 397-402.
14. Davis, J. B. and W. F. Swinson, "Experimental Investigation of Transient Thermal Stresses in a Solid Sphere," Experimental Mechanics, Vol. 8, No. 9, September 1968, pp. 404-428.
15. Braswell, D. W., W. F. Ranson, and W. F. Swinson, "Scattered-light Photoelastic Thermal Stress Analysis of a Solid Propellant Rocket Motor," Journal of Spacecraft, Vol. 5, No. 12, December 1968, pp. 1411-1416.
16. Aderholt, R. W., W. F. Ranson, and W. F. Swinson, "Scattered-light Photoelastic Stress Analysis of a Solid Propellant Rocket Motor," Experimental Mechanics, Vol. 27, No. 2, November 1970, pp. 481-485.
17. Fishburn, J. D., R. W. Aderholdt, W. F. Ranson, and W. F. Swinson, "Scattered-Light Rosette," Experimental Mechanics, Vol. 11, No. 12, December 1971, pp. 554-559.
18. McKinney, J. M. and W. F. Swinson, "Location of Maximum Secondary Principal Axis in Scattered-Light Photoelasticity," in Developments in Theoretical and Applied

Mechanics, 4, Pergamon Press Ltd., Oxford (1969), pp. 407-413.

19. _____, "Scattered Light Photoelasticity," Bulletin T-408, Photoelastic Division, Measurements Group, Inc., 1981.
20. _____, "Scattered-Light Polariscope," Bulletin S-119-A, Photoelastic Division, Measurements Group, Inc., 1981.
21. Dally, J. W. and W. F. Riley. Experimental Stress Analysis. McGraw-Hill Book Company (1978), pp. 457-459.
22. Raju, B. B., B. S. West, and A. J. Piekutowski, "Strains from Projection Moire Data," AFWAL-TR-83-3020, Flight Dynamics Laboratory, Wright-Patterson Air Force Base, OH, February 1983, pp. 1-56.
23 James, H. Lawrence Jr., "Guidelines for the Design of Aircraft Windshield/Canopy Systems," AFWAL-TR-80-3003, February 1980, pp. 6.020.
24. Perry, C.C., "Strain-Gage Reinforcement Effects on Low-Modulus Materials," Experimental Mechanics, May 1985, pp. 25-27.
25. Dean, G. D., "The Application of Acoustic Surface Waves to the Characterisation of Polymers," NPL Report DMA(A)112, December 1985.
26. Read, B. E., G. D. Dean, and J. C. Duncan, "Characterisation and Influence of Orientation and Internal Stress in Acrylic Aircraft Materials," NPL Report DMA(A)113, December 1985.
27. Heman, John H. and G. Y. Baaklini, "Effect of Stress on Ultrasonic Pulses in Fiber Reinforced Composites," Analytical Ultrasonics in Materials Research and Testing, pp. 181-191, January 1986.

APPENDIX

ELASTIC CONSTANTS OF POLYCARBONATE MATERIAL

Tension tests were conducted using the tension specimen shown in Figure A-1 to determine the value of Young's modulus, Poisson's ratio and also to evaluate the response of WA 13-060WT-120 2 element 90° 'Tee' stacked rosette and EP-08-125AD-120 strain gage when used on polycarbonate material. The gages were installed as shown in Figure A-1 and Figure A-2. The stress-strain curves obtained using these gages are shown in Figure A-3. The modulus obtained using these gages is shown in Table A-1.

The modulus was also obtained from dial gage deflections measured at the center of the four-point bending beam specimen from the equation:

$$E = \frac{Pa}{24 y_c I} (3\ell^2 - 12\, a\ell + 12a^2)$$

where y_c = center deflection, inches

I = moment of inertia of the beam, $inch^4$

P = load, lbs.

ℓ = total span of beam, inches

a = distance between end loads and the central supports, inches

The value of E computed from this formula is shown in Table A-2. The published Young's modulus value for polycarbonate is 0.35×10^6 psi (Reference 23). Thus, the Young's modulus determined by the WA-13-060WT-120 rosettes is higher than the published value. Young's modulus values evaluated from both the dial gage deflections at the center of the four-point bending beam and the EP-08-125AD-120 strain gages agreed with the

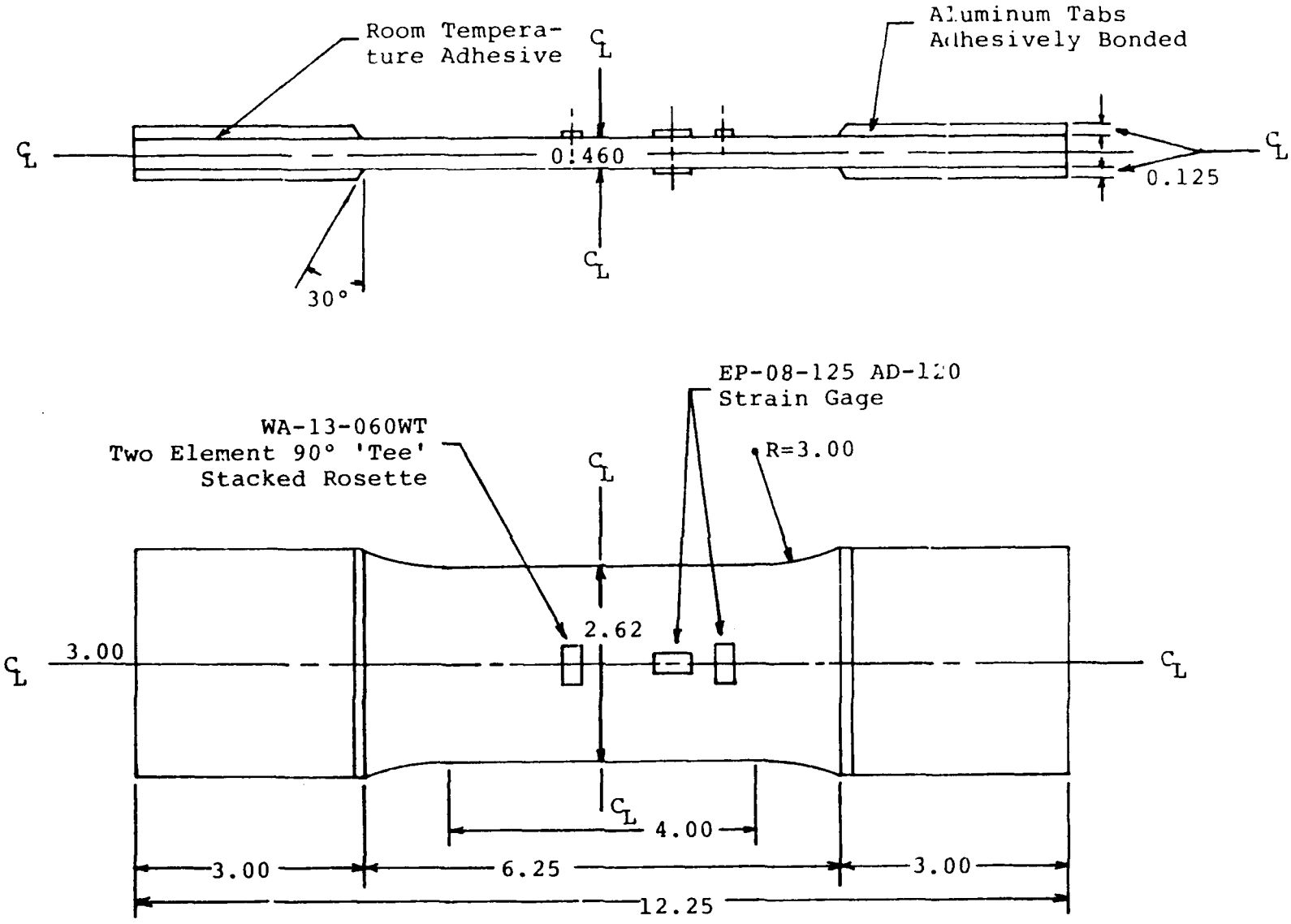

Figure A-1. Polycarbonate Tension Specimen.

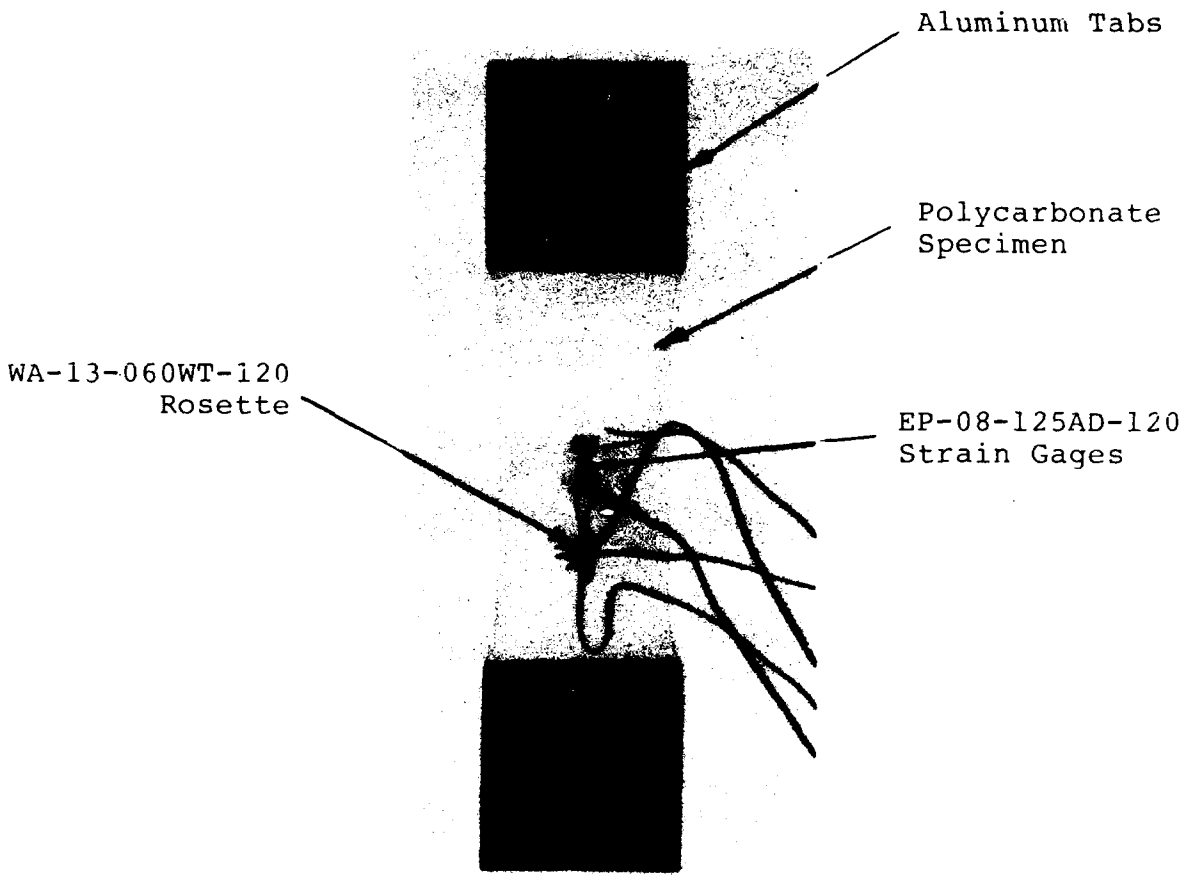

Figure A-2. Polycarbonate Tension Specimen.

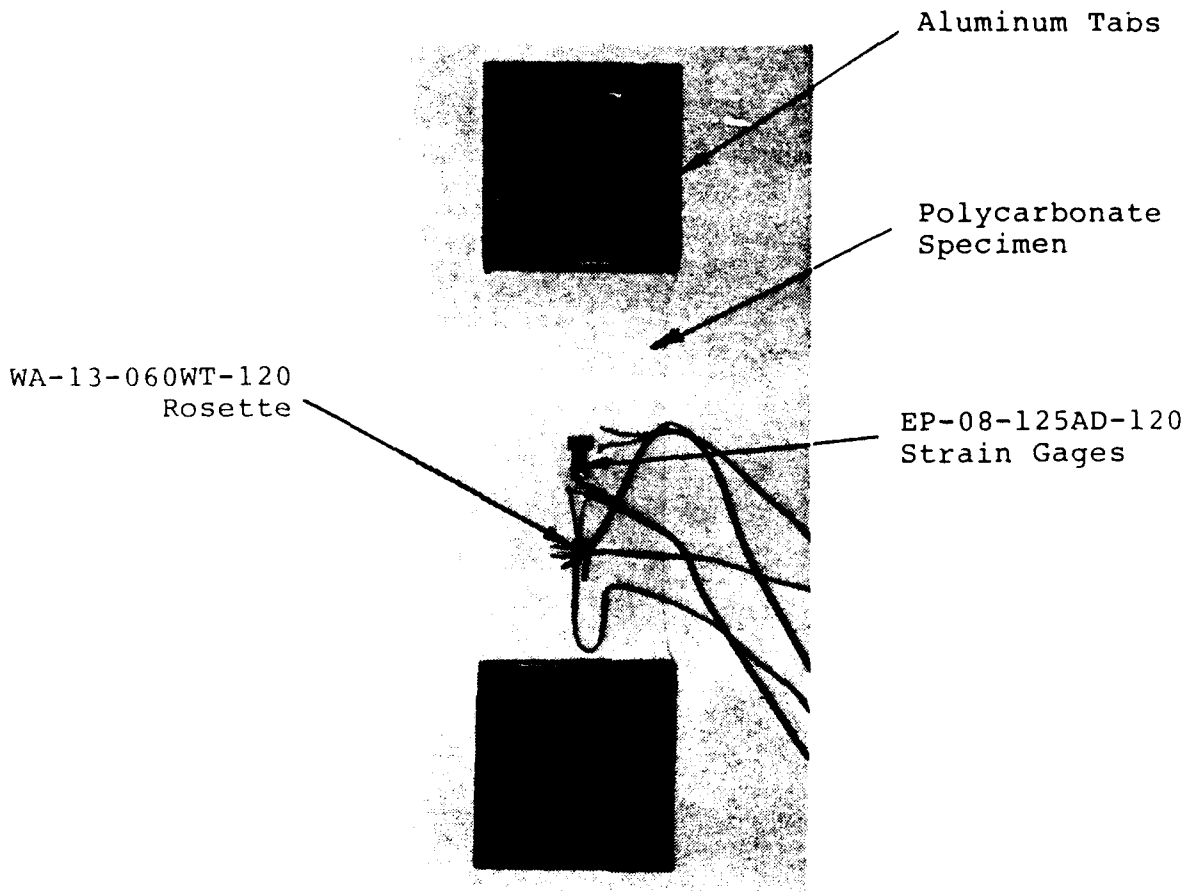

Figure A-2. Polycarbonate Tension Specimen.

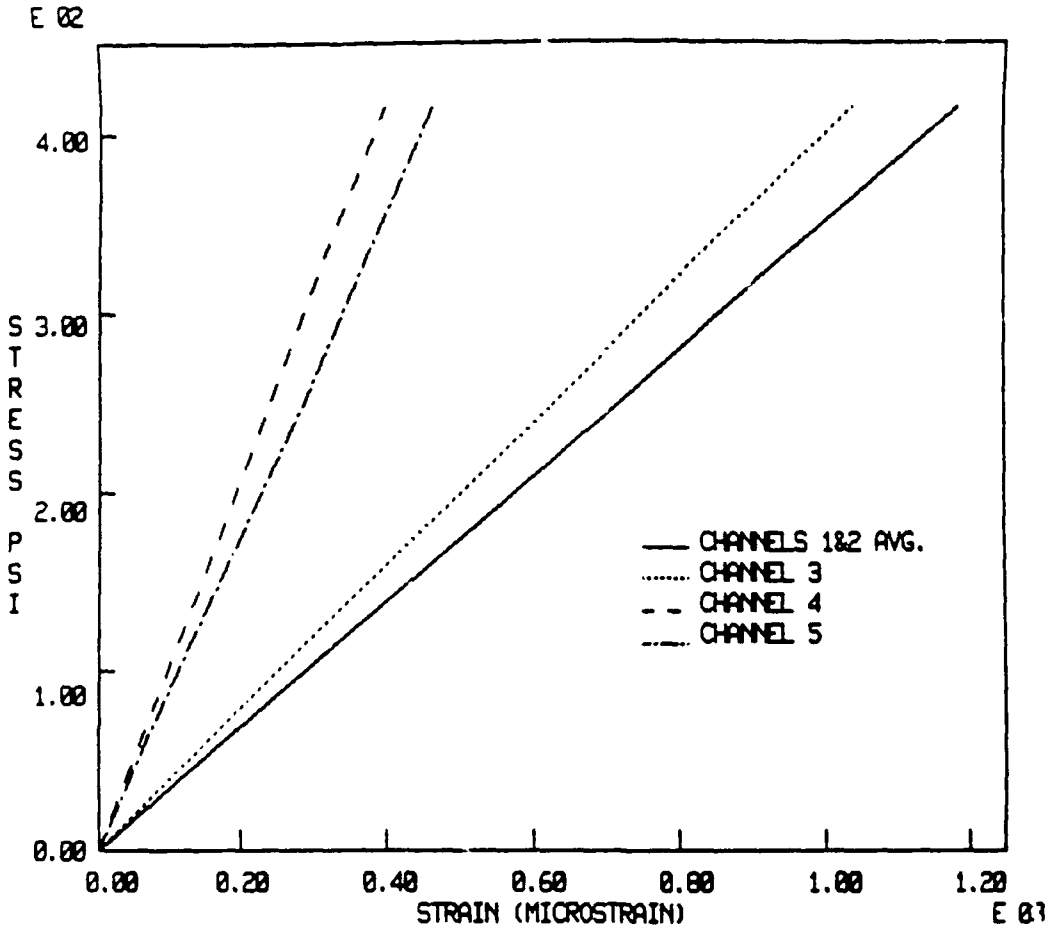

Channels 1, 2 & 5: EP-08-125 AD-120 Strain Gages
Channels 3 & 4: WA-13-060WT - 2 Element 90° 'Tee' Stacked Rosette

Figure A-3. Stress-Strain Curves from Tension Test on a Polycarbonate Specimen.

TABLE A-1

ELASTIC CONSTANTS FOR POLYCARBONATE MATERIALS
FROM STRAIN GAGE DATA

Channels 1&2 Avg.			Channels 1&2 vs 5 Pois.Ratio		
Stress (psi)	Strain (microstrain)	E (psi)	Strain 1&2 (ms)	Strain 5 (ms)	Ratio
83	242	343000	242	94	.388
166	477	348000	477	190	.399
249	712	350000	712	285	.401
333	945	352000	945	375	.400
415	1184	351000	1184	464	.392

Channel 3			Channel 3 vs 4 Pois. Ratio		
Stress (psi)	Strain (microstrain)	E (psi)	Strain 3 (ms)	Strain 4 (ms)	Ratio
83	210	395000	210	81	.386
166	415	400000	415	163	.393
249	624	399000	624	241	.386
333	828	402000	828	318	.384
415	1038	400000	1038	399	.384

Channels 1, 2 & 5: EP-08-125AD-120 Strain Gages
Channels 3 & 4: WA-13-060WT-2 Element 90°
'Tee' Stacked Rosette

TABLE A-2

YOUNG'S MODULUS FROM FOUR-POINT BENDING BEAM DEFLECTIONS

LOAD	DEFLECTION	E
(lbs.)	(in.)	psi x 10^6
50	0.093	0.361
75	0.143	0.3524
100	0.191	0.3518
125	0.214	0.3925

published value for the modulus. The Poisson's ratio determined by both gage types agreed well.

The WA13-060WT-120 two element rosette had a thick backing material which stiffened the polycarbonate material locally, resulting in lower values of measured strain and higher values for appropriate Young's modulus E. However, the correct value of stresses can be computed using the Young's modulus determined by the method defined in Reference 24. Stresses were computed by application of this correction to the strains measured in the four-point bending specimen using the WA-13-060WT-120 rosettes.

*U.S.Government Printing Office: 1989 - 748-056/24167